

9-3-2010

Novel techniques for the detection and localization of attenuated gamma-ray sources

Tyler Alecksen

Follow this and additional works at: https://digitalrepository.unm.edu/ne_etds

Recommended Citation

Alecksen, Tyler. "Novel techniques for the detection and localization of attenuated gamma-ray sources." (2010).
https://digitalrepository.unm.edu/ne_etds/25

This Thesis is brought to you for free and open access by the Engineering ETDs at UNM Digital Repository. It has been accepted for inclusion in Nuclear Engineering ETDs by an authorized administrator of UNM Digital Repository. For more information, please contact disc@unm.edu.

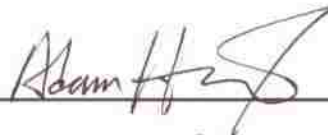
Tyler J. Alecksen
Candidate

Nuclear Engineering
Department

This thesis is approved, and it is acceptable in quality
and form for publication:

Approved by the Thesis Committee:

Dr. Adam Hecht



, Chairperson

Dr. Robert Busch



Dr. Gary Cooper



**Novel Techniques for the Detection and Localization of
Attenuated Gamma-Ray Sources**

by

Tyler J. Alecksen

**B.S., Electrical Engineering
New Mexico Institute of Mining and Technology**

THESIS

Submitted in Partial Fulfillment of the
Requirements for the Degree of

**Master of Science
Nuclear Engineering**

The University of New Mexico
Albuquerque, New Mexico

July, 2010

For my family

Acknowledgements

I would like to acknowledge my UNM advisor Dr. Adam Hecht whom with consistent guidance and encouragement has made these writings possible.

I also thank my research mentors and friends, Dr. Ken Baker, Charles Farr, Michael Schierman, and everyone at Environmental Restoration Group for the funding of this research and continuous support in my professional development. This would not have been possible without your aid and generosity.

To my family, I thank you, for without the love and support you have given me nothing would be possible. Thanks to my brother-in-law, James, for playing Call of Duty with me when I should have been writing. Those moments of distraction were well needed. And finally to my wife, Claire, I express immense gratitude for enduring all the good and bad that have come with these writings. Your endless support was never overlooked.

**Novel Techniques for the Detection and Localization of
Attenuated Gamma-Ray Sources**

by

Tyler J. Alecksen

ABSTRACT OF THESIS

Submitted in Partial Fulfillment of the
Requirements for the Degree of

**Master of Science
Nuclear Engineering**

The University of New Mexico
Albuquerque, New Mexico

July, 2010

NOVEL TECHNIQUES FOR THE DETECTION AND LOCALIZATION OF ATTENUATED GAMMA-RAY SOURCES

By

Tyler J. Aleksen

B.S., Electrical Engineering, New Mexico Institute of Mining and Technology, 2005

M.S., Nuclear Engineering, University of New Mexico, 2010

ABSTRACT

The use of cylindrical solid-crystal detectors for the detection and removal of gamma-emitting sources has become a common practice for the clean-up of radiological contaminated sites. It is often difficult to determine the capability of detecting a sub-surface source without performing experimental studies due to the large variation in detector types, source energy, and attenuating media. Furthermore, significant cost savings can be evident when the source is localized because time and the amount of material to be removed are reduced.

The first part of this thesis presents a method to determine the minimal detectable limits of a sub-surface source using multiple gridded measurements. The method uses data simulated with the Los Alamos Monte Carlo N-Particle transport code (MCNPX) for detector efficiency calculations. As a necessary supplement to the process, a program was written to automate all MCNPX simulations by modifying input cards and recording the results for all required scenarios. In this work, simulated experiments were performed using Cs-137 and Na-22 in air and soil media to demonstrate the method.

The second part of this thesis addresses the problem of source localization. By using a mapping of expected detector responses as a function of source location, the ratios of multiple detector measurements are fit to MCNPX simulated data. From the fit, the lateral position, depth, and activity of the source within an attenuating medium are

extracted. As with the first part of this thesis, the detectors are non-collimated to maintain high detection efficiency. The method is intended to be straightforward yet effective to allow real-time localization of sources. The method is a necessary conceptual step away from triangulation since real detectors have non-isotropic efficiency and real sources are commonly attenuated. Several experiments were performed using Cs-137 and Na-22 in both air and soil media to verify the method.

Contents

1	Introduction	1
1.1	Motivation of Work	2
1.2	Outline of Work	3
2	Literature Review	5
2.1	Source Localization Techniques	5
2.2	Determination of Detection Capabilities	7
3	Background.....	9
3.1	Gamma Radiation Detectors	9
3.2	The Monte Carlo Transport Method.....	9
4	Monte-Carlo Techniques and Validation.....	11
4.1	Detector Simulation	11
4.2	Detector Simulation Validation	13
4.3	MCNP Interface and Automation.....	19
5	Detection Certainty of Source.....	22
5.1	Simulated Efficiency Mapping	23
5.2	Resolution of Signal from Background.....	26
5.3	Effects of Detector Starting Location.....	30
5.4	Results	34

6	Localization of Source	37
6.1	Simulated Efficiency Mapping	38
6.2	Fitting Measured Data to Simulated Data	42
6.3	Certainty from Counting Statistics	46
6.4	Simulation Results	52
6.4.1	Simulation Experiment 1	53
6.4.2	Simulation Experiment 2	55
6.5	Detector Experiments	57
6.6	Experimental Results	59
6.6.1	Experiment 1	59
6.6.2	Experiment 2	65
6.6.3	Experiment 3	67
6.6.4	Experiment 4	70
6.6.5	Experiment 5	73
6.6.6	Experiment 6	75
7	Discussion and Summary of Results	78
7.1	Limitations	79
7.2	Future Considerations	80
7.2.1	3-D Source Localization	81
7.2.2	Multiple Source Localization	81
7.2.3	Certainty of Detection for Moving Detectors	82

8	Conclusions	83
	References.....	86

List of Figures

Figure 4.1 - Profile and radiographic images of simulated detector	12
Figure 4.2 - Experimental detector with steel table and concrete wall	14
Figure 4.3 - Simulated detector with steel table and concrete wall	15
Figure 4.4 - Comparison of 3x3 NaI detector Cs-137 full energy spectra	16
Figure 4.5 - Comparison of 3x3 NaI detector Co-60 full energy spectra	16
Figure 4.6 - Comparison of 3x3 detector Na-22 full energy spectra	17
Figure 4.7 - Comparison of 3x3 NaI detector energy efficiency using Cs-137, Na-22 and Co-60.....	18
Figure 4.8 - Comparison of 3x3 NaI detector responses as a function of distance	19
Figure 4.9 - MCNPX interface flowchart	21
Figure 5.1 - Regularly spaced detector measurements in the x- and y-directions	22
Figure 5.2 - Positional simulations of Cs-137 on surface and in 3 inches of soil	24
Figure 5.3 - Full positional simulation of Cs-137 on surface.....	25
Figure 5.4 - 10 cm detector spacing grid overlaid on detection efficiency matrix to demonstrate grid pattern	26
Figure 5.5 - Hypothesis testing of source and background distributions.....	28
Figure 5.6 - Example of detector measurement pattern.....	30
Figure 5.7 - Example of detector measurement pattern with offset starting location	31
Figure 5.8 - Example showing every possible starting location for first measurement	32
Figure 5.9 - Dependence of starting location for 10 cm grid spacing on probability of true positive detection.....	33

Figure 5.10 - Detector certainty for 0.662 MeV (Cs-137) in air and soil.....	35
Figure 6.1 - Surveying configuration for localization method	37
Figure 6.2 - 2-D simulated detector efficiency of Cs-137 in air	39
Figure 6.3 - 2-D simulated detector efficiency of Cs-137 in air with large values masked	39
Figure 6.4 - 2-D map of simulated detector efficiency of Cs-137 in soil	40
Figure 6.5 - Simulated detector efficiency of Cs-137 in soil at multiple depths.....	41
Figure 6.6 - Four detector measurements for a source at relative location $x = 23$	42
Figure 6.7 - Example comparison between measured data and the simulated data at 1 cm depth.....	43
Figure 6.8 - Example comparison between measured data and the simulated data at 2 cm depth.....	44
Figure 6.9 - Chi-square mapping showing source localization	45
Figure 6.10 - Contours demonstrating change in chi-square values	46
Figure 6.11 - ± 1 standard deviation confidence interval for simulated Cs-137 in air (1 reading)	47
Figure 6.12 - ± 1 standard deviation confidence interval for Cs-137 simulated in air (2 readings).....	48
Figure 6.13 - ± 1 standard deviation confidence interval for Cs-137 simulated in air (3 readings).....	49
Figure 6.14 - ± 3 standard deviation confidence interval for Cs-137 simulated in air (3 readings).....	50
Figure 6.15 - Overlap of confidence intervals.....	51

Figure 6.16 - Contour plot showing spatial probabilities for multiple simulated detector readings.....	52
Figure 6.17 - Simulated chi-square results of Cs-137 in air using four measurements	53
Figure 6.18 - Simulated contours for Cs-137 in air using four measurements	54
Figure 6.19 - Contour plot of Cs-137 in air using four simulated measurements.....	55
Figure 6.20 - Simulated experiment of Na-22 in soil using three measurements	56
Figure 6.21 - Chi-square contours of simulated experiment for Na-22 in soil	56
Figure 6.22 - Simulated contours for Na-22 in soil using three measurements	56
Figure 6.23 - Contour plot of Na-22 (0.511 MeV) in soil using three simulated measurements.	57
Figure 6.24 - Experimental setup for 3x3 NaI detector and source	58
Figure 6.25 - Experimental setup with sand	59
Figure 6.26 - Fit between experimental and expected measurements for Cs-137 in air....	60
Figure 6.27 - Experimental chi-square results of Cs-137 in air using three measurements	61
Figure 6.28 - Experimental chi-square results of Cs-137 in air using three measurements	62
Figure 6.29 - Relative uncertainty of simulated detector efficiency in air using a 187,353 Bq Cs-137 source with a ten second counting time	63
Figure 6.30 - Experimental contours for Cs-137 in air using three measurements.....	64
Figure 6.31 - Contour plot of Cs-137 in air using three measurements.....	64
Figure 6.32 - Experimental chi-square results of Cs-137 in air using four measurements	65
Figure 6.33 - Experimental contours for Cs-137 in air using four measurements	66

Figure 6.34 - Contour plot of Cs-137 in air using four measurements.	67
Figure 6.35 - Experimental chi-square results of Na-22 (0.511 MeV) in air	68
Figure 6.36 - Experimental contours for Na-22 (0.511 MeV) in air using three measurements	68
Figure 6.37 - Contour plot of Na-22 (0.511 MeV) in air using three measurements.	69
Figure 6.38 - Experimental chi-square results of Na-22 1.274 MeV peak in air	70
Figure 6.39 - Experimental contours for Na-22 (1.274 MeV) in air using three measurements	71
Figure 6.40 - Contour plot of Na-22 (1.274 MeV) in air using three measurements.	72
Figure 6.41 - Experimental chi-square results of Na-22 0.511 MeV peak in soil.	73
Figure 6.42 - Experimental confidence rings of Na-22 (0.511) in soil	74
Figure 6.43 - Contour plot of Na-22 (0.511 MeV) in soil using three measurements.	74
Figure 6.44 - Experimental chi-square results of Na-22 1.274 MeV peak in soil.	75
Figure 6.45 - Relative error contours of 142,805 Bq Na-22 (1.274 MeV) in soil using 120 second counts.....	76
Figure 6.46 - Experimental confidence rings of Na-22 (1.274 MeV) in soil	76
Figure 6.47 - Contour plot of Na-22 (1.274 MeV) in soil using three measurements.....	77

List of Tables

Table 6.1 - Actual versus extracted results in air73

Table 6.2 - Actual versus extracted results in soil.....77

List of Appendices

Appendix A: Detector Theory of Operation	89
Appendix B: Photon Transport in MCNPX	91
Appendix C: Photon Interactions in MCNPX	93
Appendix D: MCNPX Photon Transport Logic	97
Appendix E: MCNPX Input Files	99
Appendix F: Matlab Programs	106

Chapter 1

Introduction

Detecting surface and sub-surface radiological contaminants using uncollimated solid-crystal gamma detectors is the standard for remediation of gamma-emitting contamination. This method has been used to support the removal of discrete radioactive sources as well as diffuse contaminants existing in or on surfaces, soil, and concrete.

One of the biggest challenges when addressing the detection and removal of low-activity fragments is quantifying the uncertainty of detection. This uncertainty strongly depends on the spatial coverage of measurements, the source activity, and the detection efficiency for the contaminant of interest. Commonly, estimates of detection certainty are made based on analytical calculations of known attenuation properties of media and the radioactive decay properties of the contaminant including photon energies. Calculations, however, can become tedious and inaccurate when accounting for the solid angle and attenuation properties of a detector due to the incident photon angles relative to the detector.

A challenge when dealing with the removal of low-activity fragments is determining the location of the source. Because the activity of the source is typically not

known, localization techniques using attenuation properties are difficult to implement, especially when the source is within a medium other than air.

The first part of this thesis presents a method for determining the probability of detecting a known gamma-emitting point source based on a grid pattern of static detector measurements. The method uses the Los Alamos Monte Carlo N-Particle transport code (MCNPX) for calculating the interaction probability.

The second part of this thesis presents a method for determining the position, depth, and activity of a point source based on data from several evenly-spaced static measurements. Localization and source strength are obtained in less than a second by determining the best fit between experimental data and simulated data. Multiple simulations are performed and a best fit determination made, which is based on the relative responses at different detector locations rather than the amplitude. From this best fit, the corresponding source strength can be extracted. The method is intended to be a simple, yet effective process for use in real-time scenarios. Experiments were performed to test the method, and as in part one, MCNPX is utilized for calculations.

This thesis uses the 662 keV energy (Cesium-137) for the majority of calculations and experiments; however, both methods are suitable for any gamma-emitting point source, any solid-crystal detector size, and any transport medium given adequate statistics.

1.1 Motivation of Work

The characterization and clean-up of radiologically contaminated sites has become a frequent activity around the world. The need stems from a variety of reasons;

the most common being that the contamination occurred long before such materials were regulated and now are presumed to present an unacceptable human risk. The contamination may be present due to a result of medical applications, weapons testing, as a byproduct of mining, or academic research. With strict regulations in place, the need to verify that contamination is within regulatory guidelines or below detectable limits is necessary, especially when the plans for the property include new applications and uses. In most cases, the history of the property being remediated is well known and therefore the unknown is not what radionuclide will be found, but where, and how much. In cases where the radionuclide is contained in a discrete source within the medium, it is generally more cost effective to remove the source rather than excavate the surrounding medium due to labor and the high cost of waste disposal. The process of removing non-diffused sources has proven to be an effective method in remediation scenarios. For example, in a project of depleted uranium recovery at Sandia National Laboratory, personnel used low-energy gamma detectors to detect and remove small fragments of depleted uranium in soil [1]. Significant cost savings were evident when separating the DU from the soil rather than treating all soil as contaminated waste.

1.2 Outline of Work

This thesis is broken into two primary parts, however many steps were taken to obtain the data used for each part.

Prior to discussing the methodologies of each part, Chapter 2 outlines and discusses some other methods commonly used for the detection and localization of sources. Chapter 3 then summarizes the instruments utilized for this work.

MCNPX simulations were vital to the process of both methods so much work was performed to compare how the simulated data compared to that of an actual detector. Chapter 4 presents the steps taken to validate the responses. Chapter 4 also discusses the MCNPX interface which serves as a tool to both iterate the simulations, and allow persons not familiar with MCNPX to use both methods.

Chapter 5 uses the tools created in Chapter 4 to solve the first problem, which is essentially whether or not the source will be detected, and with what certainty. Chapter 5.1 - 5.3 discuss the methodology involved, and Chapter 5.4 presents the results of the simulations.

The second problem is introduced in Chapter 6 and solves the second problem, which is determining where the source is located within a medium, and with what activity. Chapter 6.1 - 6.3 discuss the methods. Simulated results are presented in Chapter 6.4. Following a discussion of experimental techniques in Chapter 6.5, experimental results are presented in 6.6.

Finally, Chapter 7 summarizes the results, discusses the limitations in both methods, and outlines potential future work. The work is concluded in Chapter 8.

Chapter 2

Literature Review

There has been much work in the field of source localization methods and detection capabilities. Prior to discussing the novel methods of this thesis, this chapter reviews the work and the findings of other methods utilized.

2.1 Source Localization Techniques

Several localization techniques have been employed for both radioactive and inert objects.

The difference of time-of-arrival (DTOA) is a commonly used method in applications such as aerospace and radio frequency networks for positioning as described in [2], [3] and [4]. DTOA applications take advantage of time of propagation and have been solved and utilized using mathematical models to triangulate a position. These techniques are difficult to implement when dealing with photons at the speed of light due to the timing accuracy required of instrumentation. This method is also inappropriate for localizing radioactive sources as the randomness of radioactive emission can have

catastrophic results on DTOA and geometric DTOA, particularly when dealing with low level sources where statistics have a higher uncertainty [5].

Another common method of localization uses the inverse-square law properties of an isotropic point source to relate the source to detector distance to the number of photons hitting a detector as demonstrated in [6]. The authors of [7] use this method to track a source in a room given the initial source position. Readings from four detectors were used to solve a nonlinear recursive least squares optimization problem utilizing a sequential quadratic program. The inverse square method typically limits the attenuation medium to air or very low density material. The strength of the source or the initial position of the source must also be known for accurate calculations.

Angle-of-arrival (AOA) is another method that utilizes the isotropic emission pattern as presented in [8]. Using multiple detectors that are angularly dependent, the location of the source can be approximated by the direction at which the photons hit the detectors. The method is also suitable for localizing a source within a medium; however it still requires angularly dependent or collimated detectors. The use of collimated detectors, however, results in a lower efficiency due to a lower number of photons incident on the detector.

Other methods, such as [9] have been very successful in using the Compton scatter process to localize a source. The method can extract the angle of the scattering and define a conical volume which contains the source. The projection of many cones will then overlap at a common point being the source location. This method also results in lowered detection efficiency and requires expensive equipment.

Like the localization method, there have also been studies and experiments to quantify detector measurement capabilities. The next section discusses the prior work.

2.2 Determination of Detection Capabilities

Many theoretical models exist to determine the probability of existence of radioactive sources and to address the minimum detectable limits. The author of [10] incorporates a mathematical model to determine the probability of finding a hot spot based on the density and pattern of the grid points used for sampling. Another author [11] builds on this model to account for a moving detector. Both models assume that the hot spot is a surface area source and that the number of counts per unit area per unit time by the detector is known preceding the calculation.

MCNPX has become a common tool in modeling of detection capability. However, the documented experiments are primarily limited to specific situations. For instance, the authors of [12] use MCNP to model the detection capabilities of NaI sensor systems from a helicopter. The work focuses on the measurement of high activity gamma sources through several mean-free paths of air. The authors of [13] modeled and verified the detection capability of a moving low-energy detector for an Am-241 source at different depths within soil. The method used the Electromagnetic Shower Simulation (EGS3) program for the Monte Carlo simulations. The model assumed a moving detector by modeling the theoretical point source as a line with the length dependent on the counting interval. It was concluded that a rough estimate of the scanning efficiency could be provided from the simulation.

The following chapters will present methods for the detection and localization of radioactive sources that can be used in a variety of scenarios.

Chapter 3

Background

This chapter provides a summary of the instruments used in this thesis.

3.1 Gamma Radiation Detectors

Gamma radiation frequently accompanies the emission of alpha and beta radiation, yet is much more penetrating, making gamma detection a common method for finding sources at large distances or through media. Inorganic scintillators are excellent for gamma detection and spectroscopy due to their high-Z constituents. All calculations performed in this thesis use the response and the simulated response of a NaI crystal scintillator for gamma detection. A detailed description of detector theory of operation is presented in Appendix A.

3.2 The Monte Carlo Transport Method

The Monte Carlo method is widely used for solving problems involving statistical processes and has become increasingly popular for modeling radiation particle transport. The Monte Carlo simulation tracks the paths of millions of particles by probabilistic

interactions using a random number generator and tabulated data. When a large number of particles are tracked from birth to death (interaction or leaking from the system), the average behavior of the system is characterized by utilizing the central limit theorem. This makes the Monte Carlo method well suited for particle transport because, unlike a deterministic method, there are no averaging approximations made in space, energy, or time [14]. This allows a detailed physical representation of each particle making up the system.

All simulated calculations in this thesis were performed using the photon transport option of MCNP, therefore a detailed description of the photon physics and interactions is explained in Appendices B, C, and D.

Chapter 4

Monte-Carlo Techniques and Validation

This chapter discusses the experimental setup and preliminary steps taken to obtain results.

4.1 Detector Simulation

For all calculations and experiments, a cylindrical 3 inch diameter by 3 inch height Sodium-Iodide (NaI) detector was used due to its availability for experiments as well as its high efficiency at the relevant photon energy range. These detectors are commonly used for environmental remediation work. A simplified model of the detector was constructed in MCNPX. The simulated detector is shown in Figure 4.1 and was modeled based on the Ortec model 905-4 specifications. It consisted of the NaI crystal, shown in yellow, and encased in aluminum with a shell thickness of 0.0508 cm. The photomultiplier tube was omitted from the simulated detector as it has a negligible effect on the full energy. The geometry of the detector was also simplified by assuming a constant width for the entire detector housing. All MCNPX input files are given in Appendix E.

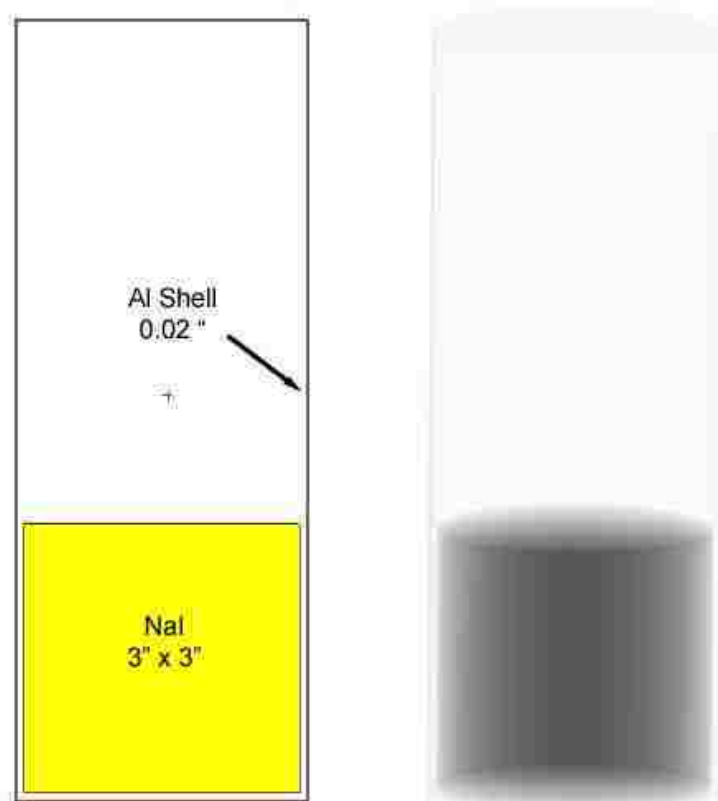


Figure 4.1 - Profile and radiographic images of simulated detector

The analog model was used for all simulations performed in MCNPX. The analog model is the commonly used Monte Carlo model for photon particle transport. It uses tabulated probabilities that various events occur, which are analogous to naturally occurring radiation transport. To determine the number of photons hitting the detector, the MCNPX Pulse Height Tally F8 option was used for all simulations. The pulse height tally is analogous to a physical detector and presents the total energy deposited in a detector, in the specified channels, by each particle history. In addition, the MCNPX detailed physics model was implemented for all simulations, which included coherent (Thomson) scattering and fluorescent photons from photoelectric absorption [14].

Because the simulation time was an extremely important factor in the calculations, electron transport was turned off. In this case, rather than track each individual electron, MCNPX uses a thick-target bremsstrahlung model. Electrons are still generated from interactions, however the model assumes that they are locally slowed to rest, neglecting the time consuming electron transport. Any bremsstrahlung photons are assumed to inherit the direction of the parent electron and are included in the photon transport calculations.

In addition to the tallied result of the simulation, MCNPX also records the relative error, defined as approximately $R \sim 1/\sqrt{N}$. As discussed in the manual, the tally only has meaningful results if the relative error is less than 0.1 [14]. Tallies that exceed this suggested threshold are omitted programmatically from calculations.

4.2 Detector Simulation Validation

Prior to data analysis, the MCNP model output was compared against data collected using the experimental setup to verify that the detector and the simulated detector were similar in response. Much work has been performed to verify similar experiments [15][16][17][18]; however because different detectors respond differently, the method serves as validation for individual scenarios. Spectra were obtained using an optics table and a minimum live counting time of 300 seconds, however most spectra were counted for 3,600 seconds to obtain good counting statistics. A background spectrum was also obtained on the same day of each experiment to obtain more accurate results. The counts of the energy peaks were separated from the background counts using

the trapezoidal background approximation [19]. The activities of the sources were calculated on a daily basis to account for radioactive decay.

The full energy spectrum of three common radionuclides were analyzed experimentally and then simulated using MCNPX. The Gaussian energy broadening (GEB) feature in MCNPX was utilized to simulate the broadened energy resolution exhibited in physical detectors [15]. To verify the secondary photon interactions in MCNP, the physical surroundings of the experimental setup were modeled. This model included the steel optics table beneath the detector and the concrete wall behind the detector. The setup for the experimental detector is shown in Figure 4.2. The MCNPX simulation is shown in Figure 4.3.



Figure 4.2 - Experimental detector with steel table and concrete wall

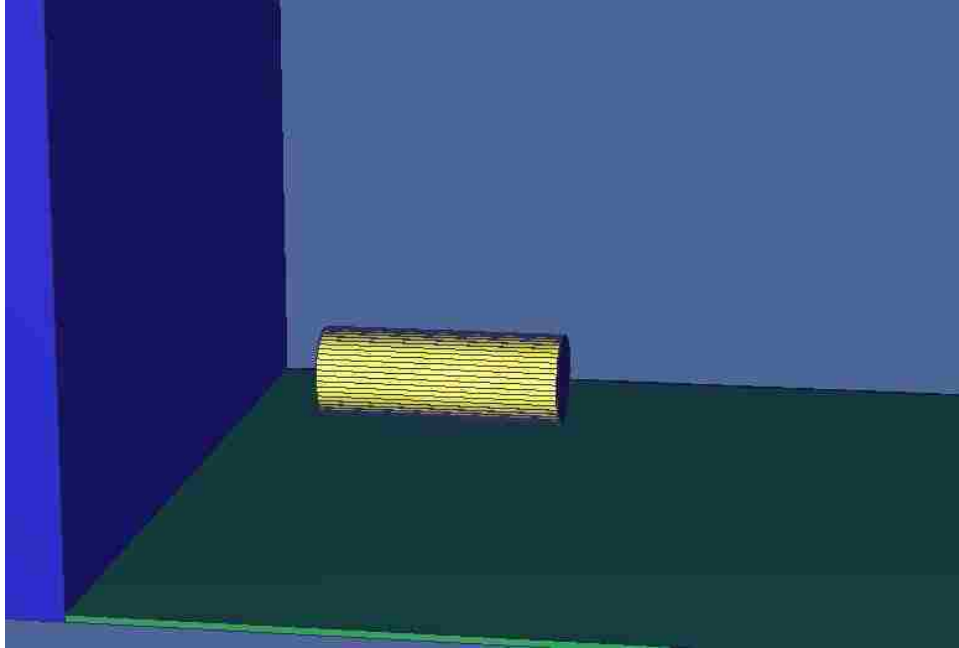


Figure 4.3 - Simulated detector with steel table (bottom) and concrete wall (left)

The sources were measured at 15.24 cm (6 inches) in attempt to lessen dead-time of the detector. The experimental spectra were collected for 3,600 seconds and the simulated spectra consisted of 100,000,000 histories. The resulting responses for Cesium-137, Cobalt-60, and Sodium-22 are presented in Figure 4.4, Figure 4.5, and Figure 4.6.

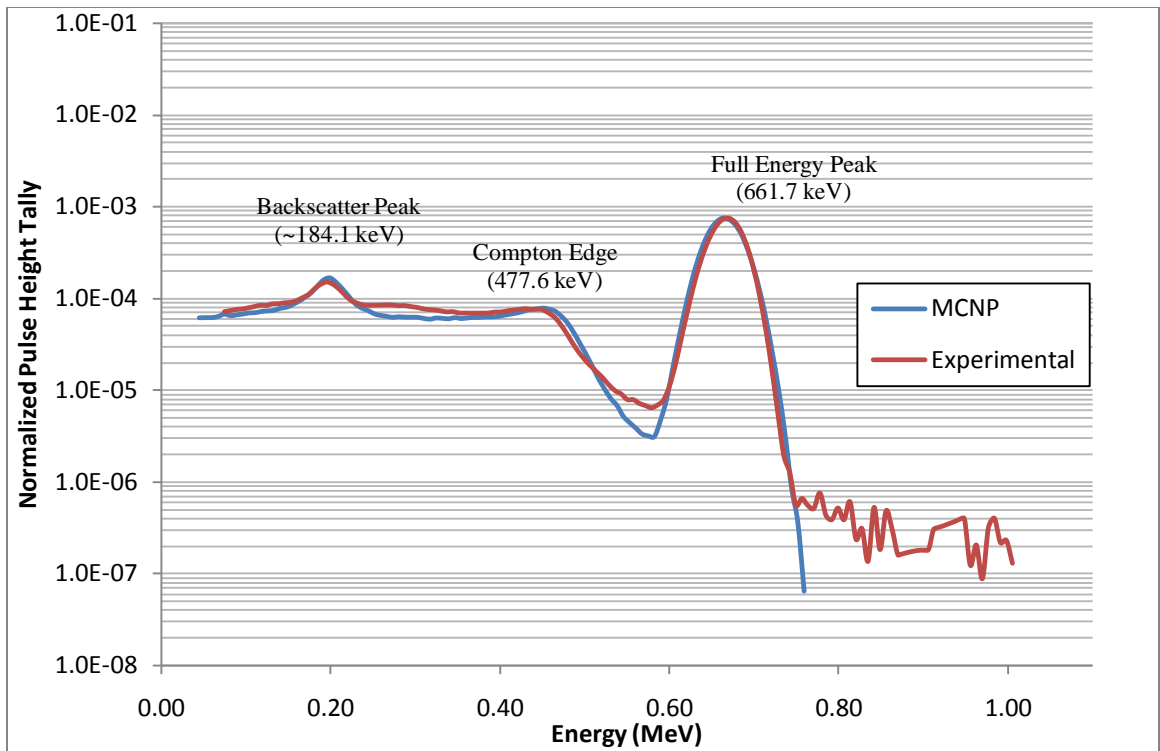


Figure 4.4 - Comparison of 3x3 NaI detector Cs-137 full energy spectra

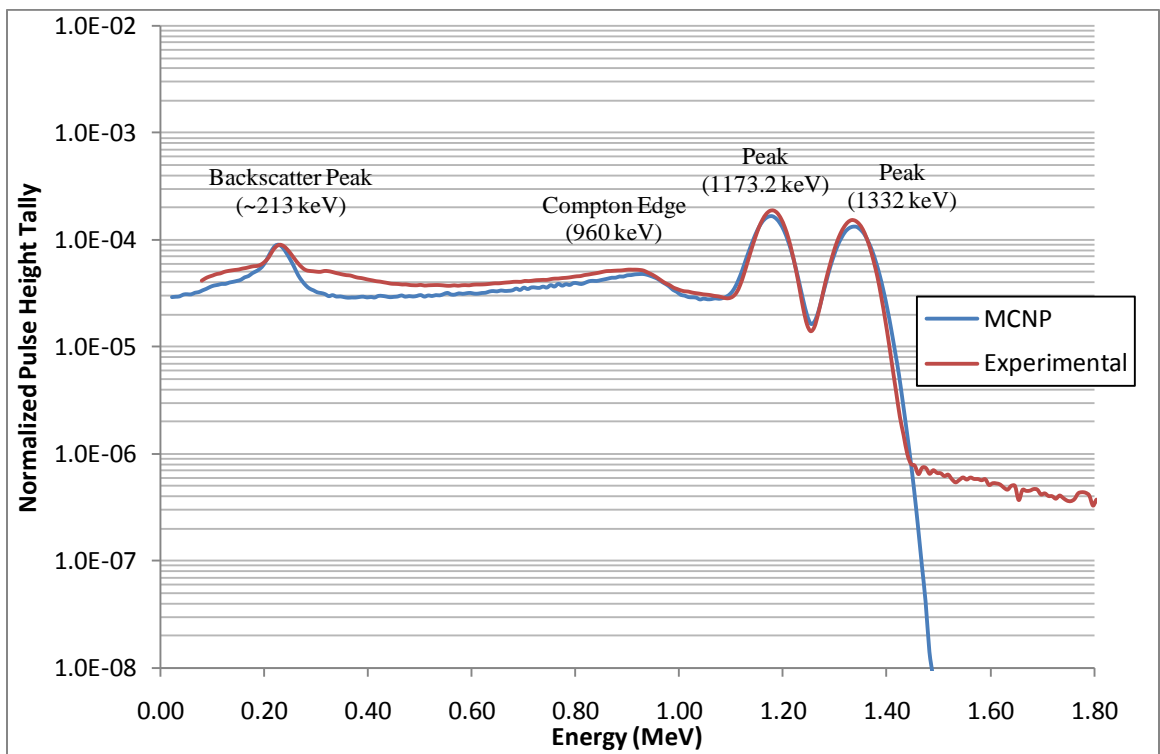


Figure 4.5 - Comparison of 3x3 NaI detector Co-60 full energy spectra

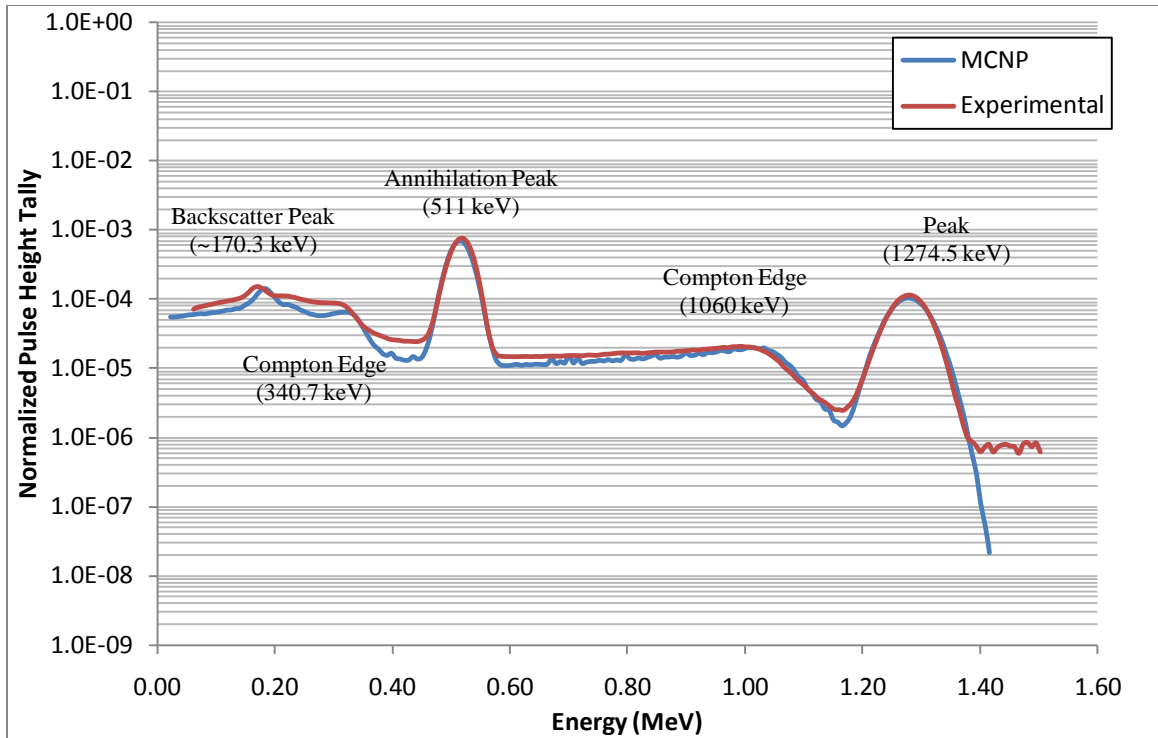


Figure 4.6 - Comparison of 3x3 detector Na-22 full energy spectra

The comparison yielded good results between the experimental and simulated spectra. Small variations in the peak heights were present between radionuclides, however the characteristic energy peaks remained proportional, implying a small uncertainty error in the source activity or geometry. The full peak efficiency was also compared between physical detector response and MCNPX. A source at a distance of 15.24 cm from the detector face was simulated at energies varying from 10 keV to 2 MeV in 10 keV steps to determine the energy response of the simulated 3x3 sodium iodide detector. The same test was performed using the physical detector at several energies from the available sources. The results are shown in Figure 4.7. Results indicate a good comparison between the simulated and experimental energy responses.

Error bars represent a 5% uncertainty of the experimental source calibrations which are assumed to dominate the experimental uncertainties.

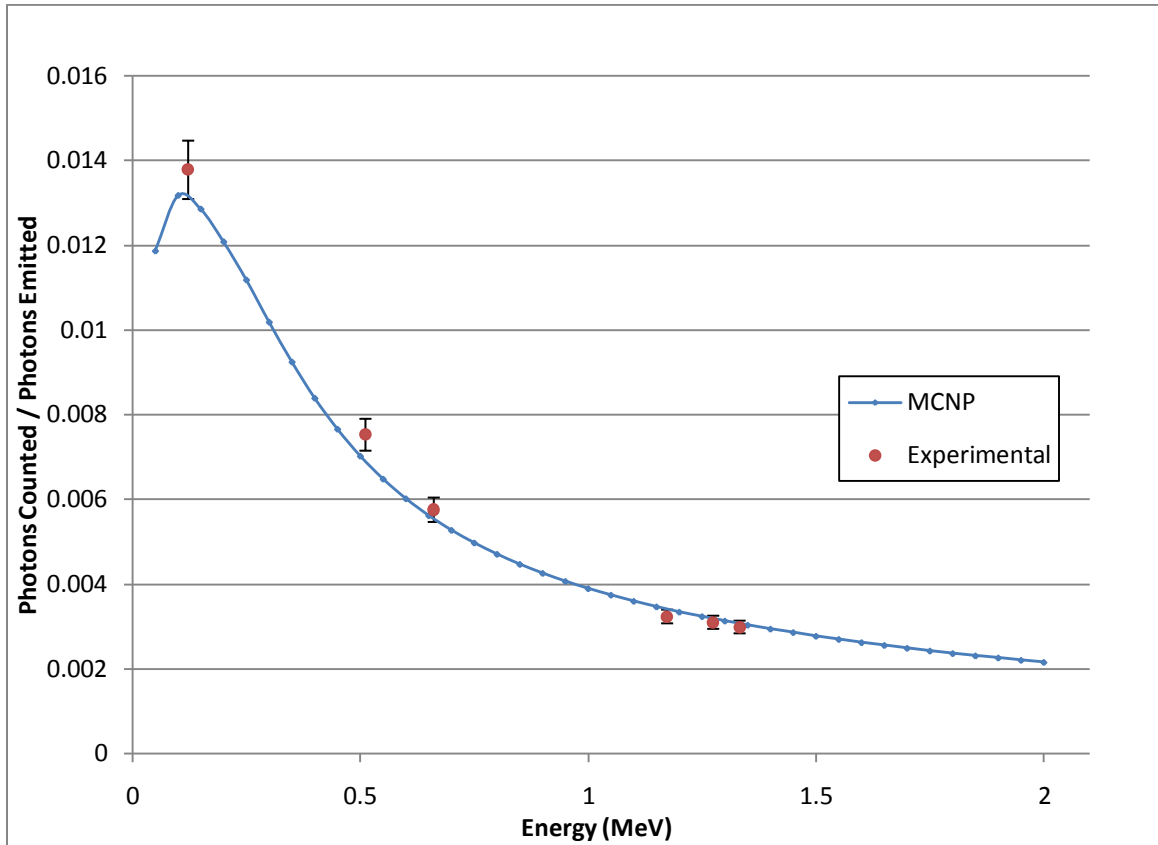


Figure 4.7 - Comparison of 3x3 NaI detector energy efficiency using Cs-137, Na-22 and Co-60

Because depth measurements are important to this thesis, the detector response as a function of source distance was obtained and compared with the simulated response. Only the 662 keV of cesium-137 and the 1332 keV of cobalt-60 energy peaks were obtained experimentally to avoid the error involved in subtracting out the Compton continuum counts. The source was counted in one-inch increments from near contact to 28 cm (~11 inches) from the face of the detector. The experiment was then modeled in MCNP from a distance of 1 cm to 30 cm. The solid angle of the detector was calculated

analytically in both cases to approximate the number of photons hitting the face. Results are shown in Figure 4.8. As with the energy spectra and the efficiency as a function of energy, the simulated detector responses as a function of distance along the axis compare well with experiment.

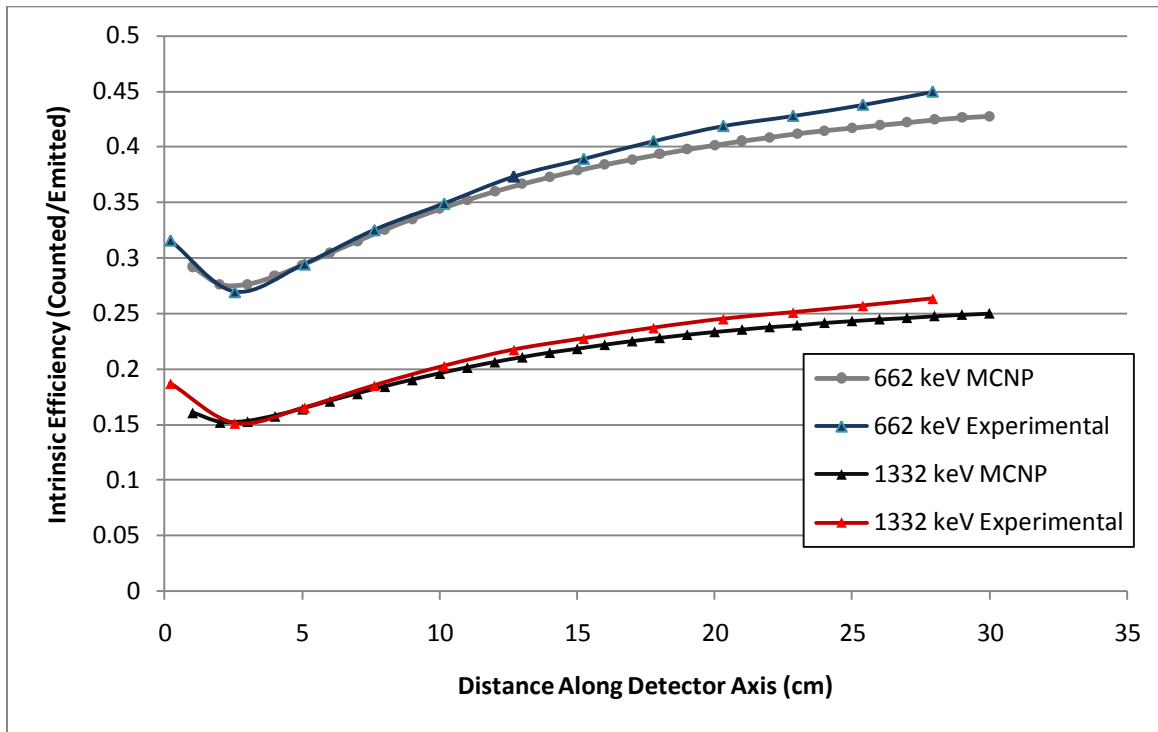


Figure 4.8 - Comparison of 3x3 NaI detector responses as a function of distance

4.3 MCNP Interface and Automation

Both parts of this thesis use a simulated matrix of detector efficiencies at varying source locations. Essentially, each reading in the matrix is the MCNPX result of a detector above some media with the source at some location within the media. For high

density matrices, several hundred thousand MCNPX simulations (each simulation consisting of several million particle histories) were performed.

Currently, there is no way to iterate an MCNPX simulation through the input cards. For a large number of iterations, the time and effort involved in modifying input files and recording the result after each subsequent simulation is very time consuming.

For this work a console-based program was written to automate the process. The program, written in a combination of C and Basic, modifies the relevant input parameters of the designated MCNPX input file, and then passes it into the FORTRAN compiler. Once the simulation is complete, the necessary portion of the output file (tally tables, relative error, and statistical errors when present) is written to a single file. This process is repeated until the defined energy range or positional range was completed. In addition, the MCNPX structure was written in ANSI-Standard FORTRAN 90 language and processes input cards using dynamically allocated storage with globally shared FORTRAN 90 modules [20]. This structure allows multiple MCNPX processes to occur in parallel using a single computer. By using a quad core computer, four different independent processes were performed simultaneously to achieve results in one-fourth the time.

A second function of the program is to simplify the complexity of the MCNPX input geometry card. Because the intent of this thesis is to provide a method for multiple scenarios, the program also modifies the basic geometry parameters according to the surveying conditions. Rather than re-write MCNPX input cards, a user only needs to enter the height of the detector above the media, the type and density of the media, and the radionuclide. In addition, the MCNPX geometry card parameters of commonly used

detectors may be stored in the program and become a selectable parameter. The entire process allows MCNPX to be used in an iteration process without modifying the original FORTRAN code. The general flowchart of the process is shown in Figure 4.9.

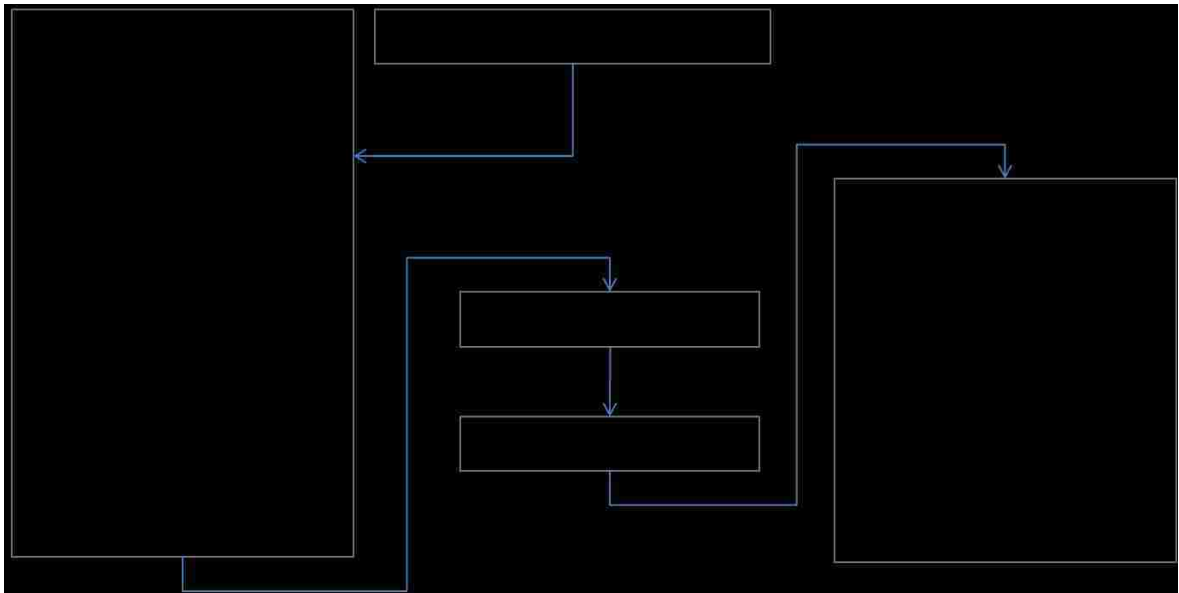


Figure 4.9 - MCNPX interface flowchart

The total simulation computation time varies significantly between scenarios. Models that only use the characteristic energy peak, for example, are drastically faster than simulating the full spectra. By killing photons that fall below the desired energy, it was determined by trial that millions of histories can be simulated in a few seconds. For all simulations in this work, an AMD Phenom X4 9150e quad core processor and 4GB DDR2 memory were used.

Chapter 5

Detection Certainty of Source

The first part of this thesis investigates the probability of detecting a known low-activity radionuclide with known parameters. The problem serves as a method to determine whether a source will be detected given several parameters. The method assumes several equally spaced static measurements are taken in an area of interest containing a point source as shown in Figure 5.1.

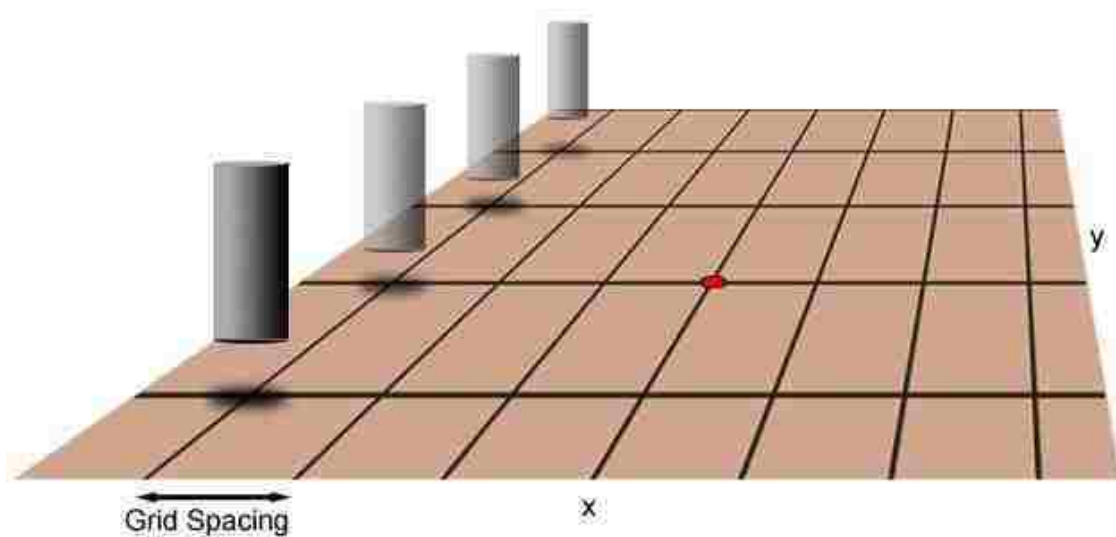


Figure 5.1 - Regularly spaced detector measurements in the x- and y-directions

Contrary to the figure which only shows one row of measurements, the survey pattern assumes that the detector measurements are taken at every node defined by the grid spacing length. That is, detector positions are spaced regularly in both y and in x . Given the depth at which the source is contained in the medium and the strength of the source, the overall probability of detecting true positives for the source from all measurements can be obtained. The probability of detection is based on several factors such as the background counts, the spatial density of the static measurements, and the counting time of each measurement.

5.1 Simulated Efficiency Mapping

The first step in understanding the probability of detection is to understand the detection efficiency as a function of detector and source position. The MCNPX recursion process, described in section 4.3, is first used to model the response of a detector at a constant height above a surface, with the source at a constant height beneath or on the surface. The response is simulated at every location in the area starting at location $(x, y) = (0, 0)$, which assumes the detector is directly above the source, and moves outward in the x and/or y directions in one centimeter increments. The bounds of the simulated area are dependent on the transport medium and the strength of the source. For work in this thesis, only the full energy peak is analyzed, however the method is equally suitable for the full spectra. The response is therefore defined as the number of full energy photons counted divided by the number emitted isotropically by the source, the detection efficiency. Using the full spectrum is more suitable for typical field detectors where a discriminator is not typically used, however doing so results in a loss of efficiency. For a

cylindrical detector, it is assumed that the response is symmetric about the central axis of the detector; therefore only one quadrant of the active area is simulated and then duplicated to make up the entire survey area. Figure 5.2 shows two simulated detector responses at 15.24 cm (6 in) above a soil surface. The top grid represents a 0.662 MeV (cesium-137) surface source and the bottom grid is the same source, but 7.62 cm (3 in) beneath the soil. Figure 5.3 demonstrates the full surface source response from the point (0, 0) to 30 cm outward in both the x and y directions. The simulated grid response of the detector with the desired parameters is then used to estimate the probability of detection based on a second set of parameters.

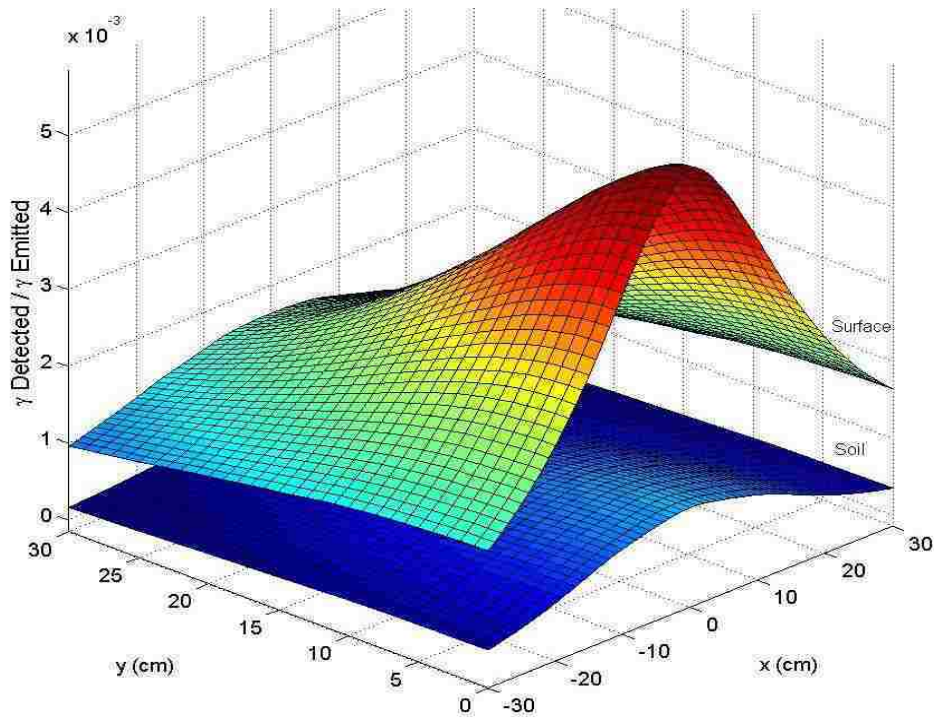


Figure 5.2 - Positional simulations of Cs-137 on surface and in 3 inches of soil

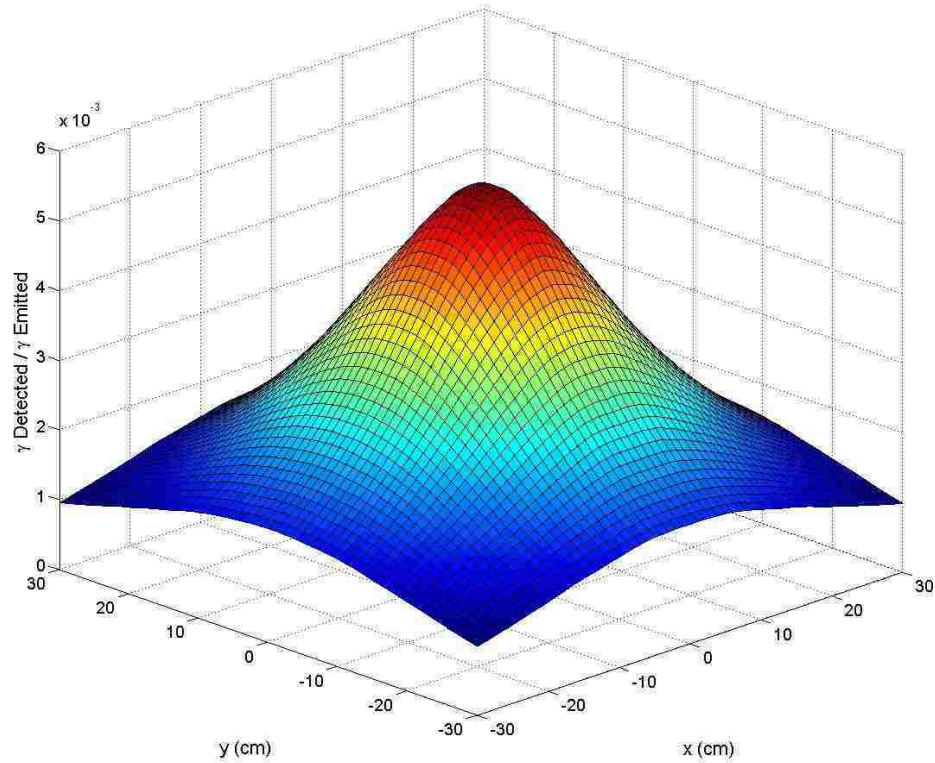


Figure 5.3 - Full positional simulation of Cs-137 on surface

The problem assumes the grid of static measurements covers the entire sampling area. Measurements are taken for some counting time, assuming enough for good statistics, and the detector is moved from one user-defined spacing to the next counting location. The process is repeated in both the x- and the y-directions until the entire area has been covered. Figure 5.4 demonstrates a sampling pattern with 10 cm spacing. The effects of varying the user defined spacing and the definition of a lower detectable limit will be addressed in section 5.2.

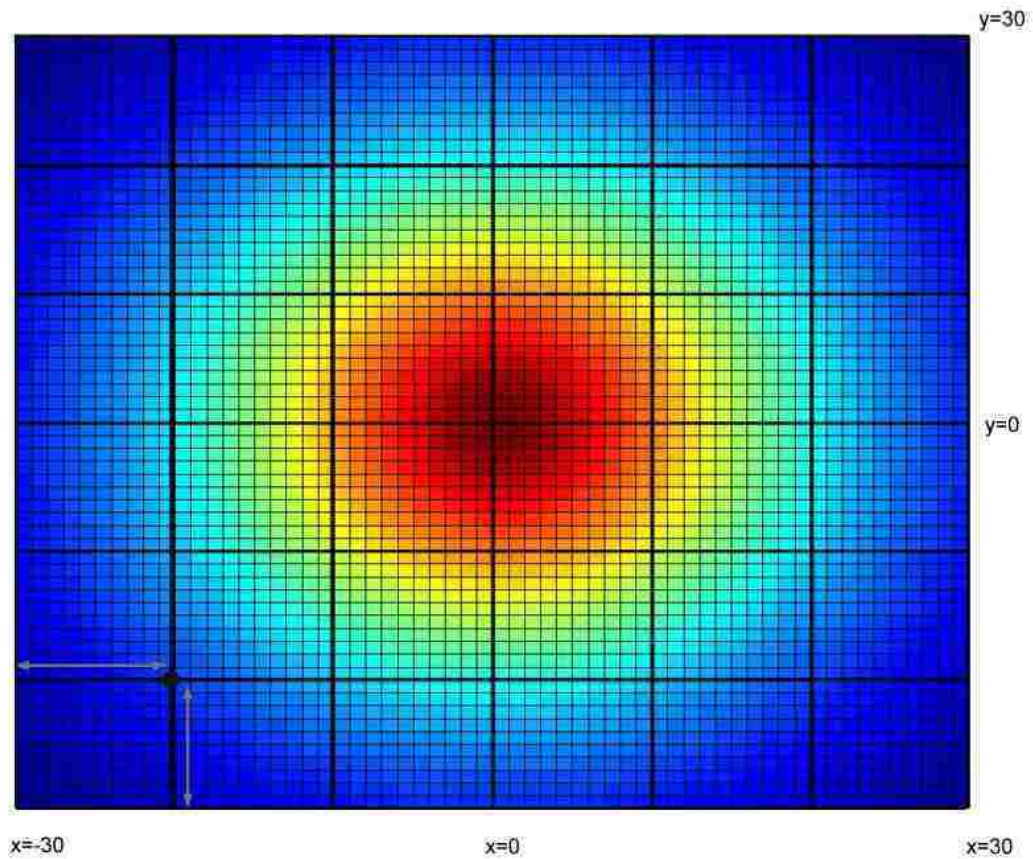


Figure 5.4 - 10 cm detector spacing grid overlaid on detection efficiency matrix to demonstrate grid pattern

5.2 Resolution of Signal from Background

Unfortunately, in a realistic detector system, there is background noise to contend with. The ability to resolve the source counts from the background counts is an important issue, especially when dealing with low net count rates.

Because radioactive decay is a randomly occurring event, it must be described in statistical terms. The statistical variation in the number of counts obtained from a radioactive source is given by the binomial distribution. For larger counts however,

typically equal or greater than 30, the binomial distribution is a very close approximation to the Gaussian (normal) distribution [21]. Because photon counting typically results in counts greater than 30, the normal distribution approximation is used for all counting statistics in this thesis.

An evaluation of the detector simulation above for a cesium-137 source in soil concludes that even at the farthest distance from the detector at $(x, y) = (30 \text{ cm}, 30 \text{ cm})$, a one microCurie (μCi) source would result in approximately 32 characteristic energy counts in one second. This relatively weak source at a far distance and a very short counting time is theoretically detected while also satisfying the threshold for the normal distribution approximation. Unfortunately, outside the simulated world, background radiation plays a large role in the ability to determine the validity of detecting a source. Counts from external sources of gamma radiation (terrestrial and cosmic) will follow the same statistical counting patterns as a source, therefore a method for resolving the two distributions is required.

Figure 5.5 shows the relationship between the background and source distributions. The critical limit L_c , is the smallest value above mean background where a source count can be considered valid with the certainty defined by α and β :

$$L_c = k_\alpha \sigma_b = S - k_\beta \sigma_s$$

k_α and k_β are the number of standard deviations (σ) from the mean. S is the mean of the source counts and B is the mean of the background counts. Using normal distributions, $\sigma_b = \sqrt{B}$ and $\sigma_s = \sqrt{S + B}$. Solving for k_β gives the number of standard deviations (σ_s) from L_c :

$$k_{\beta} = \frac{S - k_{\alpha}\sqrt{B}}{\sqrt{S+B}}$$

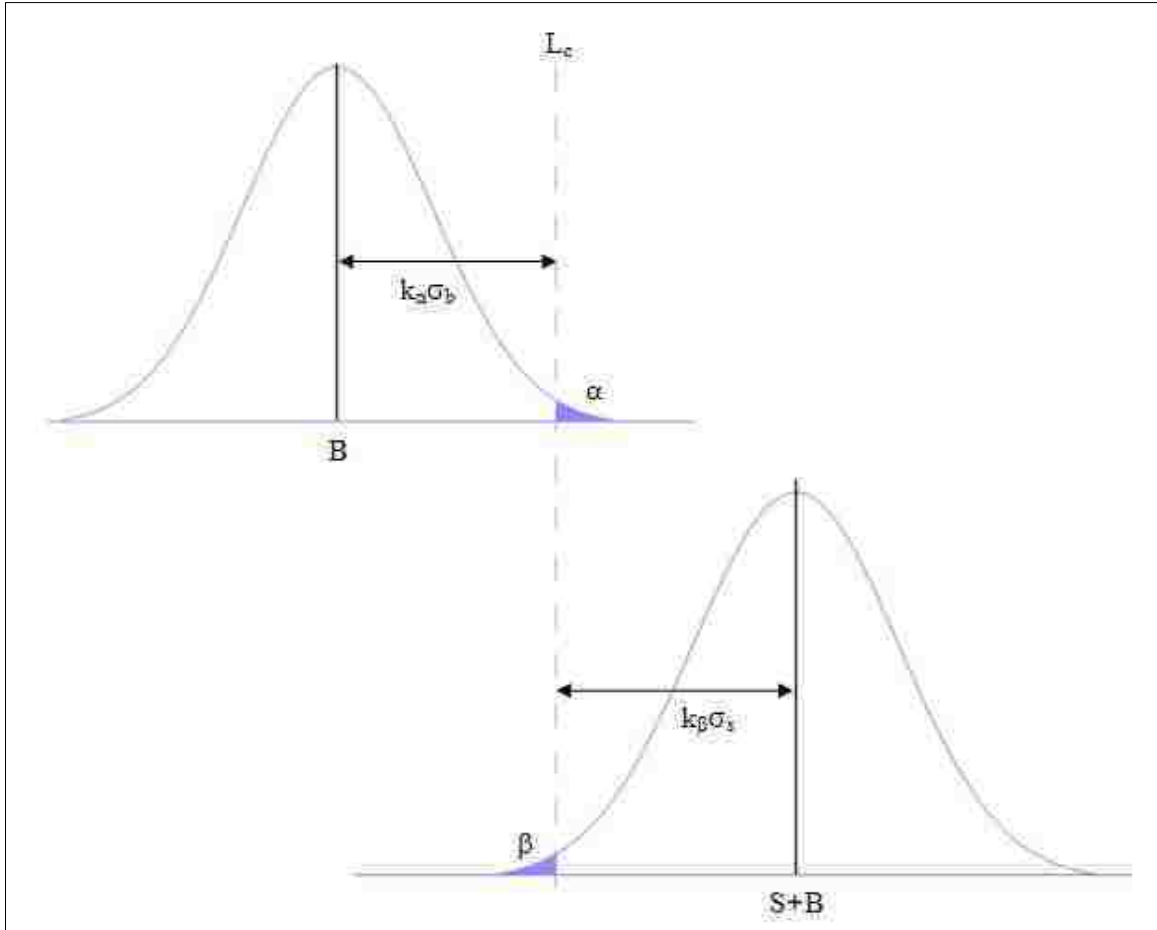


Figure 5.5 - Hypothesis testing of source and background distributions [22]

By acquiring a mean background for the survey area and choosing the desired percentage of false positives (α), L_c becomes a fixed threshold. Values above this threshold are considered statistically a positive reading. Any counts from the source distribution that fall below the L_c threshold, defined by β , cannot be distinguished from background counts with any certainty. The percentage of true positives, defined by $1-\beta$, can be

obtained for any value of S. The number of true positives is determined by taking the standard normal cumulative distribution of k_β :

$$p(k_\beta) = \frac{1}{\sqrt{2\pi}} \int_{-\infty}^{k_\beta} e^{-\frac{t^2}{2}} dt$$

where t is the normal random variable. The process is repeated for every grid location using Matlab. All Matlab programs written for this work are given in Appendix F. Based on the scenario, the percentage of false positives may be varied as a function of the threshold value. By maintaining a cutoff for a low percentage of false positives, the overall certainty of detection is increased significantly, however detection capability is lowered.

The overall probability that the source is not detected at any of the locations in the grid is calculated by taking the joint probability at each detector spacing, S:

$$P(\overline{P_{0,0}} \cap \overline{P_{S_1,0}} \cap \dots \cap \overline{P_{S_n,S_m}}) = [1 - P_{0,0}] [1 - P_{S_1,0}] \dots [1 - P_{S_n,S_m}]$$

the total probability of true positives for the source is then:

$$P(S) = 1 - P(\overline{P_{0,0}} \cap \overline{P_{S_1,0}} \cap \dots \cap \overline{P_{S_n,S_m}})$$

The calculated probability calculated from the surveying pattern shown in Figure 5.4 assumes that the first detector location always occurs on the edge of the grid. This particular detector spacing with the dimensions of the efficiency mapping will always result in a measurement being taken directly over the source. Likewise, a detector spacing of 20 cm would result in the unrealistic scenario of always having two measurements straddling the source. In case of a point source, there is a significant

variation in the detection probability when the detector is offset from the source; the next section addresses this variation.

5.3 Effects of Detector Starting Location

To study the effects of a random starting location, the iteration process is repeated for every one centimeter block between the grid corner and one grid length in the x- and the y-direction. To clarify this concept, Figure 5.6 demonstrates the ideal pattern of detector measurements. The source is represented by the red circle at the center of the grid and one line of measurements at some defined spacing is shown to the left.

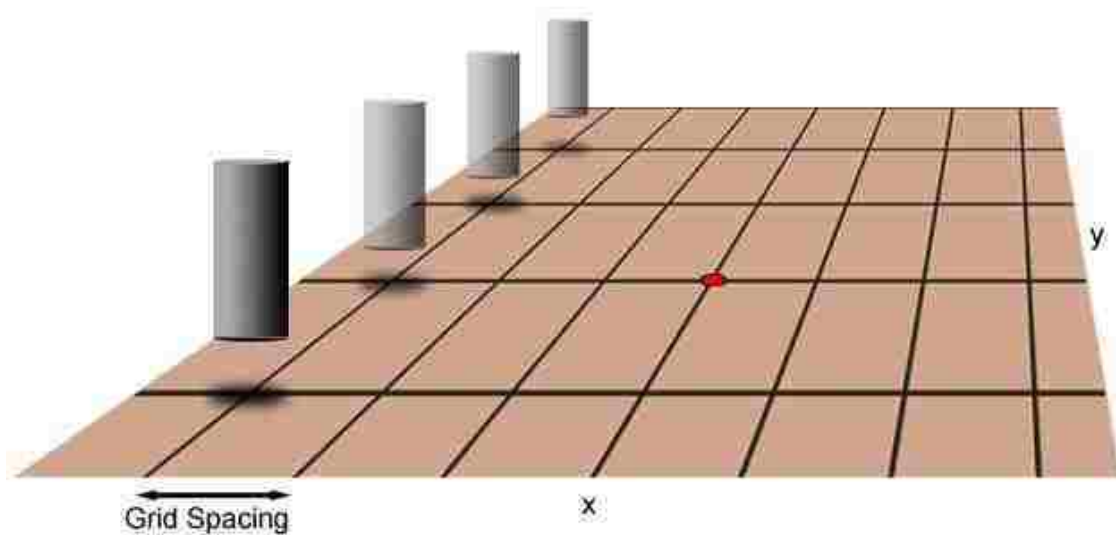


Figure 5.6 - Example of detector measurement pattern

In this example, the starting location of the first detector measurement will result in one measurement landing directly above the source when all measurements have been taken. Realistically, using a grid configuration with a random starting location for measurements

will not always yield a measurement directly above the source. Figure 5.7 shows the same measurement scenario with the same grid spacing and same source location. In this case, however, the starting location is offset by one-half the grid spacing length in the y direction. As a result, rather than have one measurement directly above the source, two measurements straddle the source.

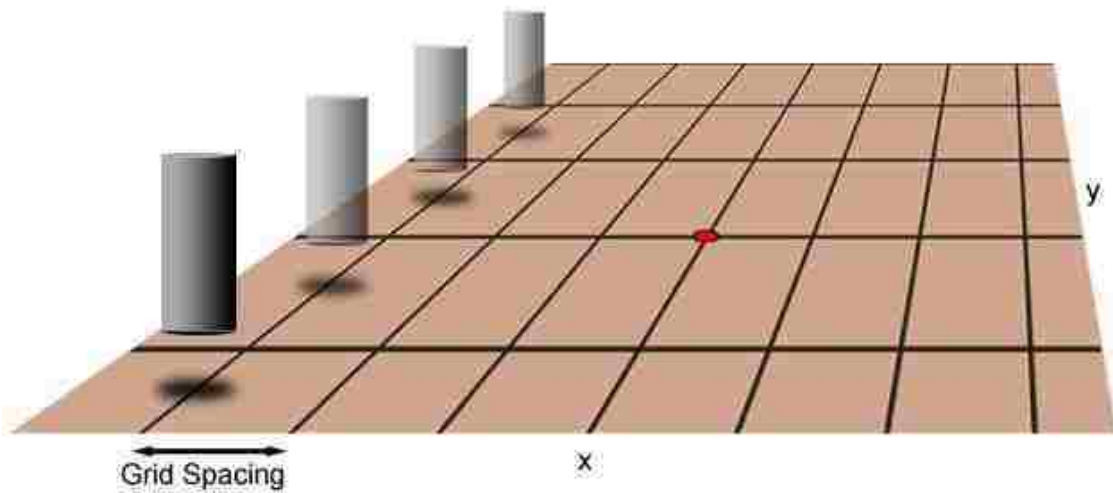


Figure 5.7 - Example of detector measurement pattern with offset starting location

This offset can result in drastic changes of the detection capability, especially when the length of the grid spacing becomes large. To account for the change of probability, every possible starting location, with a resolution one cm, is considered in both the x- and the y-direction. Using the same example above and assuming 10 cm grid spacing, the blue region in Figure 5.8 represents all 100 (10cm x 10cm) possible starting locations. At a length of one grid spacing, the response will repeat assuming the total coverage of detector measurements is maintained.

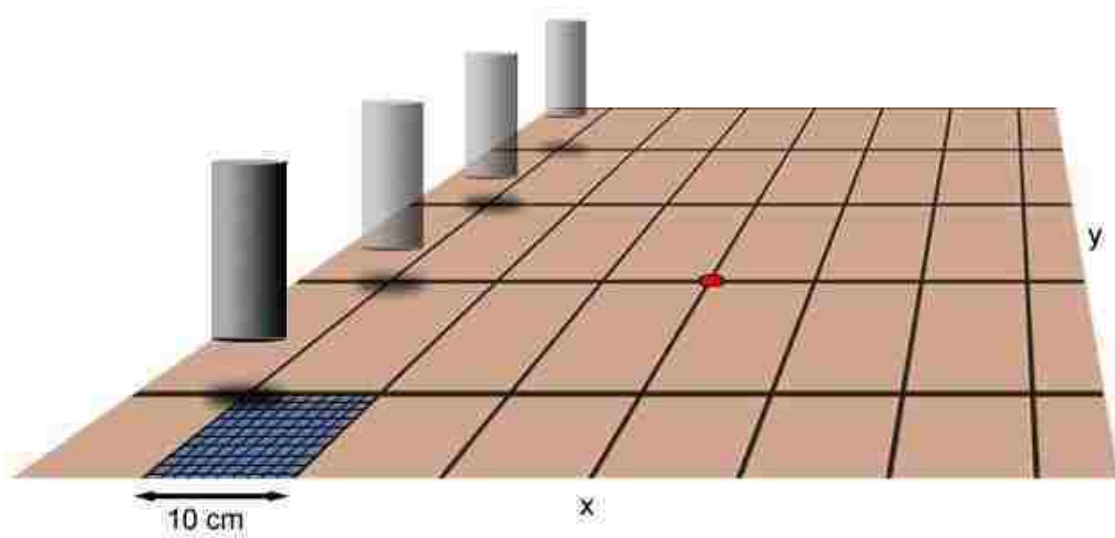


Figure 5.8 - Example showing every possible starting location for first measurement

Figure 5.9, representative of the blue region in the previous figure, demonstrates the variation of the total probability of detecting true positives for every starting location for a $0.3\mu\text{Ci}$ Cs-137 source in soil. The figure response assumes that L_c was set using a laboratory background measurement and the false positive rate at 1%. As expected, starting in the center of a survey grid yields a lower probability because the measurements straddle the source location. In this case the difference of limits is negligible with a minimum probability of 0.845 and a maximum probability of 0.885. Using a larger grid spacing between detectors would result in a much larger variation between the minimum and maximum probabilities.

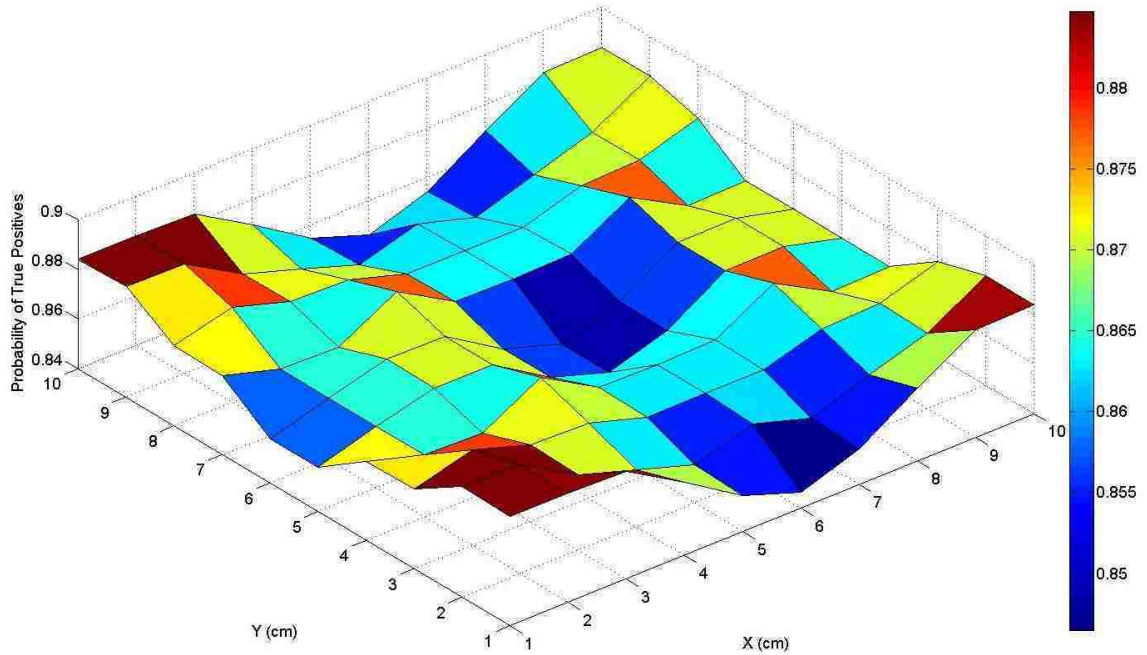


Figure 5.9 - Dependence of starting location for 10 cm grid spacing on probability of true positive detection

The probability of a true positive reading for each starting location is then equally weighted to give a total probability for the entire region as:

$$P = \frac{(P(S)_{1,1} + P(S)_{1,2} + \dots + P(S)_{n,n})}{n^2}$$

for a detector spacing, n , to account for the change in response for different starting positions. The model assumes that the size of the full simulated grid is chosen such that the percentage of true positives is very low at the edges given the desired source and background parameters. For high activity sources, the bounds of the grid could be extended much farther, and the simulated increments would be of lower density.

5.4 Results

The certainty of detecting a Cesium-137 source based on counts of the 662 keV peak was performed in two simulated scenarios. The first scenario consisted of a point source on the surface with the detector at a height of 15.24 cm (6 in) from the surface. The second scenario consisted of the same detector height, but with the source beneath 7.62 cm (3 in) of soil. A mean background of 55 counts per second was obtained experimentally in the detector laboratory. The false positive rate was set to 0.1% and values containing less than 5% true positives were neglected. The method was explained using a 10 cm detector spacing, but simulations were performed for several different spacings. The response of detector measurements for both scenarios is shown in Figure 5.10 using the probability for detection over the entire region, as defined in section 5.3.

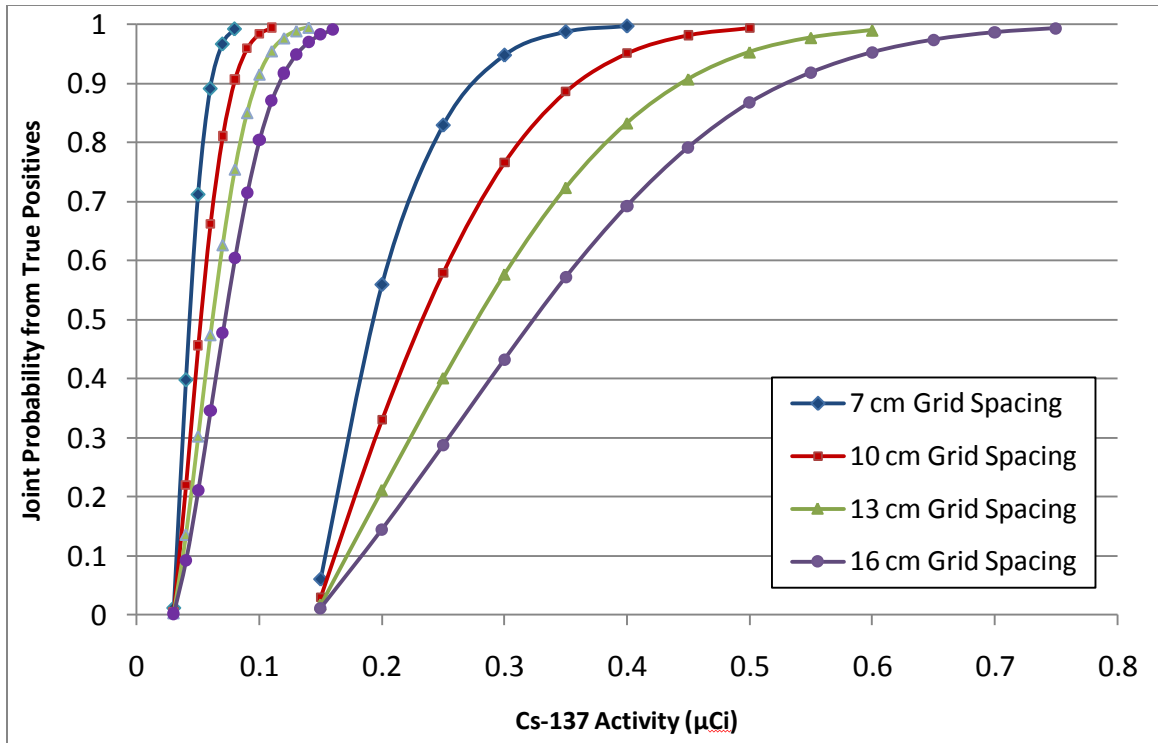


Figure 5.10 - Detector certainty for 0.662 MeV (Cs-137) in air (left) and soil (right)

The graph clearly demonstrates the change in detection based on the detector grid spacing. As expected, a lower activity source can be seen with greater certainty using smaller measurement spacing. Results also indicate that the certainty of detection in air for a 0.03 microCurie (μCi) Cs-137 source will be very low using the stringent threshold level. For the scenario of Cs-137 in soil, the smallest activity that can be detected with certainty is 0.15 μCi . As in the case with the source at surface, the denser grid spacing results in a higher detection certainty at lower activities.

The method described is useful for determining the certainty of detection for a buried source given the source activity, source position, detector spacing, and background counts. Although methods in this work only utilize the characteristic energy for analysis, the method is equally suitable using the full energy range. It is also desirable to obtain

the results in the opposite manner: to determine source location and activity from detector measurements. The next chapter presents this method.

Chapter 6

Localization of Source

The second part of this thesis investigates the process of finding a long-lived point source with unknown parameters. The problem assumes that several static measurements are taken from a detector at a constant height and at equally spaced steps with the goal of extracting source position and activity. The measurements are taken in a horizontal line above the medium in which the source is contained as shown in Figure 6.1.

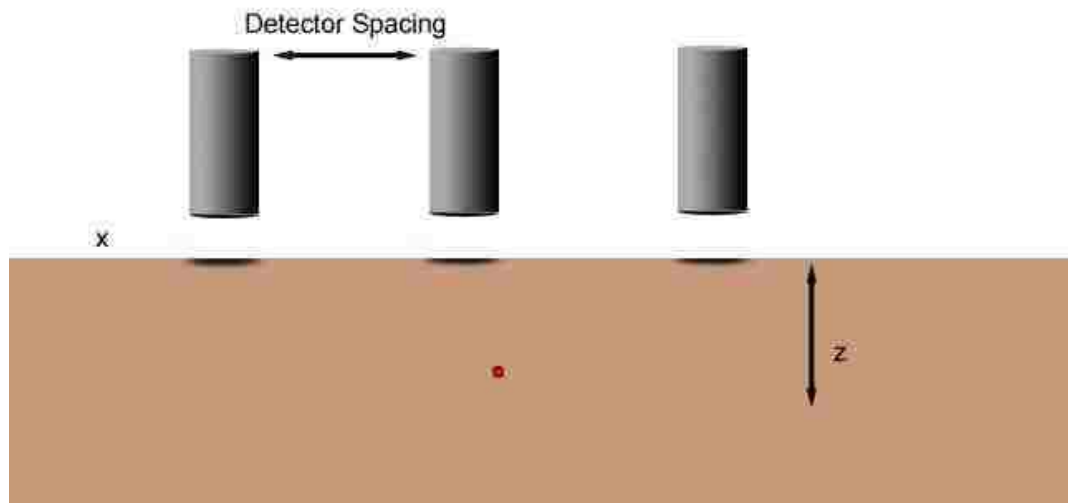


Figure 6.1 - Surveying configuration for localization method

The configuration may also be represented as an array of detectors at equal spacing taking measurements simultaneously. Using a minimum of three static measurements, the ratio of the detector counts is used to determine the unknown parameters of the source such as the depth, activity, and lateral position relative to the detectors. The method first involves creating a simulated map of detector efficiencies with respect to source locations. A best fit of the detector responses to the efficiency mapping is used to determine the source location, and subsequently the source activity.

Like part one of this thesis, the simulation is performed prior to calculations. However in this case, the source location is varied in the xz plane rather than the xy plane. For this part of the thesis, laboratory experiments are also performed and compared with simulations.

6.1 Simulated Efficiency Mapping

The MCNPX iteration process is first used to model the detector at a fixed height above the medium with the source varying in depth (z) and lateral position (x) to determine detection efficiency. The density of the transport medium is obtained and utilized in the simulation. The source is modeled in one centimeter increments from directly below the detector face to some maximum distance in the x - and z -direction, depending on the detection efficiency through the medium. The detection efficiency is thus determined for a source at a range of locations relative to the detector. This model assumes that the static measurements are taken along the x -axis with the front of the detector at $z = 0$. The response is assumed to be symmetrical to the detector position so only half the area is simulated.

The first simulation was modeled with the 3x3 NaI detector facing down and the center of the detector face located at $(x,z) = (0, 0)$ - all plotted coordinates are in cm - on the plot. Figure 6.2, presented in the xz plane, shows the resulting detected efficiency (γ detected / γ emitted) of a 662 keV (Cs-137) source in air. Figure 6.3 shows the same response over the full range and with the larger values masked to show the response at lower efficiencies.

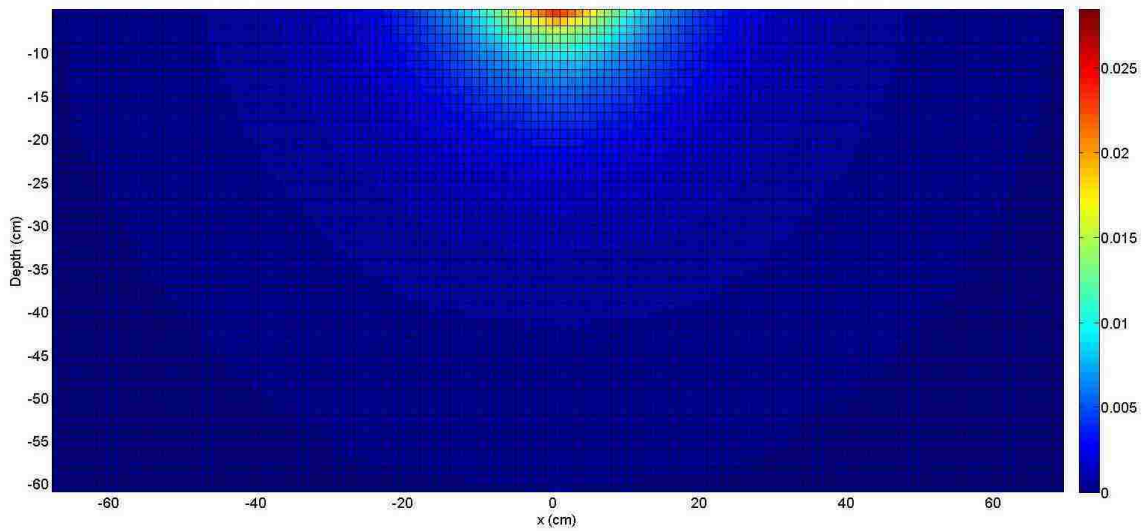


Figure 6.2 - 2-D simulated detector efficiency of Cs-137 in air

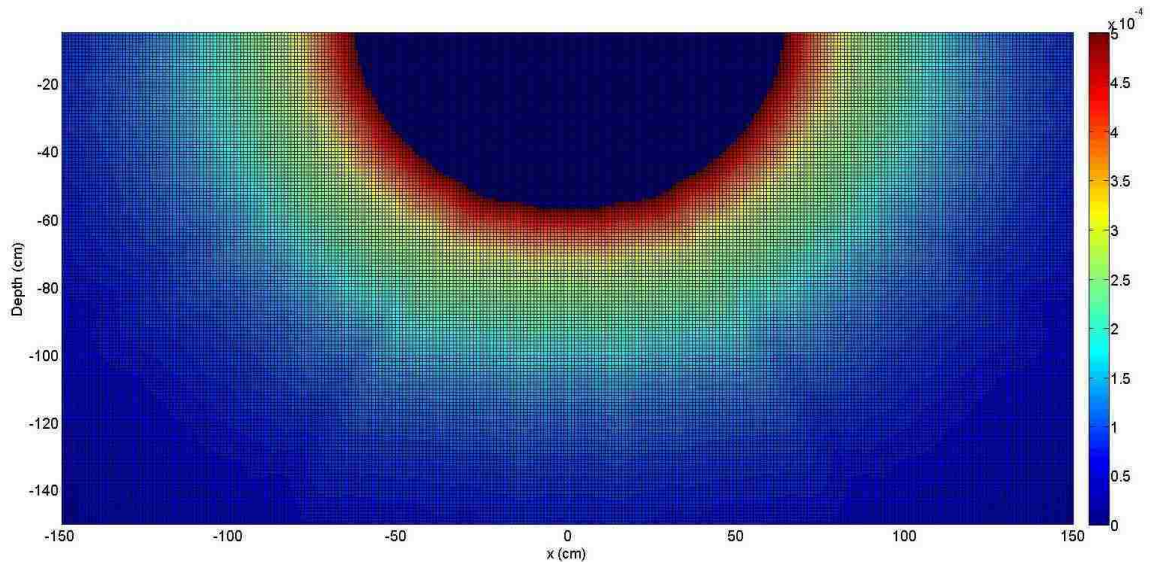


Figure 6.3 - 2-D simulated detector efficiency of Cs-137 in air with large values masked

To demonstrate the response in a medium, the Cs-137 source was also modeled in soil with the detector at position $(x,z) = (0,0)$ in air with the soil beginning at $z = -15.24$ cm (6 in). The response is shown in Figure 6.4 where the top of the plot represents the surface of the soil.

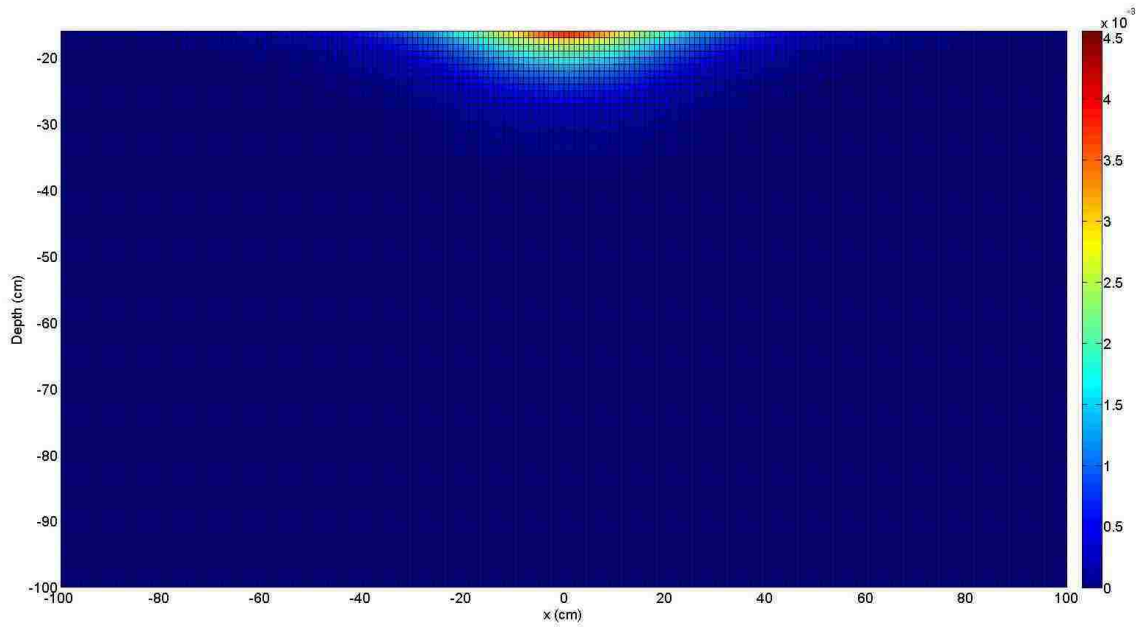


Figure 6.4 - 2-D map of simulated detector efficiency of Cs-137 in soil

The simulating time of the entire matrix of efficiencies varies depending on the media and the source energy. For this work, efficiency matrices in air were completed within one day. Soil matrices, however, took 2 to 3 days for completion. Longer simulation time is expected when simulating the full-range of energy because there is no cutoff of photons.

Assuming that a detector at a fixed height above the surface recorded counts at one centimeter spacing, Figure 6.5 is the resulting simulated efficiency of the source at each depth, a re-representation of the values presented in Figure 6.2.

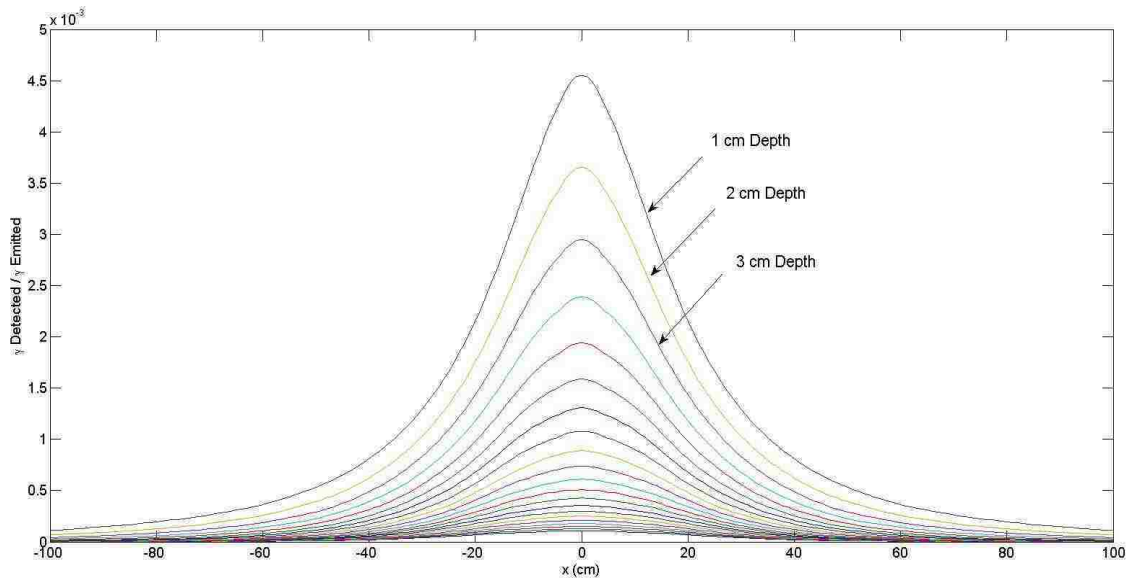


Figure 6.5 - Simulated detector efficiency of Cs-137 in soil at multiple depths

This plot demonstrates the unique pattern for varying source depth and vertical position of the detector. The curve corresponding with the closest z to the detector shows the highest efficiency and, importantly, the steepest slope. The same unique pattern will be evident from individual measurements taken at different lateral positions from a source. For example, Figure 6.6 shows the response of four measurements, spaced at 10 cm, for a source at the relative location $x = 23$. By comparing the pattern of the experimental data to the simulated efficiencies, the desired source information, i.e., source location and activity, can be extracted.

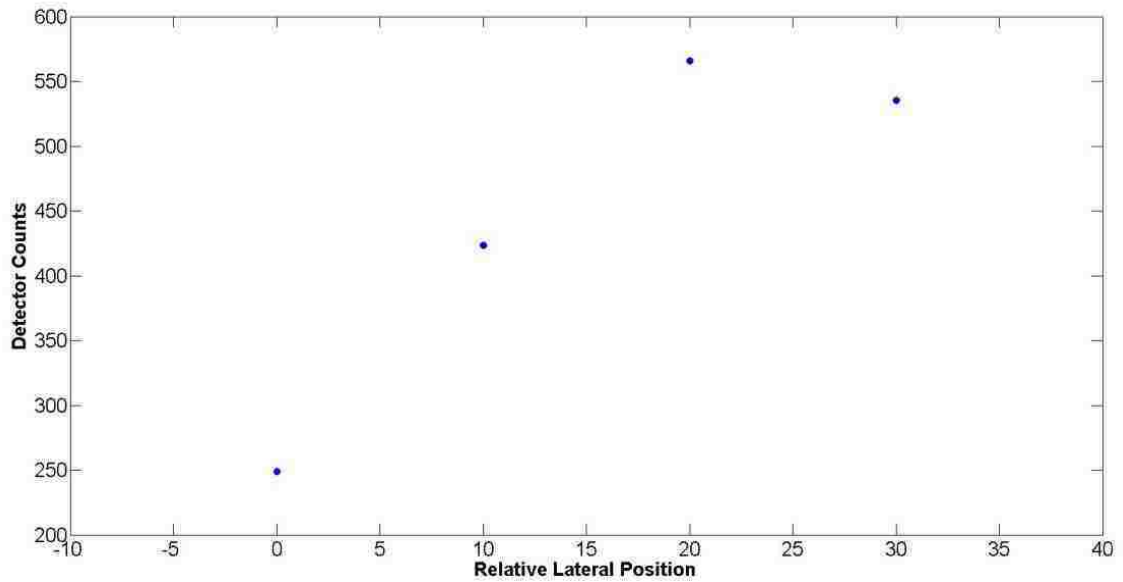


Figure 6.6 - Four detector measurements for a source at relative location $x = 23$

6.2 Fitting Measured Data to Simulated Data

Because the simulated data are normalized per photon, giving efficiency, it would be impossible to match a single measurement to any one curve without knowing the source strength. Three or more measurements, however, will quantify the measurements with a slope independent of the source strength.

Detector counts are obtained at a known constant spacing between detectors and compared to the expected (simulated) efficiency map using Matlab. The input parameters of the program are the unmodified counts obtained at each location per counting interval, and the spacing at which the counts were taken. The program compares the measured detector ratios to the efficiency mapping, starting at the minimum x and moving in 1 cm steps to the maximum x for each depth (z). Figure 6.7 and Figure 6.8 show examples of how the measured data are compared. The first plot shows the

discrete points being compared at the one centimeter depth curve. The second plot, representing a much better fit, shows the data being compared with the 2 cm depth curve. At each step the mean of the observed data is normalized to the mean of the relative expected points and Pearson's chi-square test is performed for each point in the series. As x and z are varied, the detector positions remain fixed. The unmodified chi-square test is defined as:

$$\chi^2 = \sum_{i=1}^N \frac{(O_i - E_i)^2}{E_i}$$

where O is the observed measurement and E is the expected point – the simulated efficiency. The test is used to measure the goodness-of-fit between the two point series where, in general, the smaller the chi-square value the better the fit [19].

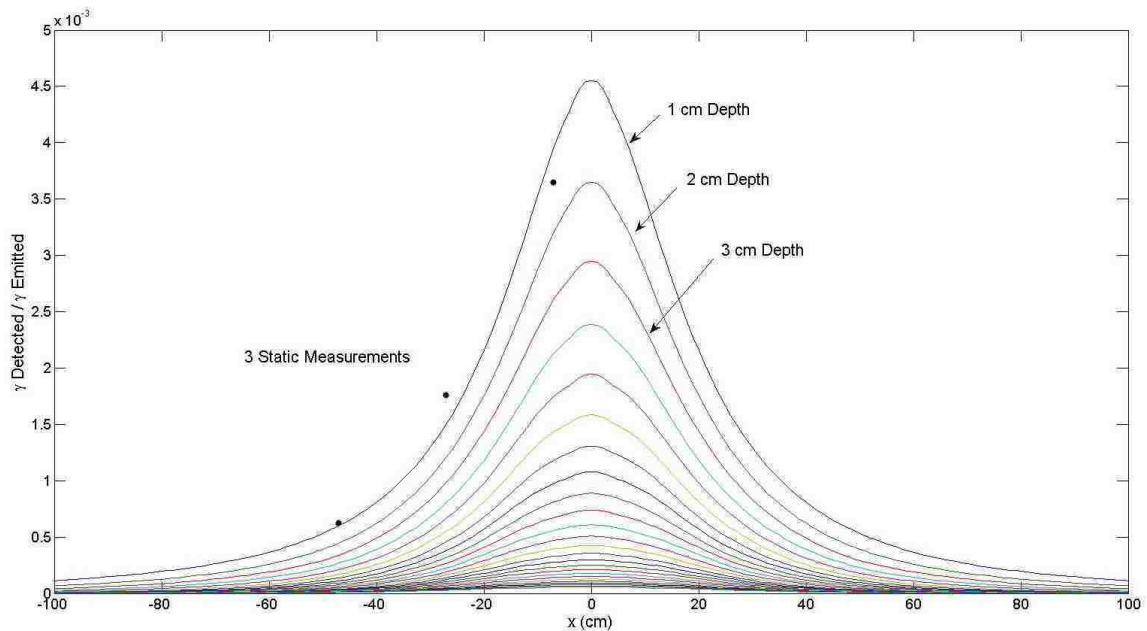


Figure 6.7 - Example comparison between measured data and the simulated data at 1 cm depth

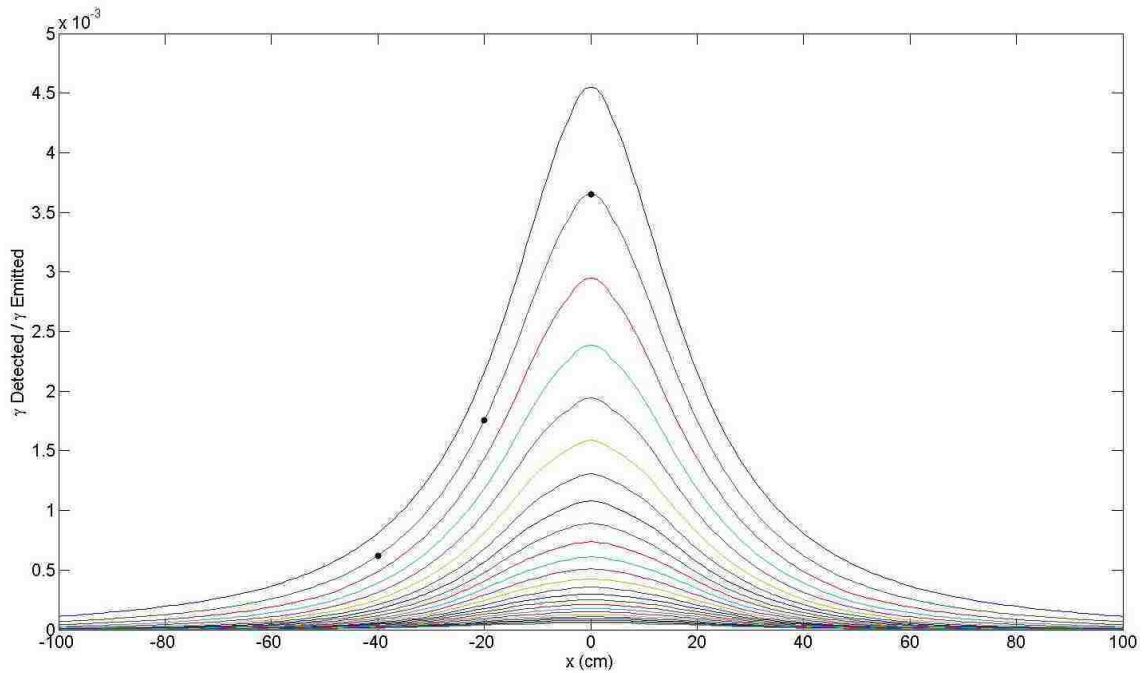


Figure 6.8 - Example comparison between measured data and the simulated data at 2 cm depth

The observed measured values are scaled:

$$\chi^2 = \sum_{i=1}^N \frac{(AO_i - E_i)^2}{E_i}$$

to give a minimum chi-square for that set of x and z; therefore chi-square values, minimized for each x and z, are compared globally. The comparison will ultimately result in one location where the chi-square value is the lowest – the location of the source with respect to the first detector measurement. The scaling factor A is also recorded at every location. This is the multiplication factor between the number of counts observed and the detector efficiency for the source at that point relative to the detector. Therefore,

once the location of the lowest chi-square is established for the entire grid, the reciprocal of the scaling factor at that location gives the approximate source strength in photons per counting interval. The position-by-position chi-square values are shown in Figure 6.9. The large chi-square values, implying a bad fit, are colored red and the lower values, a good fit, are blue. The location of the source is represented by the minimum chi-square value, located by the arrow.

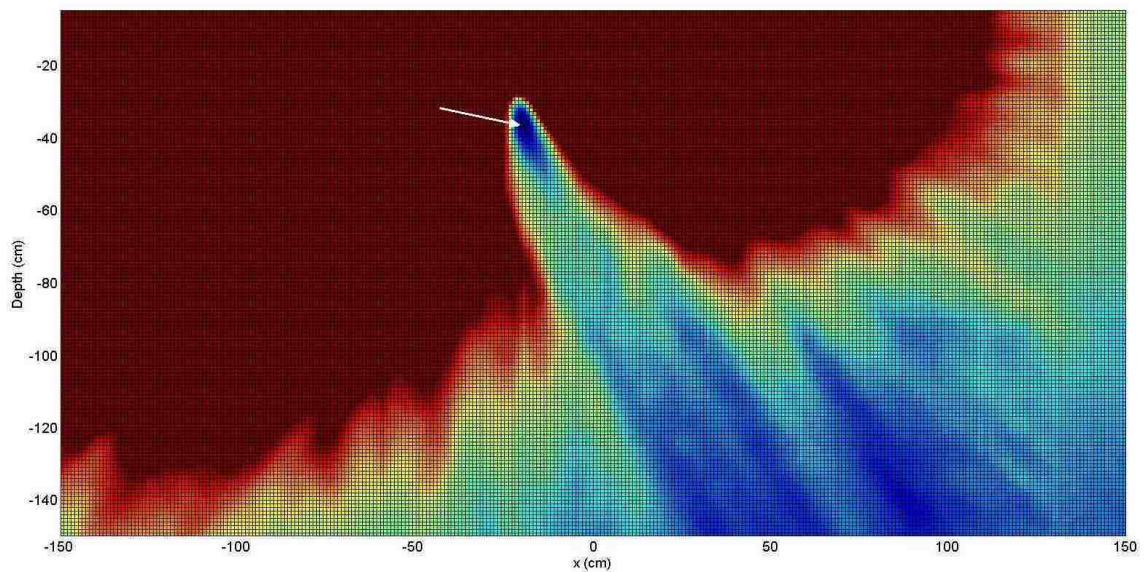


Figure 6.9 - Chi-square mapping showing source localization

Figure 6.10 demonstrates how quickly the chi-square values change at areas adjacent to the source location. Here, the global minimum is an order of magnitude smaller than the surrounding values at $1E-8$.

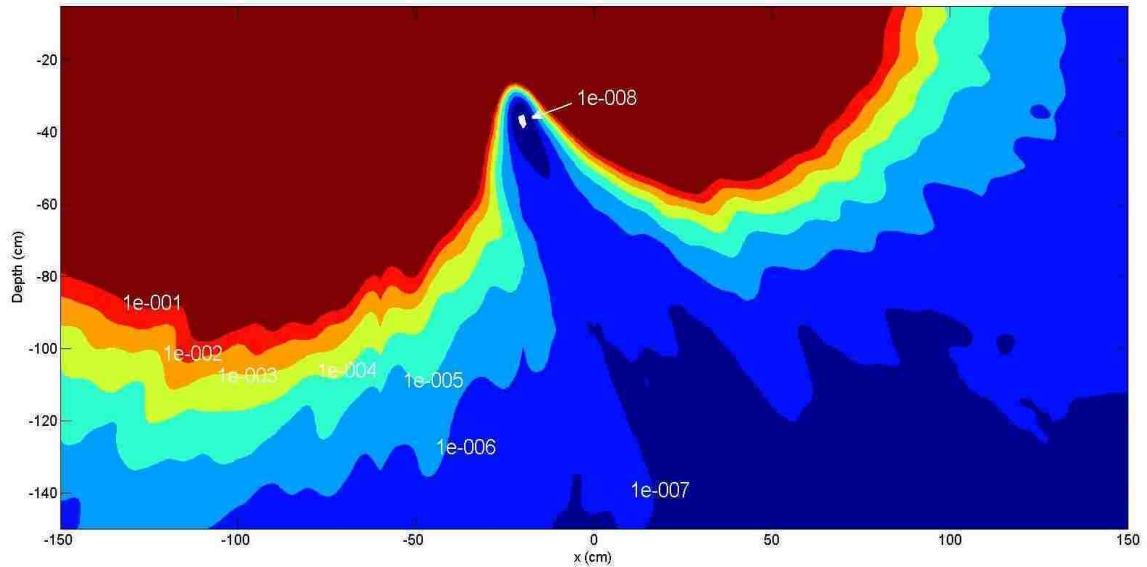


Figure 6.10 - Contours demonstrating change in chi-square values

Although the simulation time of the efficiency matrix was on the order of a few days, the actual comparison with the data and chi-square calculation takes less than a second for completion, making it ideal for field use.

6.3 Certainty from Counting Statistics

A method was established to relate the chi-square mapping to traditional tests for uncertainty as a function of position, such as confidence intervals. Using a known source strength, the expected number of counts, N , in each detector can be calculated from the MCNPX efficiency grid. Up to this point MCNPX values are used for both the efficiency mapping and the detector measurement, therefore in this example, the only variation is due the Monte-Carlo random sampling. The simulated grid values are limited to the range $N \pm k\sqrt{N}$ for a given detector reading. The result is a region of source positions

that will yield counts within a confidence interval defined by $k\sqrt{N}$. Figure 6.11 demonstrates a 7.5 μCi Cs-137 source simulated in air at a distance of 50 cm below the detector face with a confidence of \pm one standard deviation.

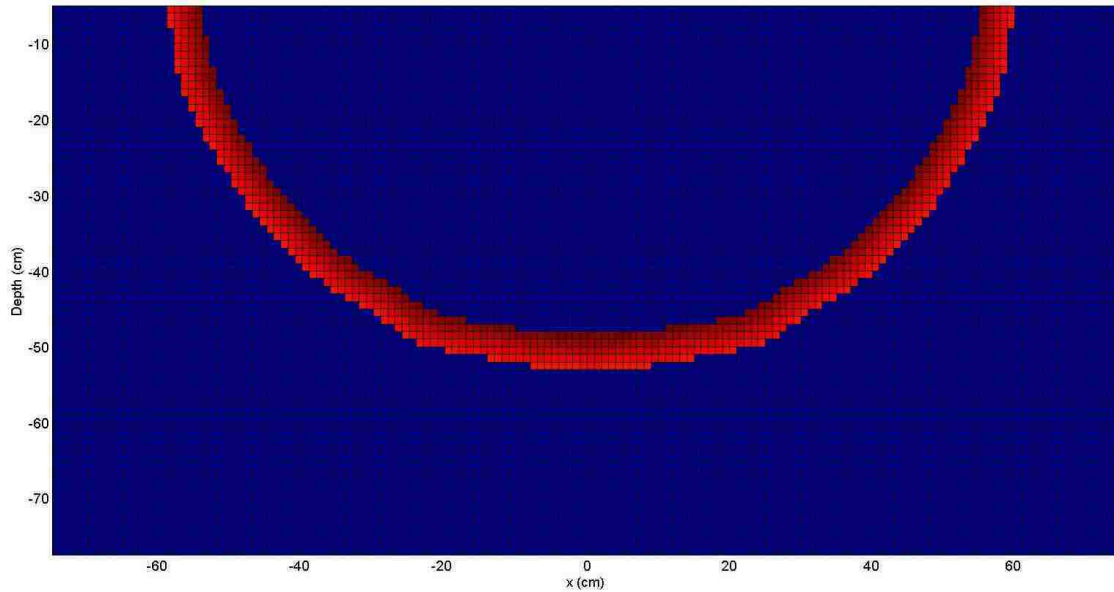


Figure 6.11 - ± 1 standard deviation confidence interval for simulated Cs-137 in air (1 reading)

The response represents all possible source locations that would yield a 68% confidence of falling within the band. By taking multiple static measurements at a fixed spacing, the location of the source is narrowed down significantly. Figure 6.12 shows the same source with two detector readings at -30 cm and -10 cm with respect to the source location at $x = 0$ and the same depth of 50 cm.

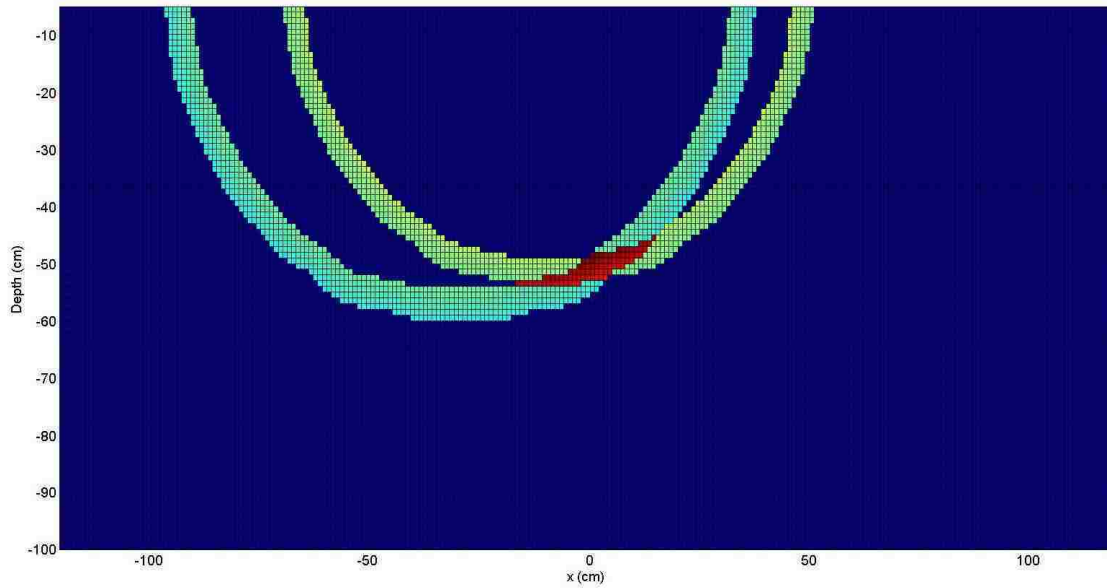


Figure 6.12 - ± 1 standard deviation confidence interval for Cs-137 simulated in air (2 readings)

For two detector readings at different positions, the confidence interval is narrowed to the overlap of the two responses, indicated in the figure by the red region. A third reading at the position $x = 10$ cm from the source is shown in Figure 6.13.

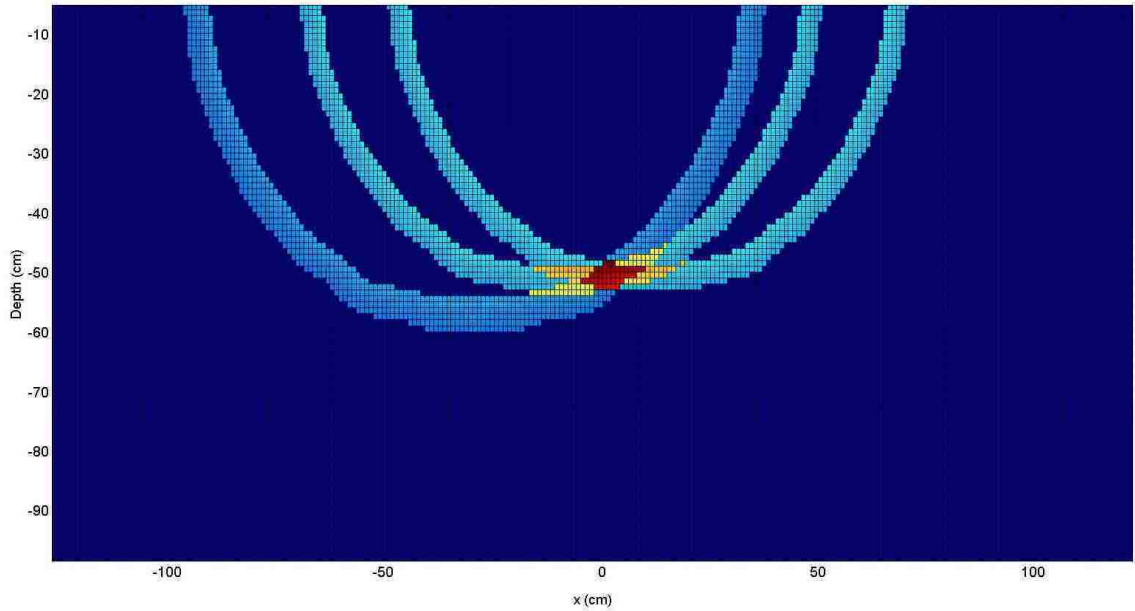


Figure 6.13 - ± 1 standard deviation confidence interval for Cs-137 simulated in air (3 readings)

To account for almost every possible location (99%) from each detector reading, the confidence bands are expanded to ± 3 standard deviations. The statistics are estimated by using steps of 1, 2, and 3 standard deviations. Figure 6.14 demonstrates the result where the center of each band (green) represents 68.2% probability, the second ring (light blue) represents another 27.2%, and the outer portion (medium blue) is another 4.2%. Everything outside these areas (dark blue) is assigned to zero. The values of each detector confidence ring are normalized to one, to account for a total probability that the source position, as determined by each detector can be anywhere within the ring.

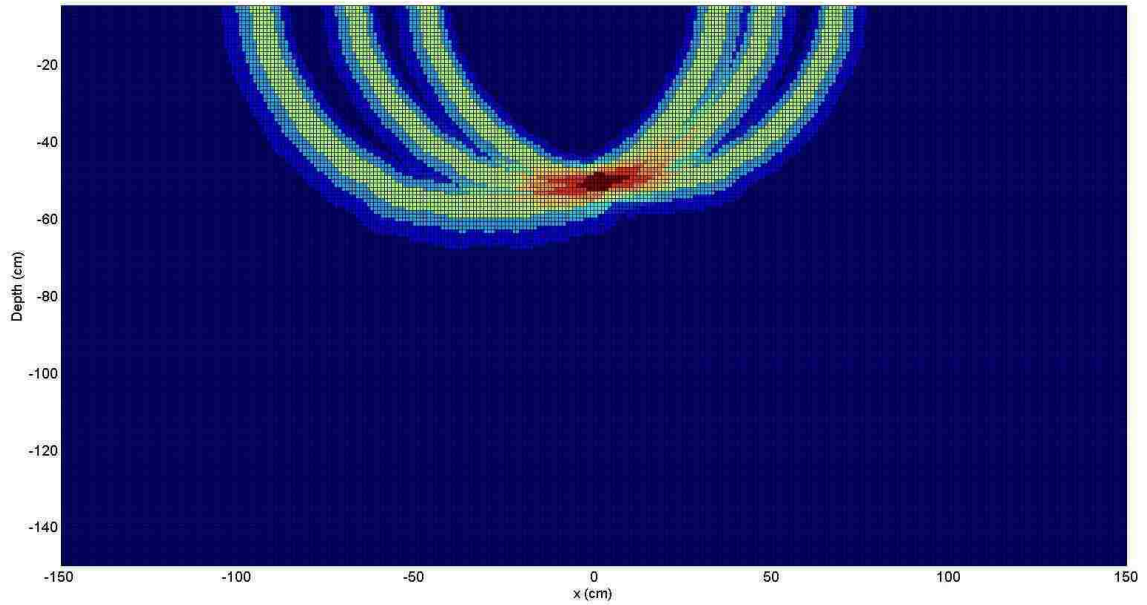


Figure 6.14 - ± 3 standard deviation confidence interval for Cs-137 simulated in air (3 readings)

The process is repeated for each detector confidence ring and the joint probability of every cell in the grid is taken. In the case of three detector measurements, the probability is:

$$P = P(\text{Interval 1}) \cap P(\text{Interval 2}) \cap P(\text{Interval 3})$$

The only nonzero results are the cells where all the confidence intervals overlap as shown in Figure 6.15.

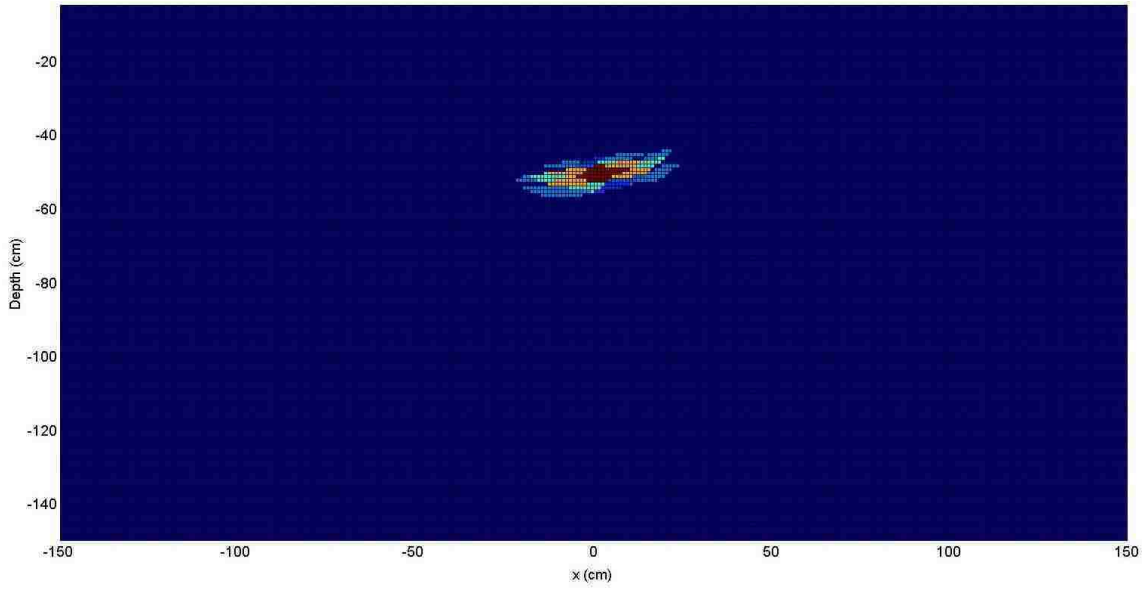


Figure 6.15 - Overlap of confidence intervals

Because it is assumed that the detector measurement will always fall within the 99% confidence interval for each detector individually, the intersection region is giving the total probability. Cells of equal values are broken up into contour regions. The contour plot overlaid on the joint region plot above is shown in Figure 6.16. The grid cell colors are changed to show the contour lines. Each contour region represents the joint probability for several detectors. In this particular example, the center contour represents the probability region where 48% of the measurements are expected to fall; 82% of the measurements are expected to fall inside the yellow contour; and 98% are expected to fall inside the light blue contour. For all grid-plots, the values are assigned to the grid line intersection points rather than the center of the grid pixel. As a result contours are placed according to the intersection and may not encompass the full block. This is an artifact of the different graphics outputs of the analysis program.

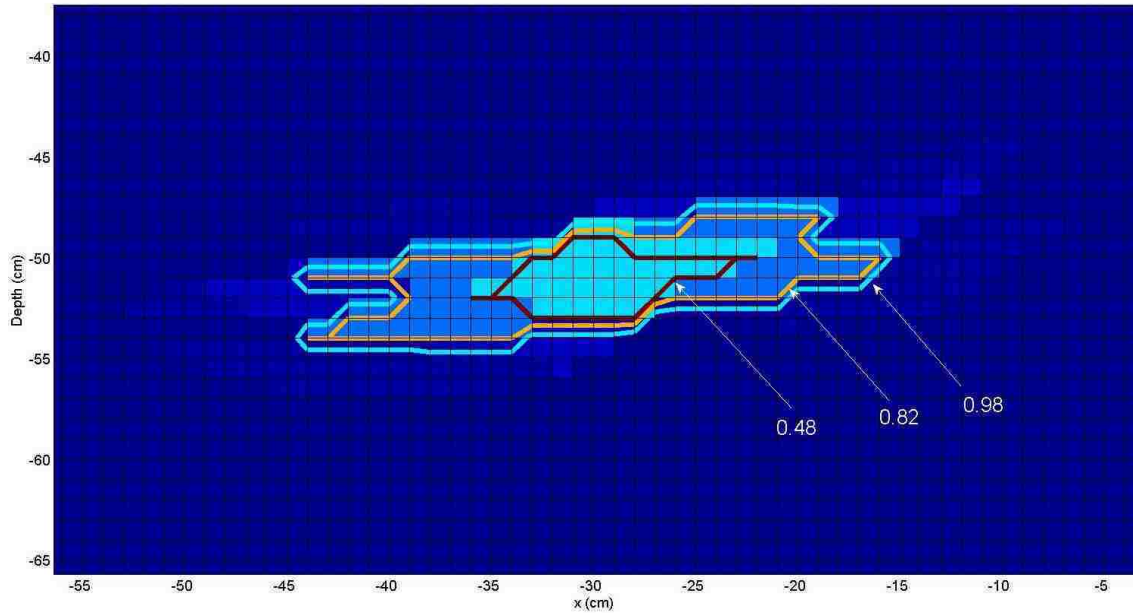


Figure 6.16 - Contour plot showing spatial probabilities for multiple simulated detector readings

6.4 Simulation Results

The chi-squared localization method was first verified using MCNP to model the detector measurements and then tested with experimental measurements. By using simulated data as the detector measurements, the only variability introduced is the Monte Carlo random sampling difference between the efficiency mapping and the subsequent simulated detector response runs. The method was verified in two different scenarios. In both scenarios, 10,000,000 histories - source photons emitted isotropically - were used to get a very close approximation to the mean.

6.4.1 Simulation Experiment 1

The first simulation used four measurements in air with the detector at positions $x = -20, 0, 20,$ and 40 cm with respect to the source, and with a depth of -37 cm perpendicular to the face of the detector measurements. The source was assumed to have an activity of $232,325$ Bq and simulations were run for a total of $10,000,000$ 662 keV photons emitted. The resulting MCNP detector measurements in counts per second at each location were $222.1, 265.5, 223.5,$ and 143.9 . Using the chi-square best fit method described previously, the extracted source location was at $x = -20$ cm and a depth of -37 cm. The chi-square plot is demonstrated in Figure 6.17.

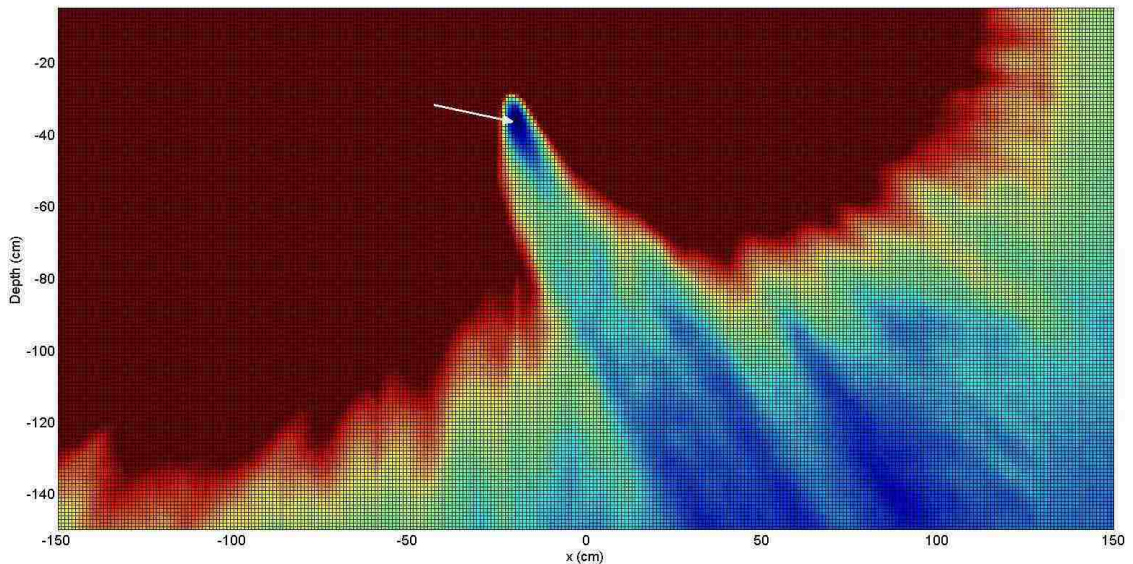


Figure 6.17 - Simulated chi-square results of Cs-137 in air using four measurements

The dark red region represents the chi-square values that exceed $3E-5$ and the blue regions are lower values. The single minimum chi-square value of $3.2E-8$ is located at the position $x = -20$ and a depth of -37 , again shown by the arrow. Although it has no

statistical representation, the chi-square plot is important because it demonstrates the pattern in the fit between the actual and the expected measurements.

Recalling that the experimental detector values were scaled by some factor to match the amplitude of the expected, the resulting values for each detector are 231,179, 232,813, 232,679, and 231,826. These factors are representative of the source activity in Becquerels (Bq). Each independent factor was used to construct the confidence interval for each detector position shown in Figure 6.18.

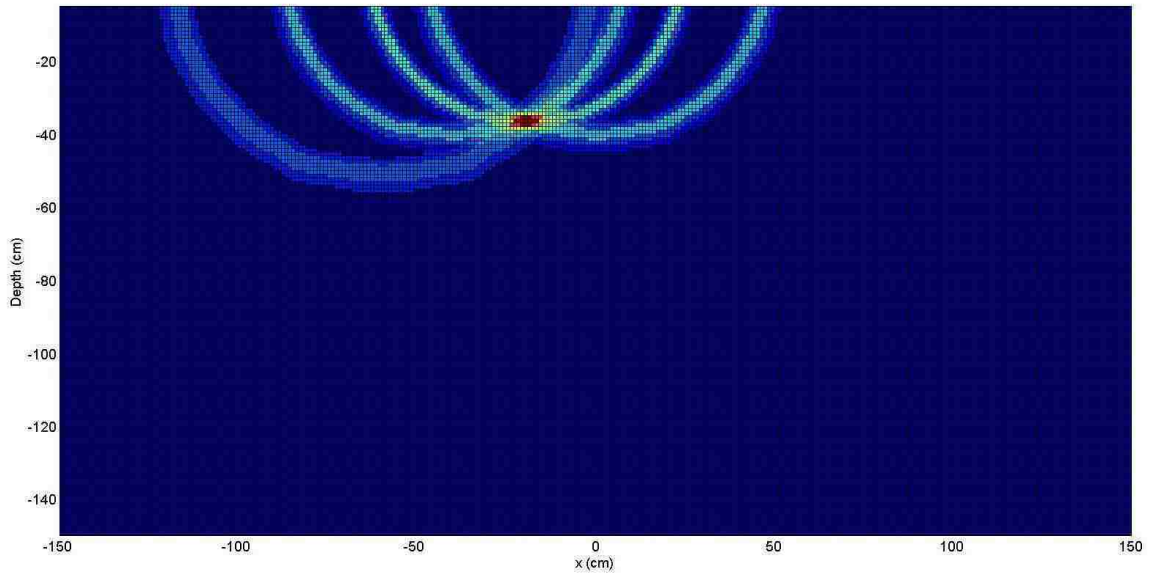


Figure 6.18 - Simulated contours for Cs-137 in air using four measurements

The calculated source activity, an average of the four extracted values, resulted in 232,186 Bq where the actual source activity was 232,325 Bq, a 0.06% error. Finally, the confidence contours overlaid on the chi-square mapping is presented in Figure 6.19.

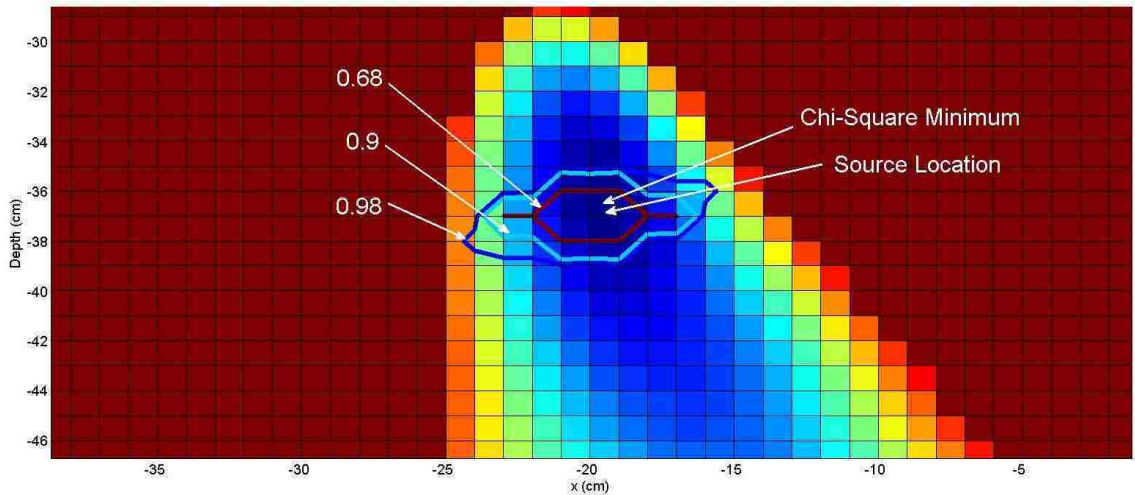


Figure 6.19 - Contour plot of Cs-137 in air using four simulated measurements. Chi-square minimum at $(x,z) = (-20, -37)$ and source location at $(x,z) = (-20, -37)$. All (x,z) coordinates in this and subsequent plots are in units of cm

As expected, the simulated results yield very accurate results with the chi-square minimum and the actual source location at the same location. Using a large number of simulated histories, the deviation between the simulated measurements and the simulated expected values are close enough to yield a very good fit.

6.4.2 Simulation Experiment 2

The second simulated experiment consisted of a 0.511 MeV (Sodium-22) source behind approximately 14 cm of soil and a total distance of 30 cm from the face of the detector. Three measurements were taken with the detector at locations $x = -20, 0,$ and 20 cm with respect to the source. The simulated source activity was 142,805 Bq with 10,000,000 histories taken. The corresponding MCNPX measurements were 42.4, 76.3, and 44 averaged per second. The chi-square plot is shown in Figure 6.20. Again, the minimum chi-square value is represented by the dark blue region shown by the area.

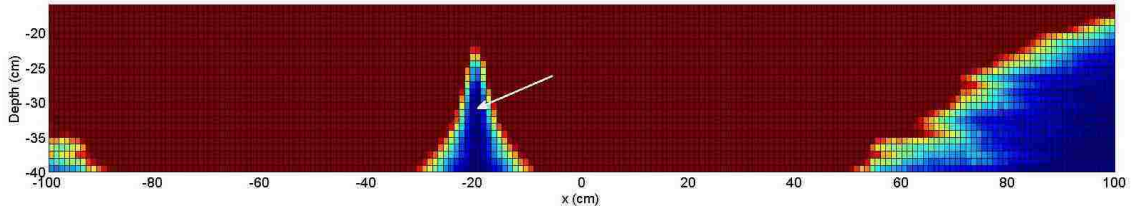


Figure 6.20 - Simulated experiment of Na-22 in soil using three measurements

Although difficult to represent in the chi-square plot, the minimum value is again smaller than the adjacent values by several orders of magnitude. The contours of chi-square values are shown in Figure 6.21. One grid pixel, located by the arrow, has the minimum value of $4e-8$.

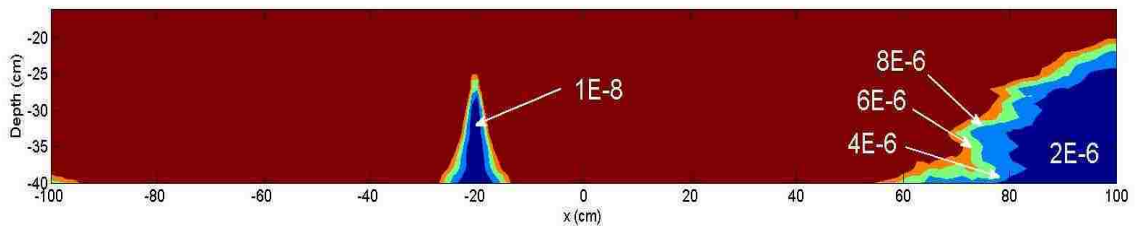


Figure 6.21 - Chi-square contours of simulated experiment for Na-22 in soil

At the location of the best chi-square fit, the reciprocals of the scaling factors resulted in the values 140,617, 143,135, and 145,582. The resulting confidence intervals using the reciprocals of the scaling factors are presented in Figure 6.22.

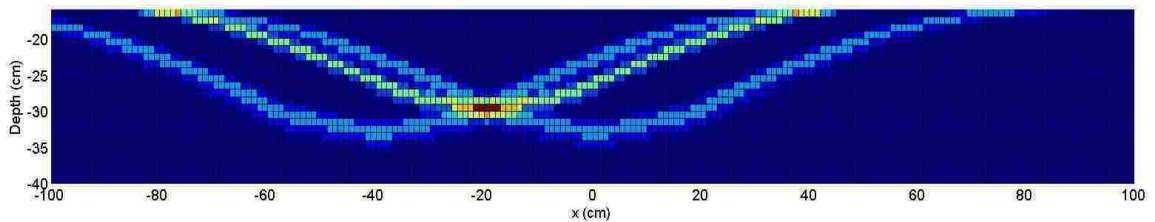


Figure 6.22 - Simulated contours for Na-22 in soil using three measurements

The resulting calculated source activity was 143,153 Bq, only a 0.2% error of the assumed source activity. Again, the chi-square minimum and the actual source location are at the same location as shown in Figure 6.23.

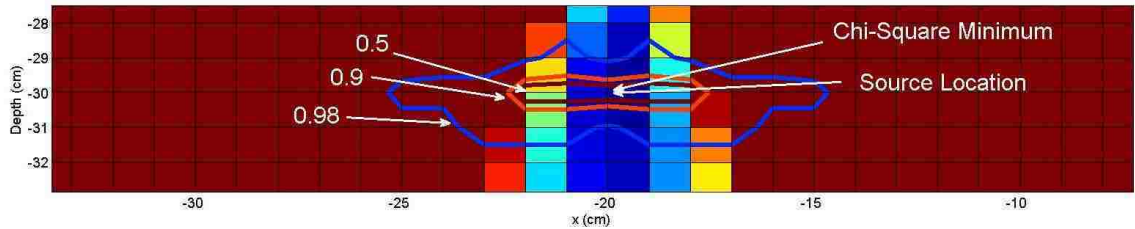


Figure 6.23 - Contour plot of Na-22 (0.511 MeV) in soil using three simulated measurements. Chi-square minimum at $(x,z) = (-20, -30)$ and source location at $(x,z) = (-20, -30)$

The simulated experiments demonstrate that the chi-square fit method yields good results for both the location of the source and the extracted activity of the source.

6.5 Detector Experiments

The method was also tested experimentally under several different laboratory conditions using an optics table for accurate positioning and measurements. The Ortec Model 905-4 3 inch diameter by 3 inch height cylindrical NaI detector was used for all experiments to validate the localization method. The detector was coupled to a multi-channel analyzer to obtain detailed energy spectra for peak analysis. The detector was mounted on an optics table, shown in Figure 6.24 to provide precise positioning and measurements.



Figure 6.24 - Experimental setup for 3x3 NaI detector and source

For experiments that were analogous to a source in soil, a tank filled with sand was utilized as shown in Figure 6.25. The attenuation coefficients of SiO_2 (sand) and MCNPX soil were verified to be similar over the relevant energies, and the measured density of the laboratory sand was used for all simulated calculations.



Figure 6.25 - Experimental setup with sand

6.6 Experimental Results

The results of all experiments are summarized below.

6.6.1 Experiment 1

The first experiment consisted of three detector measurements of Cs-137 in air. The measurements were taken with the detector at positions $x = -30, -5,$ and 20 cm, and a height of 50.5 cm with respect to the source. Unlike the simulated experiments, more

error is introduced from the uncertainty of the true source activity, positional error, and counting statistics. The location of the best fit is presented in Figure 6.26.

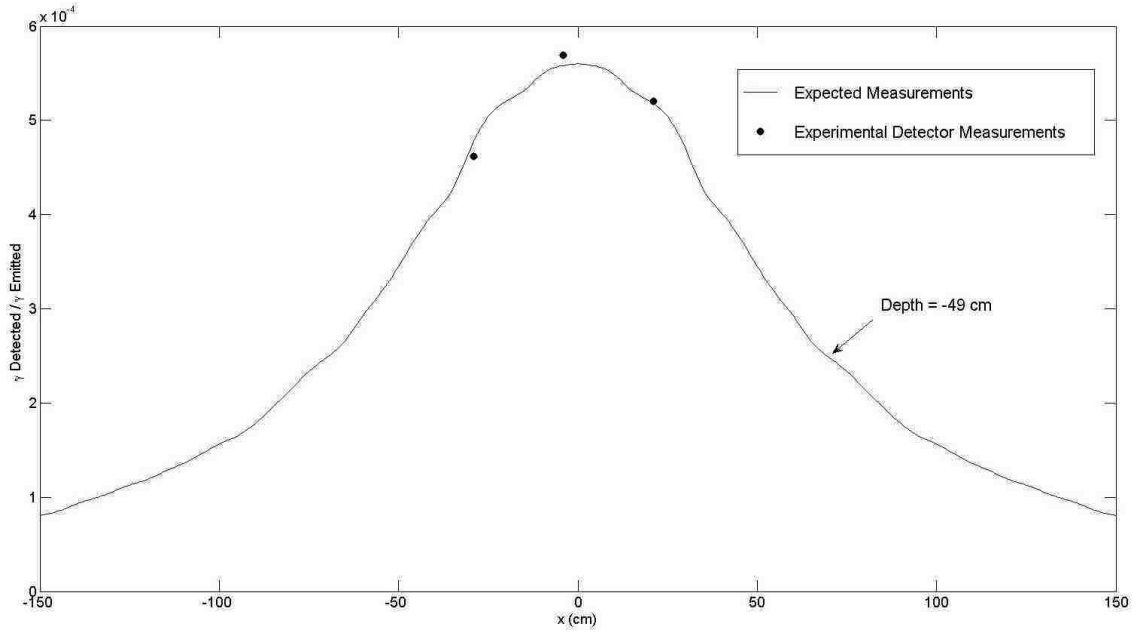


Figure 6.26 - Fit between experimental and expected measurements for Cs-137 in air

Figure 6.27 shows the resulting chi-square plot. As in the case of the simulated experiment, the dark red region represents the chi-square values that exceed $1E-5$ and the blue regions are lower values. The single minimum chi-square value of $6.83E-9$ is located at the position $x = -29$ and a depth of -49 , shown by the arrow.

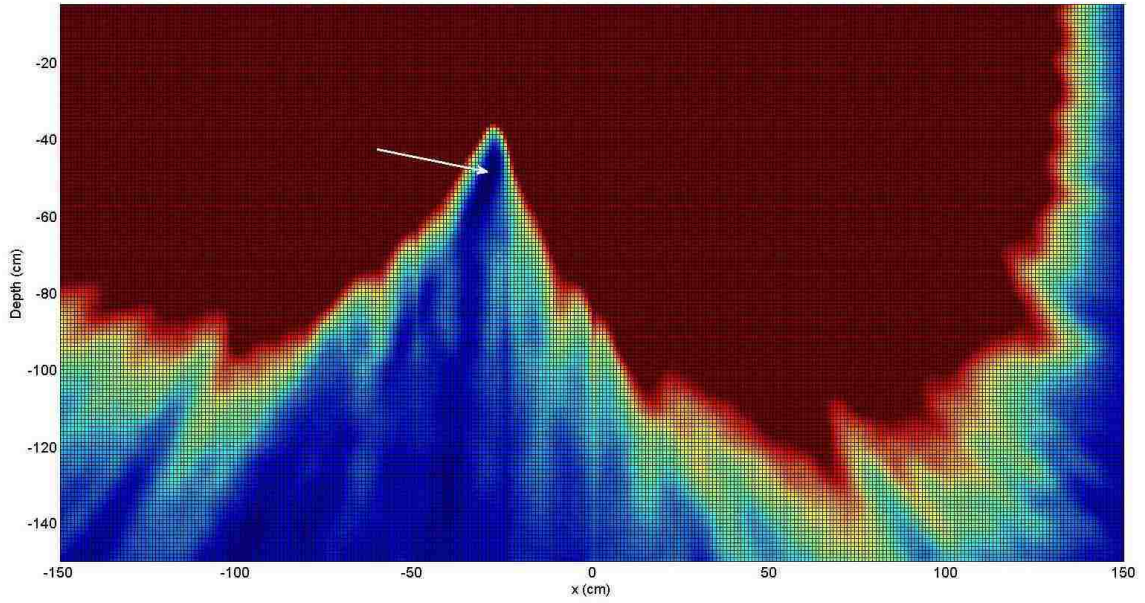


Figure 6.27 - Experimental chi-square results of Cs-137 in air using three measurements

The area of best fit is distinguished by a peak with very high chi-square values above and on each side of the peak. The right portion of the plot represents an area where there were an insufficient number of points to compare due to the edge of the grid. Showing chi-square values less than $7E-7$ greatly localizes the area of interest as demonstrated in Figure 6.28.

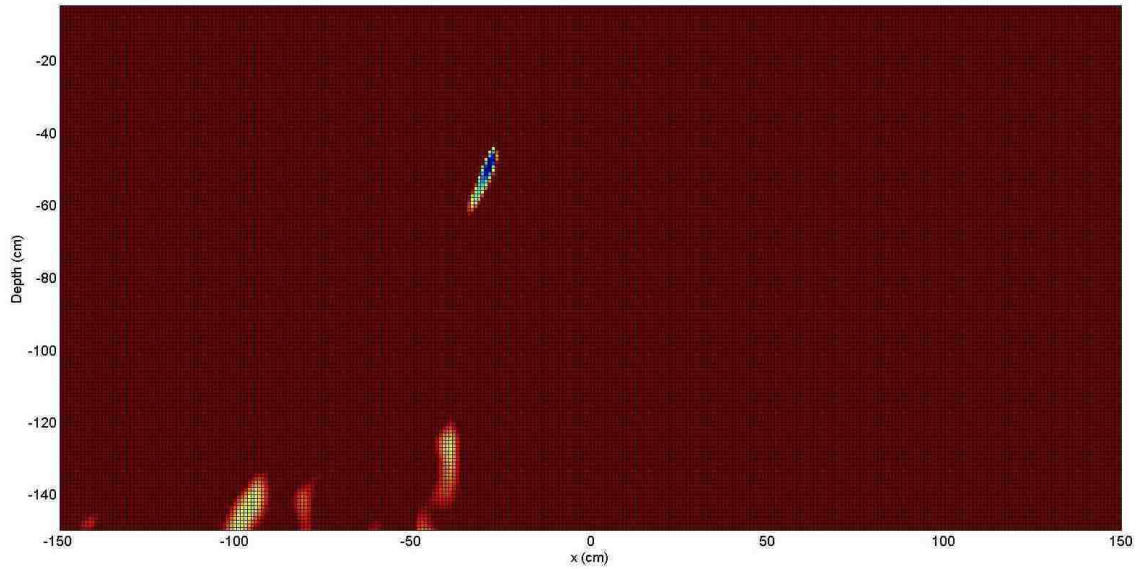


Figure 6.28 - Experimental chi-square results of Cs-137 in air using three measurements

Again the lowest chi-square values, and best fits, are represented by the dark blue regions. The remaining regions are a result of comparing the values at a depth where statistical variations are high. This uncertainty for the applied Cs-137 is demonstrated in Figure 6.29, where the contours represent the standard error for a ten-second counting time. The chi-square values in these low statistics regions are still distinguishable from the true source region because they are larger by several orders of magnitude.

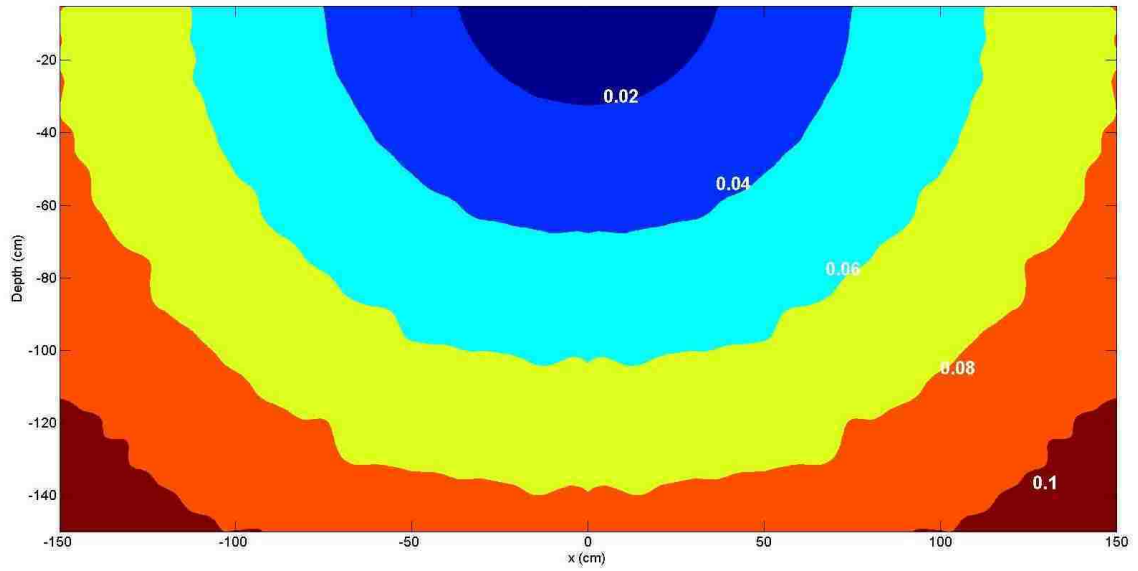


Figure 6.29 - Relative uncertainty of simulated detector efficiency in air using a 187,353 Bq Cs-137 source with a ten second counting time

The resulting factor of each measurement was 186,053, 185,374, and 185,096. The detector contours are presented in Figure 6.30 where again the overlap is represented by the red region.

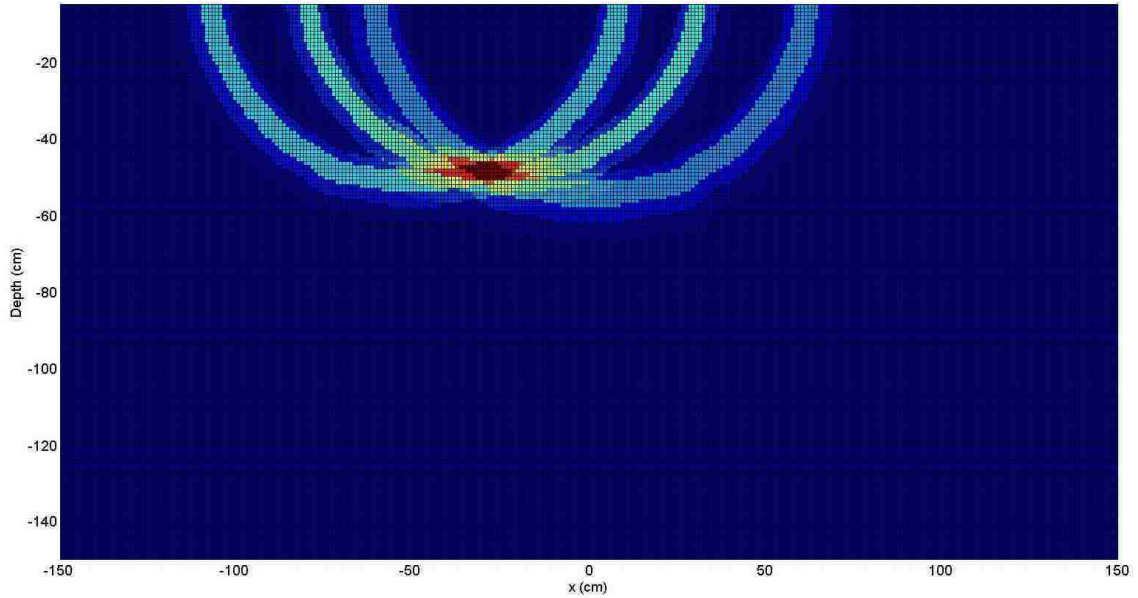


Figure 6.30 - Experimental contours for Cs-137 in air using three measurements

The resulting contour plot overlaid on the chi-square plot is demonstrated in Figure 6.31.

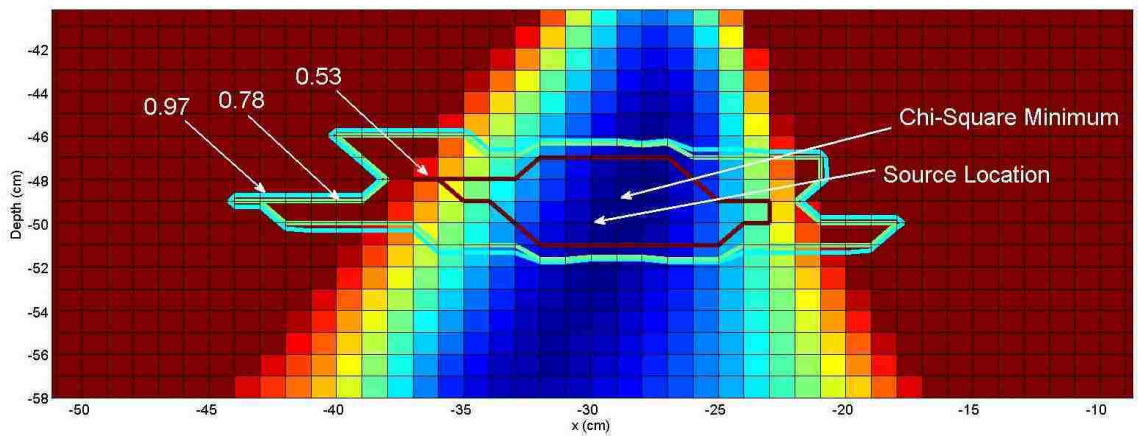


Figure 6.31 - Contour plot of Cs-137 in air using three measurements. Chi-square minimum at $(x,z) = (-29, -49)$ and source location at $(x,z) = (-30, -50.5)$

In this case, both the actual source location and the predicted source location (chi-square minimum) are within the most constrained 52% interval. The extracted location was

accurate to within 2 cm of the actual location, and the extracted source activity resulted in a relative error of only 1% to the actual source activity.

6.6.2 Experiment 2

The experiment was repeated using a higher activity Cesium-137 source with four measurements. The measurements were taken with the detector at $x=-20, 0, 20,$ and 40 cm with respect to the source and a height of 36.5 cm above the source. The source activity for this experiment was $234,809$ Bq. The chi-square plot is shown in Figure 6.32.

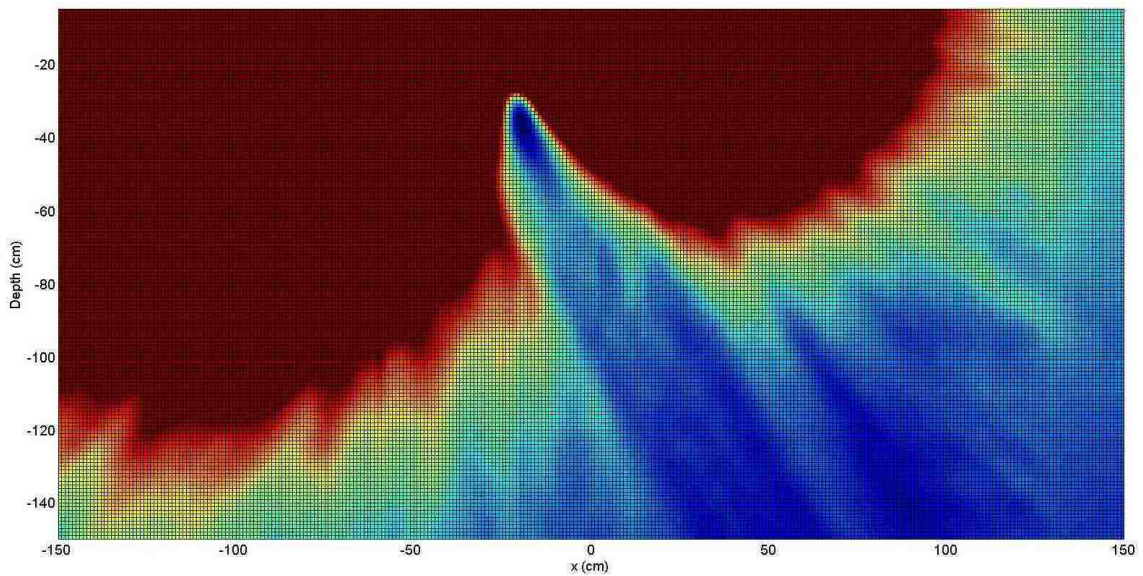


Figure 6.32 - Experimental chi-square results of Cs-137 in air using four measurements

By taking four measurements with the source closer to the detectors, the dark blue region within the peak is much more defined in Figure 6.32 as compared with Figure 6.27. In this case, the resulting reciprocal of the scaling factors of the experimental data were $234,552, 237,428, 230,992,$ and $236,302,$ with the same 1:1 relation between the inverse

of the scaling factor and source activity in Bq. The corresponding confidence intervals are shown in Figure 6.33. As a result of the higher source activity, closer proximity to the detector, and greater number of measurements, the width of the one sigma curve is smaller and so the overlap region is greatly reduced.

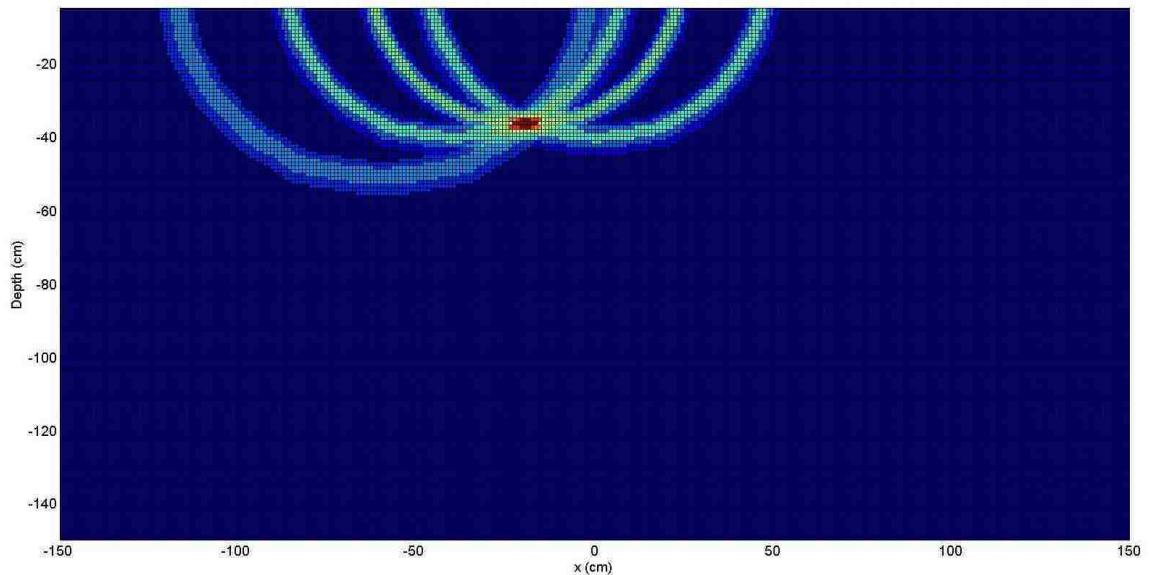


Figure 6.33 - Experimental contours for Cs-137 in air using four measurements

Figure 6.34 shows the resulting confidence contour overlaid on the chi-square plot. Again, both the chi-square minimum and the experimental source location are within the smallest defined (68%) contour interval.

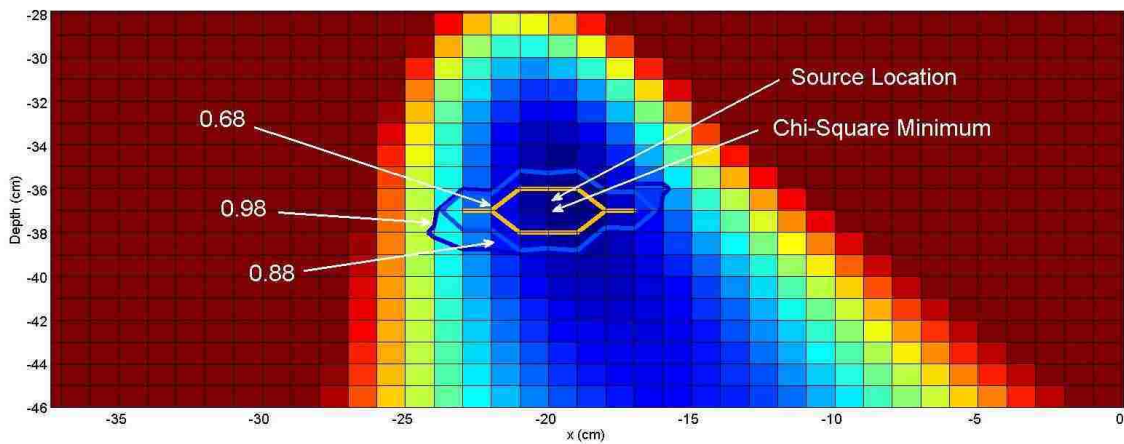


Figure 6.34 - Contour plot of Cs-137 in air using four measurements. Chi-square minimum at $(x,z) = (-20, -37)$ and source location at $(x,z) = (-20, -36.5)$

In this case the extracted source location was within one cm of the actual location and the extracted source activity had a small relative error of 1.1% of the actual activity.

6.6.3 Experiment 3

The experiment was also performed using a Sodium-22 source to determine the response at different energies in air. Three measurements were taken with the detector at the locations $x = -30, -10,$ and 10 cm with respect to the source at a depth of -33 . The chi-square plot for the 0.511 MeV peak is shown in Figure 6.35.

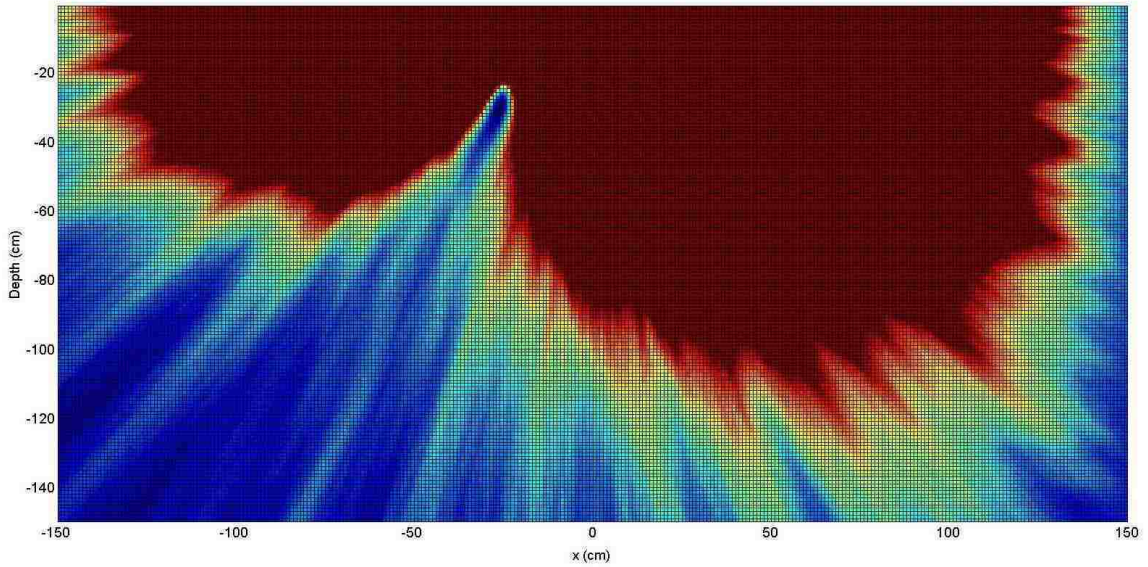


Figure 6.35 - Experimental chi-square results of Na-22 (0.511 MeV) in air

The corresponding reciprocals of the scaling factors for the three detector measurements were 148,127, 148,877, and 148,609. The confidence intervals for the experimental detector measurements are shown in Figure 6.36.

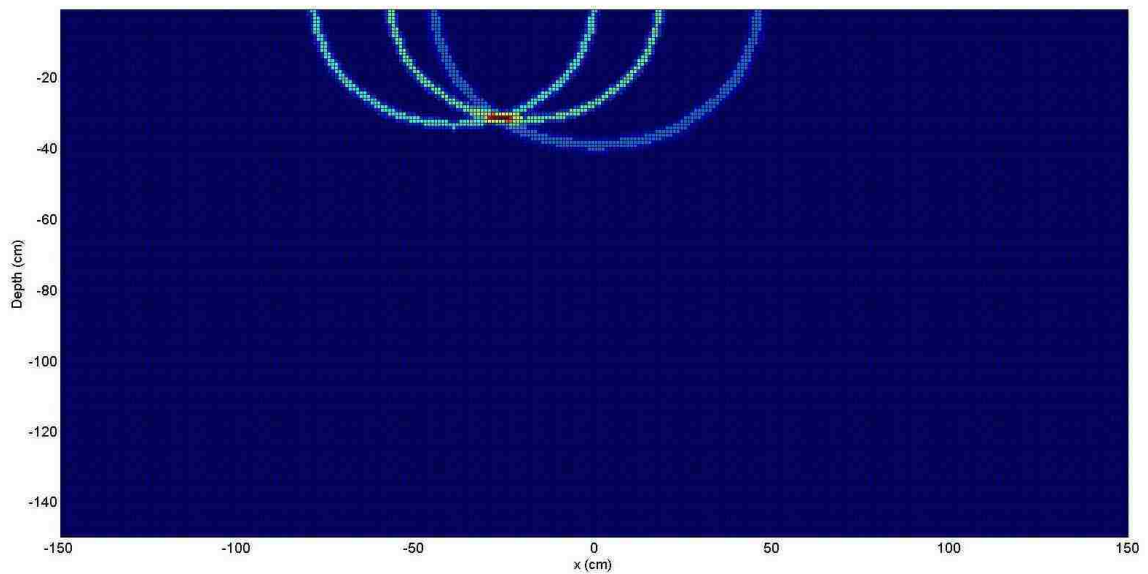


Figure 6.36 - Experimental contours for Na-22 (0.511 MeV) in air using three measurements

As a result of the shallow depth and the higher number of 0.511 MeV photons per decay (due to annihilation), the confidence intervals are very narrow resulting in a small region of certainty. The chi-square minimum and the experimental source location both fall within the region of 98% confidence interval as shown in Figure 6.37. It should be noted that values of the grid plots are assigned at the intersections of the lines, not the entire grid. As a result, the inner contours in this case are smaller than the height of a grid block, however they do encompass the values assigned by the line.

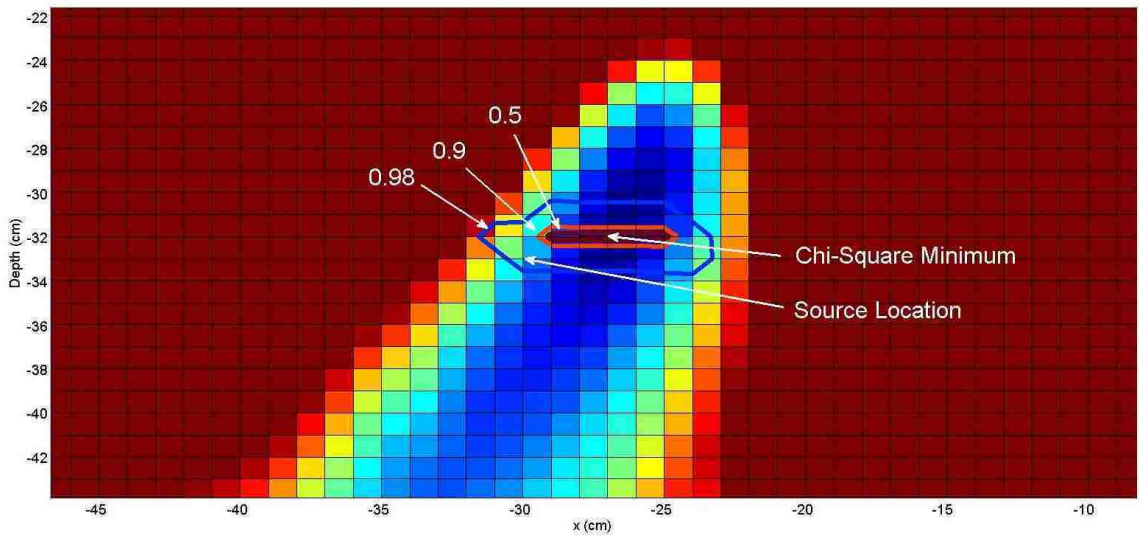


Figure 6.37 - Contour plot of Na-22 (0.511 MeV) in air using three measurements. Chi-square minimum at $(x,z) = (-27, -32)$ and source location at $(x,z) = (-30, -33)$

In the case of the 511 keV peak, the extracted positional accuracy is within 4 cm of the actual source location, and the source activity had a 4% relative error to the actual activity.

6.6.4 Experiment 4

Using the same locations, the 1.274 MeV peak of the Na-22 source was evaluated to determine the response at a higher energy. The chi-square plot is shown in Figure 6.38.

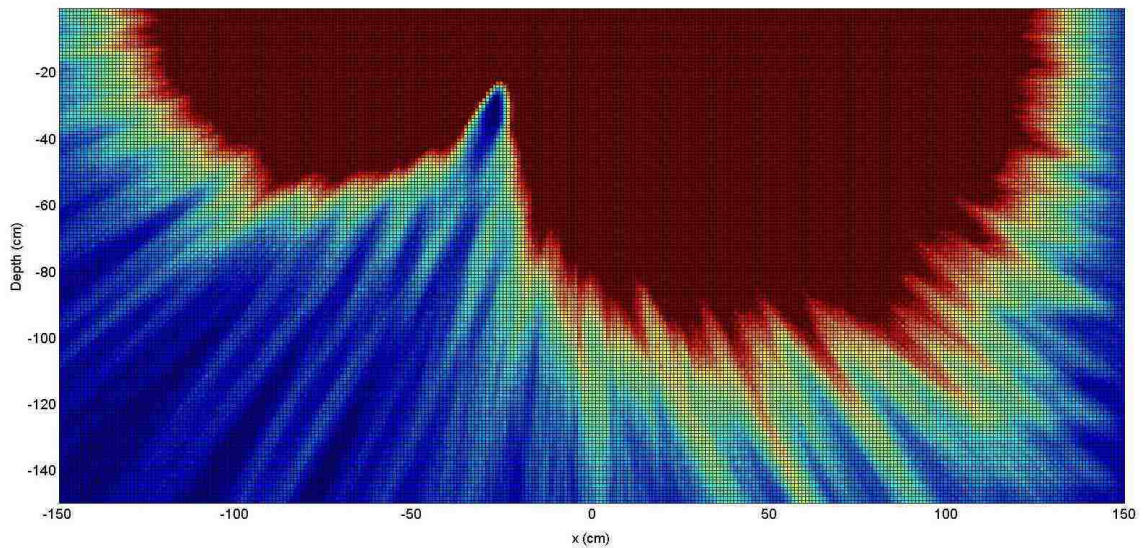


Figure 6.38 - Experimental chi-square results of Na-22 1.274 MeV peak in air

The reciprocals of the scaling factors were 124,054, 124,110, and 123,542. The resulting confidence intervals are shown in Figure 6.39. As expected, the intervals are much wider than the 0.511 peak due to the single photon emission per decay with the same number of decays.

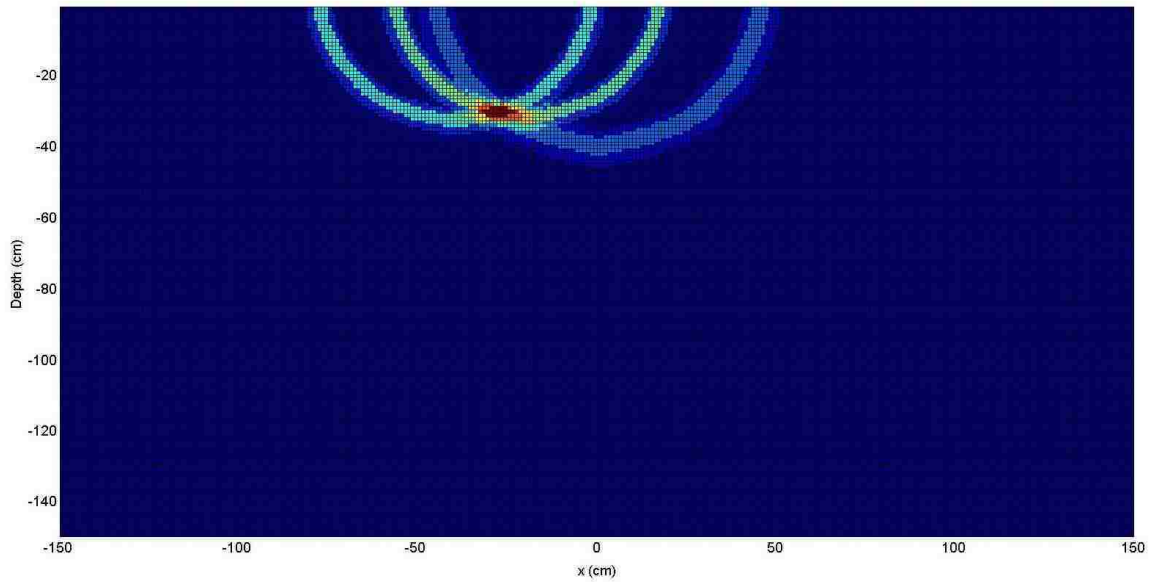


Figure 6.39 - Experimental contours for Na-22 (1.274 MeV) in air using three measurements

The resulting confidence interval overlapping the chi-square plot is shown in Figure 6.40. In this case the actual source location falls outside the 79% region of confidence but is within the 98% region of confidence for the detector measurements.

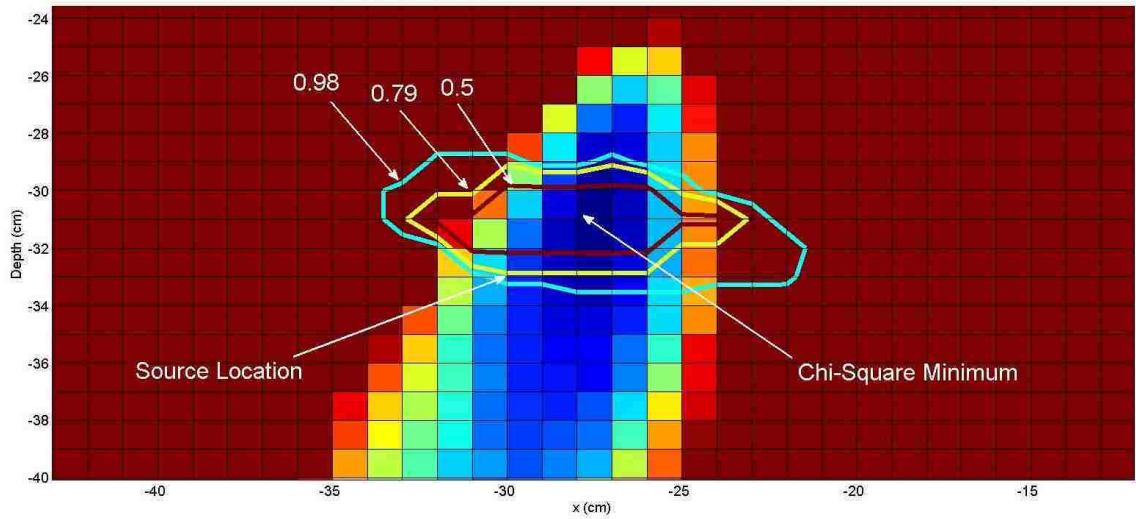


Figure 6.40 - Contour plot of Na-22 (1.274 MeV) in air using three measurements. Chi-square minimum at $(x,z) = (-28, -31)$ and source location at $(x,z) = (-30, -33)$

Due to the lower efficiency of the 3x3 NaI detector for the 1.274 MeV line, there is greater uncertainty in both the initial efficiency mapping and the subsequent measurements of the chi-square mapping. The extracted 1.274 MeV peak location was within 3 cm of the actual source location and had an extracted activity error of 13% relative to the actual activity. The relative source errors for every experiment, with the exception of the 1.274 MeV, are within the 5% source calibration error. The results from all experiments performed in air are summarized in Table 6.1.

Table 6.1 - Actual versus extracted results in air

Energy (MeV)	Actual			Extracted			Relative Source Error
	x (cm)	Depth (cm)	Source (Bq)	x (cm)	Depth (cm)	Source (Bq)	
0.662	-30	50.5	187,353	-29	49	185,483	0.1%
0.662	-20	36.5	232,325	-20	37	234,809	1%
0.511	-30	33	142,805	-27	32	148,585	4%
1.274	-30	33	142,805	-28	31	123,891	13%

6.6.5 Experiment 5

To test the primary motivation of this method, i.e., the ability to locate concealed or buried sources, the experiment was performed using a Na-22 source in soil. In this experiment the detector face was 15.24 cm (6 in) away from the media surface. Simulated data from more than 40 cm depth were omitted due to a large relative error. Each measurement was counted for 1200 seconds to obtain good statistics through the media. The chi-square plot is shown in Figure 6.41. The depth only accounts for a maximum of 25 cm into the soil, 40 cm including the air, because simulated efficiencies below this depth exceeded the maximum f8 tally relative error of 0.1%.

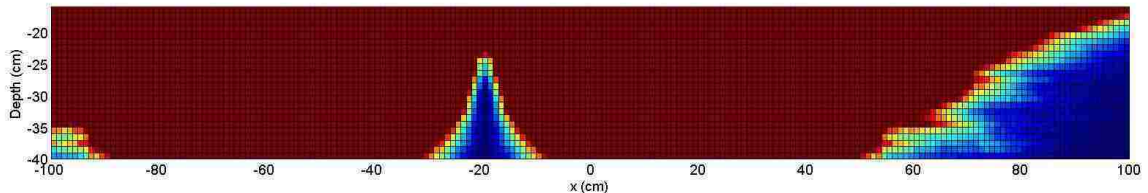


Figure 6.41 - Experimental chi-square results of Na-22 0.511 MeV peak in soil

The reciprocals of the scaling factors were 150,522, 151,203 and 151,329. The resulting confidence intervals for each detector are shown in Figure 6.42.

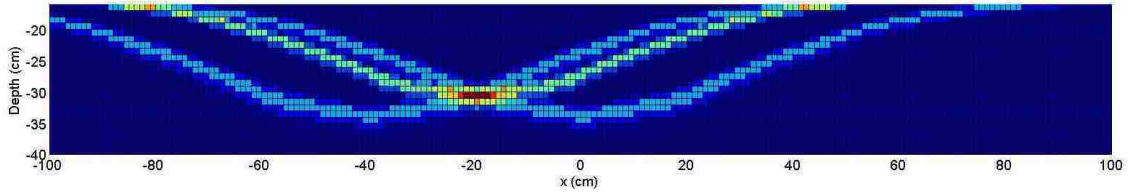


Figure 6.42 - Experimental confidence rings of Na-22 (0.511) in soil

In this case the intervals take a different shape than the source in air because of the attenuation of the soil. The overlap region is very narrow in height due to the large change in attenuation with varying depth. The contours are shown in Figure 6.43.

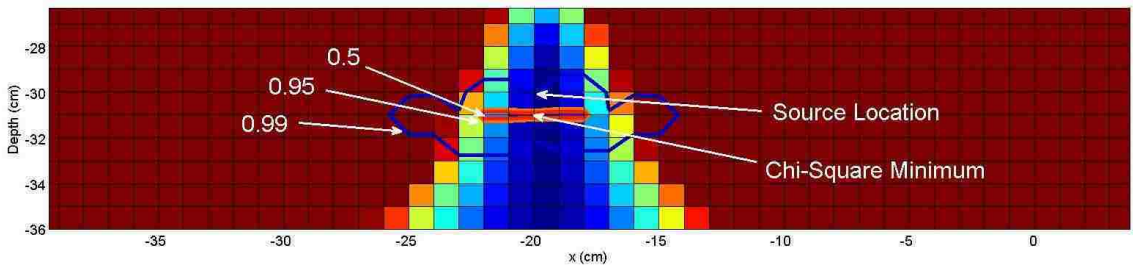


Figure 6.43 - Contour plot of Na-22 (0.511 MeV) in soil using three measurements. Chi-square minimum at $(x,z) = (-20, -31)$ and source location at $(x,z) = (-20, -29.84)$

For Na-22 in soil, the location of the source falls outside the contour representing 95% confidence but remains inside the 99% confidence. The calculated location of the 511 keV peaks was only one cm from the actual source location, and the calculated source activity had a 5.8% relative error to the actual.

6.6.6 Experiment 6

Using the same source positions as Experiment 5, the 1.274 MeV peaks from Na-22 were also obtained and analyzed. The chi-square plot is shown in Figure 6.44. In this case the depth extends to 35 cm into the soil, 50 cm source to detector distance when including the 15 cm of air, because the 1.274 MeV photons are more penetrating in the soil than the 0.511 MeV photons.

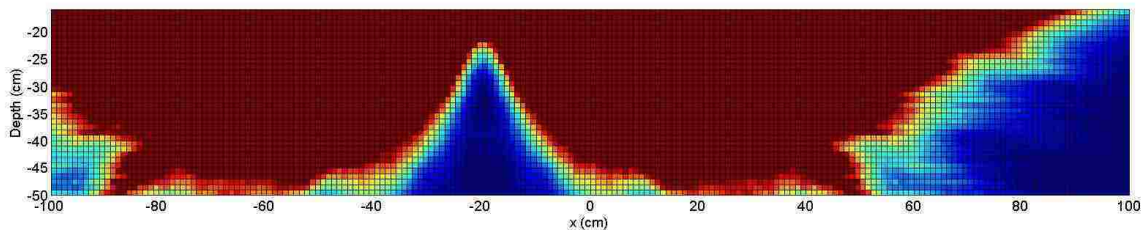


Figure 6.44 - Experimental chi-square results of Na-22 1.274 MeV peak in soil

Compared with the 0.511 MeV line, the lower number of photons per decay for the 1.274 MeV line as well as the lower efficiency of the detector at this energy results in lower counts with higher error. The chi-square plot is much broader in the peak and contains sufficiently more ‘noise’ on the edges. Again, the noise in the edge region is attributable to the high relative error in these regions. This is demonstrated by Figure 6.45, which shows the relative error contours of the detector response for a 142,805 Na-22 Bq source in soil. Due to the longer photon path length through soil from these areas, the results are less reliable.

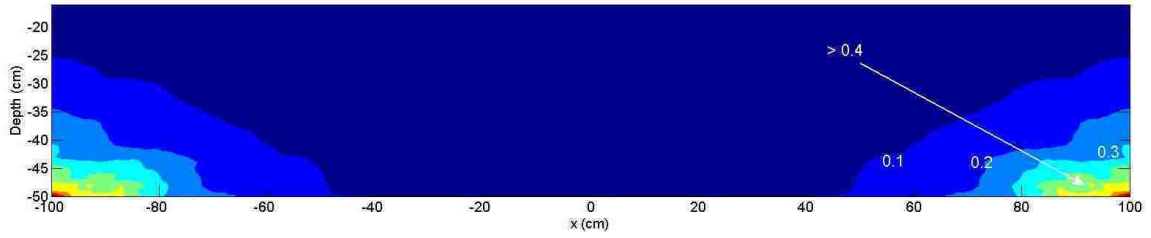


Figure 6.45 - Relative error contours of 142,805 Bq Na-22 (1.274 MeV) in soil using 120 second counts

From the chi-square mapping, the resulting reciprocals of the scaling factors were 185,171, 184,680, and 190,157. The experimental confidence intervals using these factors are shown in Figure 6.46. The lower counts and fewer photons per decay for the 1.274 MeV measurements result in a much larger region of overlap.

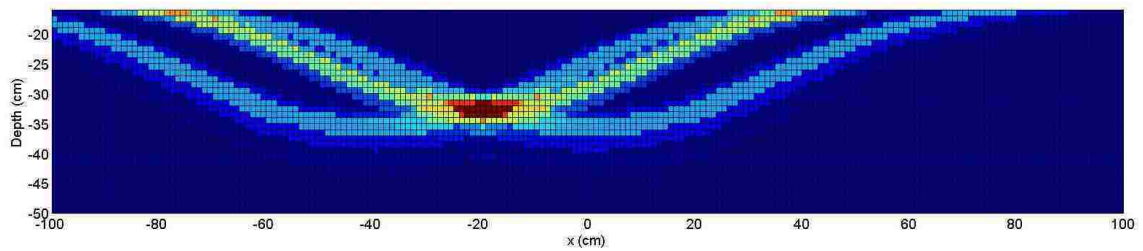


Figure 6.46 - Experimental confidence rings of Na-22 (1.274 MeV) in soil

Finally, the resulting confidence intervals overlaid on the chi-square map are shown in Figure 6.47. In this case, the actual location of the source is outside the 99% confidence ring of the calculated location. This is due to the relatively high value of the calculated source activity.

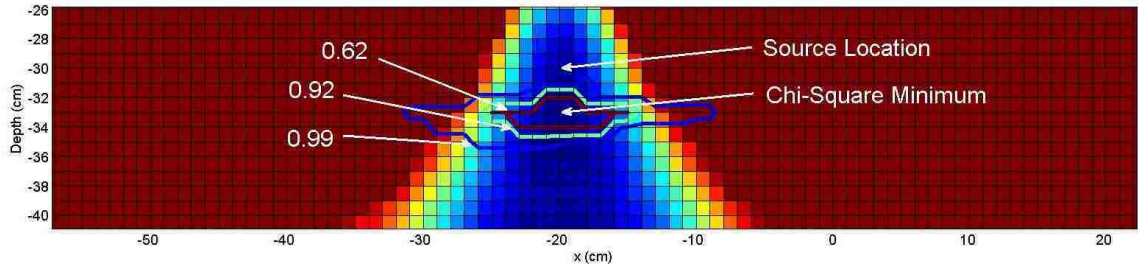


Figure 6.47 - Contour plot of Na-22 (1.274 MeV) in soil using three measurements. Chi-square minimum at $(x,z) = (-20, -33)$ and source location at $(x,z) = (-20, -29.84)$

The 1.274 MeV peak was less accurate than the 0.511 MeV peak with the calculated location within 3 cm of the actual location and a calculated relative source error of 31%. As demonstrated, these extracted quantities are related. Assuming the source is farther away requires a more intense source for the similar detector readings. Both the air and soil experiment for the Na-22 (1.274 MeV) resulted in a large error. This was a result of a number of different sources of error including detection efficiency at that energy, lower resolution of the peak, and the presence of a sum peak (1.274 + 0.511 MeV) that was not incorporated in the counts. The results of both soil experiments are summarized in Table 6.2.

Table 6.2 - Actual versus extracted results in soil

Energy (MeV)	Actual			Calculated			Relative Source Error
	x (cm)	Depth (cm)	Source (Bq)	x (cm)	Depth (cm)	Source (Bq)	
0.511	-20	30	142,805	-20	31	151,050	6%
1.274	-20	30	142,805	-20	33	186,362	31%

Chapter 7

Discussion and Summary of Results

The method described in Chapter 5 uses the full energy peak of a source to determine the certainty of detection from multiple equally spaced measurements. Although the work in this section uses only Cesium-137 for analysis, the methodology is suitable for any source, medium, and detector. According to the results, the minimum detectable activity of the source using a 3x3 NaI detector was 30 nCi through air and 150 nCi in 7.62 cm (3 in) of soil. For smaller detector spacing lengths, the certainty of detection was greater.

The method in Chapter 6 approached the problem from the opposite side, by calculating the lateral position, depth, and activity of the source using three or more detector measurements. Using three measurements for a Cs-137 source in air resulted in a radial positional difference of only 2 cm and a source activity of 1% of the actual position and activity. Using four measurements yielded even better localization results with a positional difference of 1 cm and a 1.1% relative source activity error. For Na-22 in air with three detector measurements, error for the 0.511 MeV peak was 4 cm radial and 4% relative source error. The 1.274 MeV positional difference was 3 cm, however the activity had a higher relative error of 13%. For the experiment using three

measurements for a Na-22 source through 14 cm of soil, the 0.511 MeV peak resulted in a positional difference of 1 cm and a relative source error of 5.8%. Using the 1.274 MeV peak resulted in a positional error of 3 cm and had the largest relative source error of 31%. Of all 6 experiments, only the 1.274 MeV peak through soil resulted in the actual source location falling outside the total confidence contour. The error is most contributable to the lower counting statistics as a result of the low efficiency of the 3x3 NaI detector at higher energies and thus lowering counting statistics. Note that even a 3 cm position difference is less than half the size of a single detector used for this experiment.

For the work in this thesis, the expected values were simulated with relatively high density grids at one cm spacing between measurements. For both methods, the motivation of the high density grid was to satisfy the physical structure of a detector array. Depending on the application, a detector array will have varying distance between detectors, however for low energy detectors or 100% coverage, a spacing of no more than 12 cm is common [1]. Although all work in this thesis is assuming a small length between detectors or detector measurements, the same method may be applied for higher density surveys. By utilizing larger increments in the MCNPX grid data, a larger detector spacing can be applied for both methods.

7.1 Limitations

The methods outlined in this thesis are intended to assist with the remediation process for fragmented sources. There are, however, currently many limitations that must be considered prior to being used in an applied scenario. As presented, both parts of

the thesis use simulated data of a source in a media for calculations. Because the simulated data are used for calculations, media parameters such as density and composition as well as background radiation must be determined prior to performing a survey. Because the same mapping is used for all processes, the method assumes that the surveying media is the same throughout, such as the case of a soil or concrete slab. The detector limitations have the assessed drawbacks of any detector system; that there are enough counts to obtain good statistics. For the methods in this thesis, the full energy peak was used rather than detection over all energies, requiring some spectroscopic discrimination at a known energy. The detection capability method described in part I of this thesis is well suited for a full range spectrum because background is considered. The localization techniques in part II, however, rely on either a high signal-to-noise ratio, or good background subtraction to determine the counts in the full energy peak. Theoretically, using a very low resolution detector, the total detector response could be used, however a larger associated error of the source activity would be expected. Both methods also have the limitation that they have only been tested for single point sources.

7.2 Future Considerations

Although the methods are intended to be used for multiple scenarios using different detectors, sources, and media, validated experiments and simulations are limited to the scenarios described in this thesis. It is predicted that much better results could be obtained using a germanium detector. Because the detector has a much better energy resolution, less error would be expected in the counting and background subtraction for the peaks. It is also desirable to validate the methods using other common scenarios,

such as the detection of Americium-241 or Depleted Uranium using low-energy detectors. Aside from the further validation of the current methods, below are suggestions for enhancements of both methods presented in this thesis.

7.2.1 3-D Source Localization

As mentioned in Chapter 6, the source localization method requires that the measurements be taken on the same plane as the buried source. An offset will yield inaccurate results in the calculated location of the source. The initial design intent for the method was an array of detectors at equal spacing moving at a very slow pace. Using a short counting interval, the localization technique could be performed at every step. The corresponding position and strength would then be the location where the detectors yielded the largest number of counts. In cases where extremely low density surveys or slow speeds are not used, an offset of the source can be expected. Expanding the localization method to account for a 3-D positioning would allow a lower survey density to be used. Preliminary calculations were performed with detectors out of a single x,z plane, but due to calculation times the analysis was outside the scope of the current work.

7.2.2 Multiple Source Localization

Currently, the localization method is only applicable for one source within the detection area. The ability to detect two sources would allow the method to be more applicable in non-laboratory scenarios where two fragmented sources may be in close proximity. Localization of two or more sources was considered outside the scope of this

work. An analysis of the limits of spatial resolution and the effects of nearby, unresolvable sources should be undertaken.

7.2.3 Certainty of Detection for Moving Detectors

Chapter 5 presents a method for determining the certainty of detection for a source using multiple static measurements. The method may be improved by allowing the certainty to be calculated using a moving detector. The modification would be a simple change due to the high density of the simulated data. By knowing the speed at which the detector is moving, as well as the counting interval of the detector, the total counts the detector will measure over the counting interval length can be represented by the sum of the grid pixels. Using the same hypothesis testing process described in Chapter 5, the certainty based on the total counts for every possible range may then be calculated.

Chapter 8

Conclusions

This thesis was a two-part problem for the detection of a gamma-emitting point source using a solid-crystal detector. The first method used known information about a source, including activity, depth of source in media, and type of media to determine the detection capability as a function of background and static measurement spacing. The second method was essentially the opposite problem, which used only the type of media and detector measurements to determine the location of a source within media, as well as the activity of the source. For both parts, simulated data were used as the expected data. MCNPX was initially chosen as the Monte Carlo transport code due to its widespread use and experimental benchmarking. Further analysis and experimental verification of the transport code was performed in the current work and demonstrated that its simulated results were very similar to that of the detector system used in this thesis. Due to the limitations of the closed-source MCNPX code, an external program was written to create an interface between the desired detector-source scenarios and MCNPX. The program greatly reduced the time required to re-write MCNPX input cards and obtain results from the simulations. The program also served as the key tool for creating the simulated data grids used by both parts of the thesis by iterating the process for many different scenarios.

Using the simulated data, the first part of this thesis presented a method for determining the certainty of detecting a source within some media using multiple static measurements. The method serves as a way to determine the minimum activity source that can be detected using a sequence of measurements. As expected, using a smaller spacing between measurements results in a higher certainty of detection. The simulated experiments demonstrate that a relatively low activity source can be seen when using only the full energy peak for analysis. Due to background and scatter, a much lower certainty would be expected when using the full-energy range of the detector.

The second part of this thesis used a minimum of three static detector measurements to determine the lateral position, depth, and activity of a source in a medium. The method was first verified using simulated detector measurements in both air and soil to verify the chi-square localization method with the only error being counting statistics. In both media, the calculated position and source activity were very similar to the expected. Once the chi-square method was verified using simulated data, the experiments were then performed using laboratory detector measurements to test the reliability of the method.

Though the experimental results are limited to only three energies and two types of attenuating media, they are evidence that the location of the source and the activity of the source can be predicted with good certainty. Furthermore, chi-square best-fit calculations take less than a second making the process very applicable for real-time surveying. Evidently, the experimental results in the soil are more accurate in localization than originally anticipated, because the technique has an advantage in attenuating media as compared with air. Through a medium, small positional changes of

the source in the depth result in large changes in detection efficiency; the concept that makes this process possible.

This work demonstrates that MCNPX simulated data can be used to obtain good results for modeling the response of an actual detector, source, and media. By utilizing the accuracy of the MCNPX code, simple yet effective methods can be applied to assist with the experimental detection and localization of sub-surface sources using solid-crystal detectors.

References

1. C. Farr, T. Alecksen, R. Heronimus, M. Simonds, D. Farrar, D. Miller, and K. Baker, "Recovery of Depleted Uranium Fragments from Soil." *Health Physics Journal*, Vol. 98. S6-S11, 2007
2. S. Lanzisera, D. Tin, and K. Pister., "RF Time of Flight Ranging for Wireless Sensor Network Localization." *International Workshop on Intelligent Solutions in Embedded Systems*, IEEE. 1-12, 2006
3. H. C. Schau and A. Z. Robinson. "Passive source localization employing intersecting spherical surfaces from time-of-arrival differences." *IEEE Trans. on Acoustics, Speech, and Signal Processing*, 35(8):1223-1225, 1987
4. D. L. Stephens and A. J. Peurrung. "Detection of moving radioactive sources using sensor networks." *IEEE Transactions on Nuclear Science*, Vol. 51:2273-2278, 2004
5. N. Shankar, J. Yau, Y. Hou, X. Sahni., "Localization Under Random Measurements with Application to Radiation Sources." *Information Fusion*, 11th International Conference. 1-8, 2008
6. B. MacDonald, B. Abidi, and M. Abidi "Deployment and Characterization of a Robotic Platform for Radiation Detection." *Department of Homeland Security Conference on Research and Development Partnerships*, 1-11, 2005
7. Howse, J., Ticknor, L., and Muske, K., "Least Squares Estimation Techniques for Position Tracking of Radioactive Sources." *Los Alamos Laboratory Report*, LA-UR-99-917, 1999
8. Reed, J., "Approaches to Multiple-source Localization and Signal Classification." *Master's thesis*, Virginia Polytechnic Institute and State University, May 2009
9. A. Hoover, M. Kippen, J. Sullivan, M. Rawool, I. Baird, and B. Sorensen, "The LANL Prototype Compton Gamma-Ray Imager." *Nuclear Science, IEEE Transactions*. Vol. 52, 2005
10. Gilbert RO. Statistical Methods for Environmental Pollution Monitoring. New York: Van Nostrand Reinhold; 1987

11. M. Davis. "The Probability of Finding a Localized Area with Elevated Contamination by Using a Mobile Detector", The Health Physics Society, Oct, 83(4):497-503, 2002
12. R. Detwiler, R. Mauer., "Modeling of Air Attenuation Effects on Gamma Detection at Altitude." U.S. Department of Energy. DOE/NV/11718-737, 2002
13. C. M. Marianno, K. A. Higley, S. C. Moss, and T. S. Palmer. "An Experimental Determination of FIDLER Scanning Efficiency at Specific Speeds." The Health Physics Society, Vol. 84. 197-202, 2002
14. J.F. Briesmeister, "MCNP - A General Monte Carlo N-Particle Transport Code, Version 5. Volume I: Overview and Theory," Los Alamos National Laboratory Report, LA-UR-03-1987, 2003
15. Hakimabad - "Response Function of a 3×3 in. NaI Scintillation Detector in the range of 0.081 to 4.438 MeV", Asian Journal of Experimental Sciences., Vol. 21, 233-237, 2007
16. A.Sood, R.P. Gardner. "A New Monte Carlo Assisted Approach to Detector Response Functions." Nuclear Instruments and Methods in Physics Research., Vol. 213. 100-104, 2004
17. D. Speaker. "Monte Carlo Application for the Use of Detector Response Function on Scintillation Detector Spectra." Master's Thesis, North Carolina State University, 2009
18. J. C. Silva. "Monte Carlo Simulation of Nuclear Logging Detection Systems." Brazilian Journal of Geophysics, Vol. 19(3), 2001
19. Glenn F. Knoll., Radiation Detection and Measurement: Third Edition. John Wiley & Sons, Inc, 2000
20. American National Standard for Programming Language - FORTRAN - Extended, American National Standards Institute, ANSI X3.198-1992, New York, NY, September 1992
21. H. Cember., Introduction to Health Physics: Third Edition. McGraw-Hill, 1996
22. Borgstrom, Mark C., et al., "Detection of Small Radiation Sources: The Effect of Mode of Count-Rate Presentation." Medical Physics, Vol. 15, No. 2. March/April 1988

23. Alex F. Bielajew, Fundamentals of the Monte Carlo Method for Neutral and Charged Particle Transport. Department of Nuclear Engineering and Radiological Sciences, The University of Michigan, 1998

24. O. Klein and Y. Nishina. Z. Physik 52. 853,1929

Appendix A: Detector Theory of Operation

The energy states of the material, determined by the crystal lattice, allow the scintillation process to occur. The valence band within the material contains electrons bound to lattice sites while the conduction band contains electrons that have sufficient energy to migrate throughout the crystal. When a particle's energy is absorbed, it may transfer enough energy for an electron to be excited from the valence band, which leaves a hole in the electrons original position. In a pure crystal, the electron will eventually de-excite back to the hole in the valence band. Intentional crystal impurities, called activators, create an intermediate band of energies, called the forbidden gap, where an electron can de-excite to the activator's ground state. If the activator is chosen appropriately, upon de-excitation, the electron will emit a lower energy photon in the ultraviolet or visible spectrum where PMTs (Photo-multiplier Tubes) are effective in detection. Alternatively, if the electron creates an excited energy configuration upon arriving at the impurity, it will not be able to return to the ground state through normal excitation. The electron then requires additional energy to raise it to a higher lying state where it may then de-excite. The resulting slow component of light is often a significant source of 'after-glow' in scintillators. This is an undesirable effect, because it produces background light during detection. Another undesirable effect in scintillation crystals is when an electron is captured at an impurity site. The transition from electron capture to the ground state, called quenching, will not emit a visible photon and represents loss mechanisms in the detection process. The scintillation efficiency, which is the amount of light generated per unit energy loss per unit energy deposited in the detector, varies depending on the material. For most inorganic scintillators, the light yield is nearly proportional to the

deposited radiation energy over a fairly wide range of energy. However some nonlinearity can be present due to the quenching processes [19]. The low energy photons are then counted by a photo-multiplier tube, which simply converts the weak light output of a scintillator into a corresponding electrical signal.

Appendix B: Photon Transport in MCNPX

Before interacting with a medium, a photon will travel some length l . The survival probability as a function of the path length is the well-known exponential attenuation law:

$$P_s(l) = e^{-\mu l},$$

where μ is a constant often referred to as the linear attenuation coefficient of the medium in units of inverse length. Because each medium is assumed to be homogenous, μ is independent of photon position. It is, however dependent on the energy of the photon interacting in the medium. The probability that a photon will travel length l and then collide in $[l, l + dl]$ becomes the differential probability of interaction:

$$P_i(l)dl = \mu(l)e^{-\mu l}dl$$

Integrating this gives the probability distribution function:

$$P_i(l) = \int_0^l \mu(l)e^{-\mu l}dl = 1 - e^{-\mu l}$$

Assigning a random number r that is randomly distributed over $[0,1]$ as the probability of interaction and solving for l yields [23]:

$$l = -\frac{1}{\mu} \ln(r)$$

For the case of photon transport, the probability of interaction is dependent on the type of transport medium and the energy of the photon. When the photon interacts within the

transport medium, it will go through one of several interaction processes which are explained in the Appendix C.

Appendix C: Photon Interactions in MCNPX

C.1: Photoelectric Effect

The photoelectric effect is the phenomenon, dominant at low energies, where a photon of energy E , after striking a tightly bound electron within an atom, is absorbed and the atom emits an orbital electron of binding energy $e < E$. The cross section formulae are typically in the form of numerical fits and take the approximate form:

$$\sigma_{ph}(E_\gamma) \propto \frac{Z^4}{E_\gamma^3}$$

Most Monte Carlo methods, MCNP included, employ a look-up table for the photoelectric interaction. Following the ejection of the electron, fluorescent photons may also be emitted. If the photoelectric event occurs within a material with an atomic mass of $Z < 12$ there will be no photons emitted above 1 keV because the possible fluorescence energy is too low. In this case, the photon track is terminated. If the incident material has an atomic mass of $12 \leq Z < 31$, then one fluorescent photon of energy greater than 1keV may be emitted. The resulting energy of the emitted photon then becomes the initial incident photon energy E , less the ejected electron kinetic energy, less the residual excitation energy. For $Z \geq 31$, two fluorescent photons are emitted.

C.2: Compton Scattering

In Compton scattering, an incident photon strikes an electron, modeled at rest and unbound, and is deflected from its original path with a loss in energy. The electron is ejected from its orbital position as result of the transferred kinetic energy. By conservation of energy, the resulting energy of the scattered photon will be:

$$E' = \frac{E}{1 + \frac{E}{mc^2}(1 - \cos \theta)}$$

Where E is the incident photon energy, m is the rest mass of the orbital electron, θ is the deflection angle of the photon, and c is the speed of light. The Monte Carlo method uses the scattering differential cross section given by the Klein-Nishina formula [24]:

$$K(\alpha, \mu)d\mu = \pi r_o^2 \left(\frac{\alpha'}{\alpha}\right)^2 \left[\frac{\alpha'}{\alpha} + \frac{\alpha}{\alpha'} + \mu^2 - 1\right] d\mu$$

Where $\mu = \cos \theta$ and r_o is the classical electron radius. α and α' are the incident and final photon energies calculated by:

$$\alpha = \frac{E}{mc^2}$$
$$\alpha' = \frac{\alpha}{1 + \alpha(1 - \mu)}$$

C.3: Coherent (Thomson) Scattering

In Thomson scattering, an electromagnetic wave is incident on a charged particle and the electric and magnetic components of the wave exert a Lorentz force on the particle. The energy is absorbed from the incident wave by the particle. It is then re-emitted as electromagnetic radiation. In Monte Carlo methods, Thomson scattering involves no energy loss, and thus cannot produce electrons for further transport. Only the scattering angle θ of the photon is computed and the transport continues. The energy-independent cross section of Thomson scattering is represented by the formula:

$$T(\mu) = \pi r_o^2 (1 + \mu^2) d\mu$$

with μ as defined in section C.2.

C.4: Pair Production

Pair production is a direct conversion of radiant energy to matter when an electron and a positron are formed or materialized when a photon of sufficient energy passes near a nucleus. For pair production to occur, the incident photon must have an energy of at least $E_\gamma = 2m_e c^2$ (1.022 MeV), the mass of two electrons. Any energy in excess will be converted into motion of the electron-positron pair. In MCNP, both an electron and positron are produced but not transported. The positron is annihilated locally and a photon pair is created for transport. The thick-target bremsstrahlung approximation will be applied to the electron where it will be slowed to rest locally and may produce bremsstrahlung photons during the process [14].

Appendix D: MCNPX Photon Transport Logic

Through the processes of photon interactions, there are many statistical events that allow the event of one photon to turn into multiple photons of varying energies. The process by which MCNP tracks these events can be described by a simplified model of one finite volume of one homogenous transport medium. When a photon is born in a simulation, its parameters are placed in a stack array. The stack array has the key purpose of holding a photon and its histories through the transport process. It is assumed that most simulations will have a threshold where the photon is no longer relevant to the simulation. Should a photon fall below this threshold energy, it will immediately be removed from the simulation. Defining an energy threshold applicable to the simulation can significantly reduce the calculation time because low energy photons, typically undergoing the photoelectric effect, are ignored. When a photon begins the transport routine from the top of the stack, it is first tested to see if it falls below the defined energy threshold. If it is found to be below the threshold, it is terminated, and the next photon in the stack is started. If the stack is empty, a new photon history is started and placed in the stack. If the photon energy is above the threshold, it is traversed through the medium by sampling from the path length distribution. If at any time during the simulation, the photon escapes the volume of interest, it is terminated. In the case that the simulation has more than one transport medium, the photon would be passed on to a new stack. If the photon does not leave the volume at the end of its path, it will be sampled to determine the type of interaction that is most probable. Any resulting photons that are created from the interaction process will be placed in the stack. Lower energy photons will be positioned at the top of the stack with the expectation that they will be killed more quickly and keep

the stack as small as possible to conserve memory. The process is repeated until the stack is empty and all histories are completed [23].

Appendix E: MCNPX Input Files

Input File E.1: Verification File for Cs-137

```

1  204 -0.001225 -2 4
2  208 -2.7 2 -1
3  204 -0.001225 -3 1 5 6
4  0 3
5  1 -3.67 -4
6  268 -8 -5
7  228 -2.35 -6

1  rcc 0 0 0 0 0 22.225 4.04749
2  rcc 0 0 0.0508 0 0 22.1234 3.9971
3  so 999
4  rcc 0 0 0.3 0 0 7.62 3.81
5  rpp -40 40 -11.548745 -10.9137 -40 35.55
6  rpp -40 40 -11.548745 100 35.56 43.18

mode p
c -----Al-----
m208 13000.02p -1 $MAT208
c -----Air-----
m204 7000.02p -0.755636 $MAT204
      8000.02p -0.231475 18000.02p -0.012889
c -----Concrete-----
m228 1000.02p -0.005558 $concrete (ordinary with ENDF-VI)
      8000.02p -0.4980765 11000.02p -0.017101 12000.02p -
0.002565
      13000.02p -0.045746 14000.02p -0.3150923 16000.02p -
0.001283
      19000.02p -0.019239 20000.02p -0.0829411 26000.02p -
0.012398
c -----NaI-----
m1 11000.02p -0.153373 $MAT1
     53000.02p -0.846627
c -----Stainless Steel-----
m268 6000.02p -0.0003 $SS-316,SS-316L (with ENDF-VI)
      14000.02p -0.005 15000.02p -0.000225 16000.02p -
0.00015
      24000.02p -0.1699999 25000.02p -0.01 26000.02p -
0.6693245
      28000.02p -0.1200007 42000.02p -0.0249999c
c -----
imp:p 163 158 1 0 175 1 1 $ 1, 5
c -----Source-----
sdef erg=0.6617 pos=0 0 -15.24
f8:p 5
cut:p 2j 0 0
c -----Gaussian Energy Broadening
FT8 GEB -0.00789 0.06769 0.21159
c -----Energy Bins-----
e8 0 1e-5 1e-3 1023i 3

```

nps 100000000

Input File E.2: Verification File for Na-22

```

1  204 -0.001225 -2 4
2  208 -2.7 2 -1
3  204 -0.001225 -3 1 5 6
4  0 3
5  1 -3.67 -4
6  268 -8 -5
7  228 -2.35 -6

1  rcc 0 0 0 0 0 22.225 4.04749
2  rcc 0 0 0.0508 0 0 22.1234 3.9971
3  so 999
4  rcc 0 0 0.3 0 0 7.62 3.81
5  rpp -40 40 -11.548745 -10.9137 -40 35.55
6  rpp -40 40 -11.548745 100 35.56 43.18

mode p
c -----Al-----
m208 13000.02p -1 $MAT208
c -----Air-----
m204 7000.02p -0.755636 $MAT204
      8000.02p -0.231475 18000.02p -0.012889
c -----Concrete-----
m228 1000.02p -0.005558 $concrete (ordinary with ENDF-VI)
      8000.02p -0.4980765 11000.02p -0.017101 12000.02p -
0.002565
      13000.02p -0.045746 14000.02p -0.3150923 16000.02p -
0.001283
      19000.02p -0.019239 20000.02p -0.0829411 26000.02p -
0.012398
c -----NaI-----
m1 11000.02p -0.153373 $MAT1
     53000.02p -0.846627
c -----Stainless Steel-----
m268 6000.02p -0.0003 $SS-316,SS-316L (with ENDF-VI)
      14000.02p -0.005 15000.02p -0.000225 16000.02p -
0.00015
      24000.02p -0.1699999 25000.02p -0.01 26000.02p -
0.6693245
      28000.02p -0.1200007 42000.02p -0.0249999c
c -----
imp:p 163 158 1 0 175 1 1 $ 1, 5
c -----Source-----
sdef erg=d1 pos=0 0 -30
SI1 L 0.511 1.2745
SP1 1.8 0.998
f8:p 5
cut:p 2j 0 0
c -----Gaussian Energy Broadening
FT8 GEB -0.00789 0.06769 0.21159
c -----Energy Bins-----
e8 0 1e-5 1e-3 1023i 3
nps 100000000

```

Input File E.3: Verification File for Co-60

```

1  204 -0.001225 -2 4
2  208 -2.7 2 -1
3  204 -0.001225 -3 1 5 6
4  0 3
5  1 -3.67 -4
6  268 -8 -5
7  228 -2.35 -6

1  rcc 0 0 0 0 0 22.225 4.04749
2  rcc 0 0 0.0508 0 0 22.1234 3.9971
3  so 999
4  rcc 0 0 0.3 0 0 7.62 3.81
5  rpp -40 40 -11.548745 -10.9137 -40 35.55
6  rpp -40 40 -11.548745 100 35.56 43.18

mode p
c -----Al-----
m208 13000.02p -1 $MAT208
c -----Air-----
m204 7000.02p -0.755636 $MAT204
      8000.02p -0.231475 18000.02p -0.012889
c -----Concrete-----
m228 1000.02p -0.005558 $concrete (ordinary with ENDF-VI)
      8000.02p -0.4980765 11000.02p -0.017101 12000.02p -
0.002565
      13000.02p -0.045746 14000.02p -0.3150923 16000.02p -
0.001283
      19000.02p -0.019239 20000.02p -0.0829411 26000.02p -
0.012398
c -----NaI-----
m1 11000.02p -0.153373 $MAT1
     53000.02p -0.846627
c -----Stainless Steel-----
m268 6000.02p -0.0003 $SS-316,SS-316L (with ENDF-VI)
      14000.02p -0.005 15000.02p -0.000225 16000.02p -
0.00015
      24000.02p -0.1699999 25000.02p -0.01 26000.02p -
0.6693245
      28000.02p -0.1200007 42000.02p -0.0249999c
-----
imp:p 163 158 1 0 175 1 1 $ 1, 5
c -----Source-----
sdef erg=d1 pos=0 0 -15.24
SI1 L 1.173237 1.332501
SP1 0.99974 0.999856
f8:p 5
cut:p 2j 0 0
c -----Gaussian Energy Broadening
FT8 GEB -0.00789 0.06769 0.21159
c -----Energy Bins-----
e8 0 1e-5 1e-3 1023i 3

```

nps 100000000

Input File E.4: Cs-137 in soil

```

1  204 -0.001225 -2 4
2  208 -2.7 2 -1
3  204 -0.001225 -3 1 5
4  0 3
5  1 -3.67 -4
6  260 -1.5 -5 -3

1  rcc 0 0 0 0 0 22.225 4.04749
2  rcc 0 0 0.0508 0 0 22.1234 3.9971
3  so 999
4  rcc 0 0 0.3 0 0 7.62 3.81
5  pz -15.24

mode p
c -----Al-----
m208 13000.02p -1 $MAT208
c -----Air-----
m204 7000.02p -0.755636 $MAT204
      8000.02p -0.231475 18000.02p -0.012889
c -----NaI-----
m1 11000.02p -0.153373 $MAT1
     53000.02p -0.846627
c -----Dirt-----
m260 8000.02p -0.5134 $soil (dry U.S. Ave. with ENDF-VI)
      11000.02p -0.006 12000.02p -0.013 13000.02p
-0.067
      14000.02p -0.2764 19000.02p -0.014 20000.02p
-0.05
      22000.02p -0.0045 25000.02p -0.0007 26000.02p
-0.055
c -----
imp:p 163 158 5 0 175 1 $ 1, 5
c -----Source-----
sdef erg=0.6619 pos=0 0 -15.24
f8:p 5
cut:p j j 0 0
elpt:p 5j 0.6615 $Kill the photons in the dirt that falls below .6615
e8 0 1e-5 0.6615 0.6619
nps 10000000

```

Input File E.5: Na-22 (0.511 MeV) in soil

```

1  204 -0.001225 -2 4
2  208 -2.7 2 -1
3  204 -0.001225 -3 1 5
4   0      3
5   1  -3.67 -4
6  260  -1.5 -5 -3

1      rcc 0 0 0 0 0 22.225 4.04749
2      rcc 0 0 0.0508 0 0 22.1234 3.9971
3      so 999
4      rcc 0 0 0.3 0 0 7.62 3.81
5      pz -15.24

mode p
c -----Al-----
m208 13000.02p          -1 $MAT208
c -----Air-----
m204 7000.02p          -0.755636 $MAT204
      8000.02p          -0.231475 18000.02p          -0.012889
c -----NaI-----
m1   11000.02p          -0.153373 $MAT1
      53000.02p          -0.846627
c -----Dirt-----
m260 8000.02p          -0.5134 $soil (dry U.S. Ave. with ENDF-VI)
      11000.02p          -0.006 12000.02p          -0.013 13000.02p
-0.067
      14000.02p          -0.2764 19000.02p          -0.014 20000.02p
-0.05
      22000.02p          -0.0045 25000.02p          -0.0007 26000.02p
-0.055
c -----
imp:p   163   158   5   0   175   1   $ 1, 5
c -----Source-----
sdef erg=0.511 pos=0 0 -15.24
f8:p 5
cut:p j j 0 0
elpt:p 5j 0.509 $Kill the photons in the dirt that falls below .509
e8 0 1e-5 0.509 0.513
nps 10000000

```

Appendix F: Matlab Programs

Program F.1: Grid Detection Probability Function

```
function [cm] = gridprob(xdata, ydata, cdata, freq, bg)

xlim = max(xdata(:)) - min(xdata(:));
ylim = max(ydata(:)) - min(ydata(:));

prob = zeros(ylim + 1, xlim + 1);
probnnot = 1;
totprob = 0;

for yindex = 0:freq - 1
for xindex = 0:freq - 1

    for y=(1 + yindex):freq:(ylim + 1)

        if y > ylim + 1
            exit for;
        end

        for x=(1 + xindex):freq:(xlim + 1)

            if x > xlim + 1
                exit for;
            end

            %calc the probability at each location with 99%
confidence
                prob(y,x) = normcdf(((cdata(y,x)) -
                (2.326*sqrt(bg)))/sqrt(cdata(y,x)+bg));
            if prob(y,x) < 5e-2
                prob(y,x) = 0;
            end
            probnnot = probnnot * (1 - prob(y,x));

        end

    end

    %Account for starting location
    totprob = totprob + ((1 - probnnot)*(1/freq^2));
    probnnot = 1;
end
end

cm = totprob;

end
```

Program F.2: Chi-Square Function

```
function [chi,S,xpos,depth] = chisq(xdata, ydata, cdata, spacing,
Edata)

xlim = max(xdata(:)) - min(xdata(:));
ylim = max(ydata(:)) - min(ydata(:));

chi = zeros(ylim + 1,xlim + 1); % Holds the chi-square values
Fa = chi;
vals = Edata;
EdataF = Edata/mean(Edata(:)); % Holds the experimental data

for y=1:(ylim + 1)
for x=1:(xlim + 1)

    for i=1:length(Edata)

        % make sure it is within the grid
        if(x + round((i-1)*spacing) < xlim + 1)
            vals(i) = cdata(y,x + round((i-1)*spacing));
        end

    end

    EdataT = (EdataF)*mean(vals(:)); % normalize to the avg value
    Fa(y,x) = mean(Edata./EdataT);

    for k=1:length(Edata)
        chi(y,x) = chi(y,x) + (((EdataT(k) - vals(k))^2)/ vals(k));
    end
end
end

[Y X] = find(chi==(min(chi(:)))); % The lowest value is the position
S = Fa(Y,X); % Get the source at that location
xpos = xdata(X); % Get the x position
depth = ydata(Y); % Get the depth

end
```

Program F.3: Confidence Interval Function

```
function [R] = confidence(xdata, ydata, cdata, R, offset, S)

xlim = max(xdata(:)) - min(xdata(:));
ylim = max(ydata(:)) - min(ydata(:));

Rt = zeros(ylim + 1, xlim + 1);
It = zeros(ylim + 1, xlim + 1);

It(:, :) = 1;

for i = 1:length(R)

    Rt(:, :) = cdata*S(i);

    val = R(i);
    std = sqrt(val);

    for y=1:(ylim + 1)
    for x=1:(xlim + 1)

        if Rt(y,x) >= (val-3*std) && Rt(y,x) < (val + 3*std)
            if Rt(y,x) >= (val-2*std) && Rt(y,x) < (val + 2*std)
                if Rt(y,x) >= (val-std) && Rt(y,x) < (val + std)
                    Rt(y,x) = 0.682;

                    else
                        Rt(y,x) = 0.272;
                    end
                else
                    Rt(y,x) = 0.042;
                end
            else
                Rt(y,x) = 0;
            end
        end

    end

end

Rt = Rt.*(1/sum(Rt(:)));

temp = shiftl(Rt,0, offset*(i-1));

It = It.*temp;
end

It = It.*(1/sum(It(:)));

t = unique(It);
m = length(t);
```

```
for j=1:m
    l = length(find(It == t(j)));
    It(It == t(j)) = l.*t(j);
end
R = It;
```